COMPUTATIONAL MORPHOLOGY MODELLING AND MIXED MODE FRACTURE ANALYSIS OF ZrB_2/SiC BASED CERAMIC NANO-MATERIALS USING MOLECULAR DYNAMICS

by

KRUTARTH SHAILESHKUMAR PATEL

Presented to the Faculty of the Graduate School of

The University of Texas at Arlington in Partial Fulfillment

of the Requirements

for the Degree of

MASTER OF SCIENCE IN AEROSPACE, AERONAUTICAL AND ASTRONAUTICAL/SPACE ENGINEERING

THE UNIVERSITY OF TEXAS AT ARLINGTON

December 2017

Acknowledgements

I would like to start by acknowledging my advisor, Dr. Ashfaq Adnan whose constant guidance, patience and support motivated me for this work. I have always benefitted by his passion for research and deep understanding of this field. I sincerely thank him for introducing me to this field of research. I would also like to acknowledge Dr. Kenneth Reifsnider and Dr. Andrey Beyle for serving on my thesis defense committee and for their valuable help during my defense.

I would also like to acknowledge Dr. Yuan-Ting Wu, for sharing his immense experience in the field of molecular dynamics.

I heartily thank all the member of Multiscale Mechanics and Physics Lab at UTA for all the wonderful times spent in the lab. Especially, this work would not have been completed without my colleagues Riaz Kayser and Rajni Chahal, who constantly offered their help during the project.

January 4, 2018

Abstract

COMPUTATIONAL MORPHOLOGY MODELLING AND MIXED MODE FRACTURE ANALYSIS OF ZrB_2/SiC BASED CERAMIC NANO-MATERIALS USING MOLECULAR DYNAMICS

Krutarth Patel, MS

The University of Texas at Arlington, 2017

Supervising Professor: Ashfaq Adnan

Transition metal carbides, nitrides, and borides are a group of Ultra High-Temperature Ceramic (UHTC). Owing to their remarkable properties of the high melting point, high thermal conductivities and excellent strength at elevated temperature ZrB_2 based composites are of high interest for use in the high-temperature environment. It is proved that addition of SiC in ZrB_2 can advance composite's oxidation resistance, mechanical strength, fracture toughness and sintering behavior. Firstly, molecular dynamics is used to simulate crack growth under mixed mode loading in Al, SiC, and ZrB_2 single crystals by considering inclined crack under uniaxial tension and crack growth angle are compared with those obtained by Maximum Stress criterion analytically. Subsequently, the role of grain boundary in the fracture is studied, and core-shell type morphology of ZrB_2-SiC based ceramics is modeled using Molecular dynamics tool to demonstrate the effect of modified grain boundaries on mechanical properties of such materials. Results from molecular dynamics simulations indicated that fracture under mixed mode conditions is mainly stress based and provided the good interatomic potential field molecular dynamics is capable enough to generate results in good agreement with experiments and theory. Also, a morphological study of the core-shell ZrB_2/SiC system revealed that increasing

amount of SiC above the certain limit could have a detrimental effect on material's strength, but it might increase fracture toughness of the system.

Dedicated to my family and friends for their never-ending love and support

Table of Contents

List of Illustrations

List of Tables

Chapter 1

Introduction

Mankind has always sought ways to imitate the nature. Flight has been one of these fascinating things over the centuries. Among the many tries over centuries, Wright brothers were able to make first sustained, heavier than air, power controlled flight in 1903. As they say *'Necessity is the mother of invention'*; the necessity of air power during WWI and WWII brought about great changes in understanding of aerodynamics which led to faster development of aerospace industries. By the end of WWII, turbojet engines were widely used in military aircrafts. Owing to their shorter travel time aircrafts were considered as next faster transportation technique in the era where most of the long-distance travels were carried out by ships. Then came an era of Cold War and lots of projects were carried out by different governments to achieve the most advanced technological state in aerospace industries. Flight of Bell X-1 research plane powered by a rocket engine by Chuck Yeager crossed the sound barrier and brought mankind into the age of faster than sound flights. During his flights he reached as high as Mach 2.44, that is 2.44 time faster than the speed of sound. But with the Cold War, started the “Space Race” and technological experiments were commenced to make the flight vehicles go beyond 5 times the speed of sound, and thus started the age for hypersonic flights.

With this determination of research and development to make aircrafts more efficient, faster and to make them reach farther than ever, we are constantly searching for the technology of the future, especially in hypersonic and re-entry aerial vehicles. As demonstrated records, Bell X-1 had already achieved supersonic flight and around mid-twentieth century aerodynamics of compressible flow were extensively studied which resulted in a plethora of military aircraft and a few of civil aircraft such as Concorde and Tupolev Tu-144 working at supersonic speeds.

Research aircraft X-15, developed by North American Aviation Inc. became first hypersonic rocket-powered aircraft to set records on highest speed in manned and powered aircraft. In 1967 William J. Knight flew at Mach 6.72 using X-15 aircraft which remains an unbroken record [1]. During the flight of X-15 surface temperature reached around 1350^{o} F and shock-shock interference heating took local temperature as high as 2795 ^{o} F. Certainly conventional materials which were being used below hypersonic flight regime were not capable enough to carry on such adverse conditioned flight. As the research goes on to reach new heights of speed (e.g., research project as X-43), there is a critical need to develop materials which are tough enough in such extreme environmental conditions. In the hypersonic flight regime, the temperature can exceed 2600 ^{o} C, and at such high temperature, most materials melt or greatly lose their mechanical properties, which might lead to catastrophic failure of the operating components leading to complete aircraft failure.

In hypersonic vehicles, aerodynamic drag parameter plays an important role. To reduce aerodynamic drag and thus to enhance lift-to-drag ratio and maneuverability, hypersonic vehicles require sharp leading edged profiles with the curvature of the edges not exceeding a few millimeters, which gives rise to adverse heat fluxes at stagnation point which in turn renders conventional aerospace materials such as carbon fiber reinforced SiC matrix composites useless [8,11]. But we have not been able to achieve a sustained hypersonic flight not only due to high temperatures but also because of extreme aerodynamic loads which include separated strong shock waves. With the combination of the high temperature and high aerodynamic loading, very few materials would be able to withstand these conditions. The hypersonic flight being an aggressive oxidizing environment further increases the difficulty of finding proper materials to withstand both thermally and mechanically extreme environment. Oxygen and Nitrogen disassociation,

which is splitting of a diatomic molecule to single atoms that then can readily react is the reason for such a highly oxidizing environment [12-17].

Similarly, nose-cones of re-entry vehicles undergo same adverse environment and are also hypersonic. At the time of re-entry from lower earth orbit, the speed reaches as high as 17,500 mph which is close to Mach 25. During this time there exists not only high temperature but also very high-temperature gradient. During re-entry, main components that this extreme environment affects are the leading edges and nose cones. These temperature gradients can be as high as 1000 °C in a very short distance [11]. Even with the high aerodynamic loading along with the high thermal loading, the material of these components should be able to hold their shape. Hence, the material should be oxidation resistant and withstand to ablation (the phenomenon of material removal by vaporization).

Once again from the mentioned conditions of the environment, one can determine the properties of materials that must be met. The materials should have a high melting temperature, oxidation resistance, high thermal conductivity, high toughness, and high Young's modulus. This brings us to a group of materials that are called Ultra High-Temperature Ceramic (UHTC) composites; these ceramic composites have high thermal conductivity and high melting temperatures, making them perfect candidates for hypersonic vehicles. Figure 3 below shows all the components and effects of atmospheric re-entry from space.

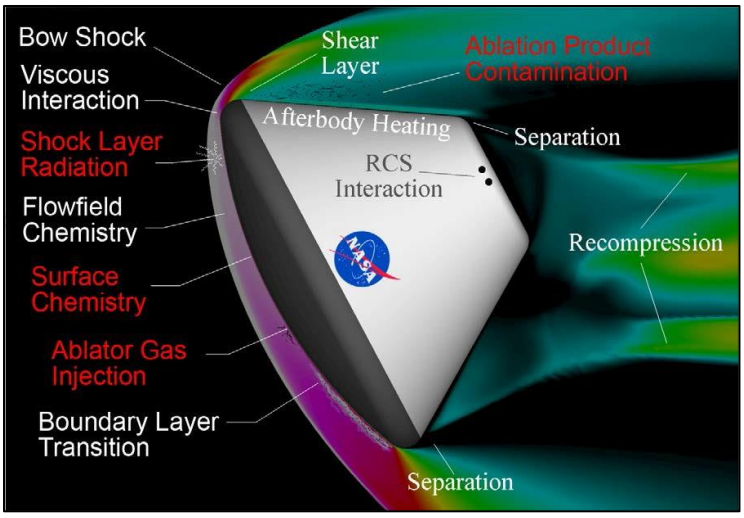

Figure 1-1: Complex environment during re-entry to Earth's atmosphere [132]

With the aforementioned environment condition, one can come up with the requirements that the material must meet in order to be used for this application. Therefore, the material must have a high strength to withstand the high aerodynamic forces, have a high thermal conductivity to be able to handle the high heat fluxes and stagnation point temperature, and since the application is an aerial vehicle, the material must have a lower density. Ceramics based on group IV-V Transition Metal Borides and carbides possess melting points above 3000 °C, are ablation resistant and therefore are capable enough to be used in next-generation space vehicles, leading edges and nose-cones of hypersonic vehicles and rocket nozzle inserts [4]. ZrB_2 and HfB_2 have a unique combination of mechanical and physical properties. They are known for their high melting points (>3000 °C), high thermal and electrical conductivities, chemical inertness against molten metals and great thermal shock resistance. Their carbides, in spite having highest melting points these borides are much suitable at thermo-mechanical environment imposed at the time of hypersonic flight. But from these two material systems, ZrB_2 particularly is of more interest, owing to its lowest theoretical density [19]. But poor oxidation resistance of the monolithic

ZrB_2 is well known, and to mitigate this problem addition of SiC is well known. The addition of SiC increases not only its oxidation resistance but also its sintering capabilities. Generally, ZrB_2 with 15-20 %vol SiC is selected as a potential material system. During its oxidation, SiC forms glassy SiO layer, which prevents oxygen from penetrating further into the material. Thus, one can say SiO acts as an effective barrier between the environment and the vehicle body. Figure 1-2 below shows the result of oxidation at 1900 °C at three different compositions of SiC in ZrB_2.

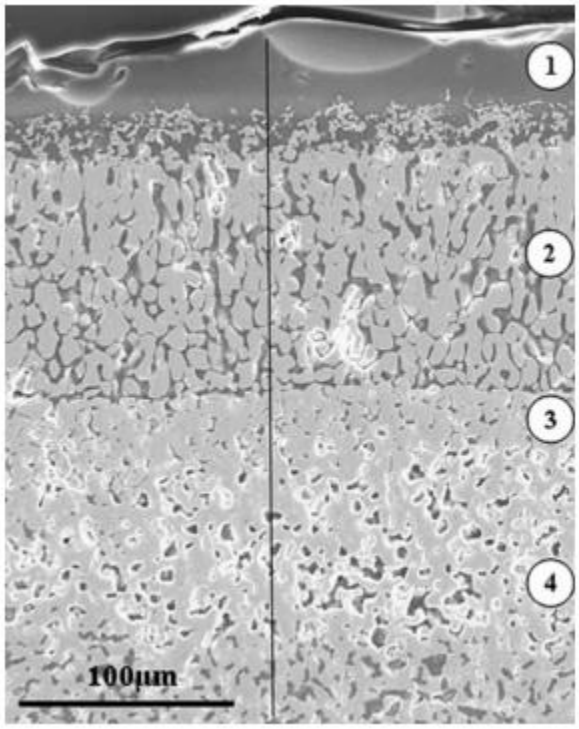

Figure 1-2: SEM image of ZrB_2 + 20 vol% SiC oxidized at 1900 K temperature (1) outer glass layer (2) ZrO_2 based interlayer (3) SiC depleted zone, and (4) unreacted ceramic [9]

Along with the addition of SiC to make ZrB_2 more suitable candidate in highly oxidizing environment secondary phases can be added additionally to increase the fracture toughness of the material. Crack-tip shielding mechanism such as dislocation cloud, micro-crack agglomeration, phase change, secondary ductile phase, fiber/whiskers bridging can be employed to make these materials tougher along their grain boundaries. But before moving to additives, it is necessary to develop an understanding of the mechanical response of each constituent. Hence, a major part of the present study revolves around the prediction of fracture in constituents of ZrB_2-SiC ceramics.

Following this introduction thesis is divided into five sections. The upcoming section is the literature review, which includes advances made in ZrB_2-SiC ceramic composites and their properties as found in literature. This includes crystal structure, processing methods, a fracture in materials and possible toughening techniques. Following literature review is the set-up and methodology section, which will go over the details of molecular dynamics simulation set-up used to assess crack propagation under mixed mode loading and toughening mechanism. Following it, is the results and discussion, conclusion, and future scope of this research.

Chapter 2

Literature Review

An extensive literature review is carried out to know advances made in ZrB_2 based ceramics as it is necessary to get acquainted with what others have done so far, which also provides the way to direct the research in a proper manner. This also provides meaning to understand the validity of obtained results. That is why this section is included in this thesis. Research stating the need of such material are mentioned to start with, and as the thesis progresses, the fracture in materials is discussed with prime interest in predicting crack growth under mixed mode loading, and finally, possible modification in grain morphology is suggested.

Soboyejo et al. [7] reviewed the high-temperature ceramics for aerospace application history, effort to toughen ceramics for high-temperature structural application in zirconia-based ceramics, aluminum oxide, silicon carbide, silicon nitride, molybdenum disilicide and zirconium diborides. Ceramic Matric Composites are being used in Thermal Barrier Coating which can be helpful in improvement of the thrust and efficiencies of aero-engines and land-based gas turbines. Yttria-doped zirconia (Y_2O_3-ZrO_2) is deposited by Plasma Spray or Electron Beam Physical Vapor Deposition Techniques which is still susceptible to thermally grown oxide (TGO) layer as a reaction product due to inter-diffusion due to high temperature environment ranging from ~500-600 °C in turbine disks and to ~1100-1150 °C in turbine blades, which can be mitigated by doping the stated TBC with heavy elements such as Hf or Zr. Similarly, Thermal Protection Systems (TPS), should have the capacity to withstand high mechanical load at a temperature as high as 1800 °C in the air. In some cases, like Reusable Launch Vehicles (RLVs) the TPS should be capable enough to maintain the inner temperature below ~200 °C while maintaining the outer temperature between 600 and 1650 °C and in cases of re-entry vehicles' materials,

they are expected to be strong. Hence, SiC-SiC composites, oxide-oxide composites, Si_3N_4-Si_3N_4 composites, carbon-carbon composites and zirconium diborides composites are researched as multifunctional structural materials for TPS in advanced hypersonic vehicles.

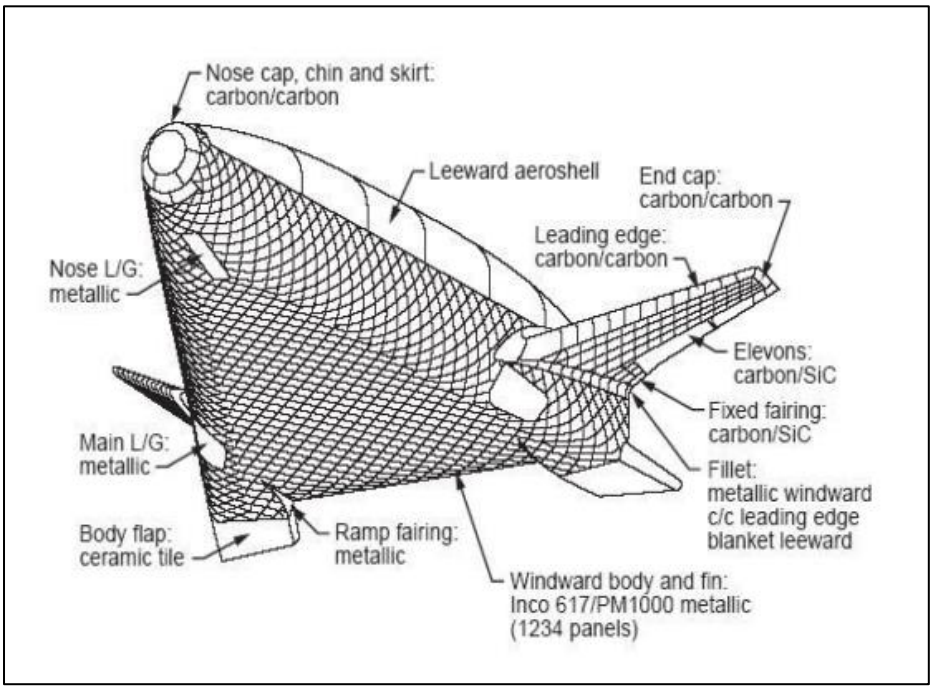

Figure 2-1: Different composites in X-33 Thermal Protection System [7]

Being interested in predicting crack growth in ZrB_2-SiC composite material, the first thing that one would care for learning about a material is the crystal structure or the smallest repeatable unit cell and the phase diagram of the constituent materials of the composite. Learning about crystal structure is important because it determines the density of material along with the mechanical properties. The phase diagram is critical, especially when one is studying materials for high-temperature application as it indicates which phase is possible at a particular temperature and pressure.

2.1 : ZrB_2 Crystal Structure

Li et al. [20] performed first-principles molecular dynamics simulations to predict the crystal structure for ZrB and ZrB_2 knowing their chemical composition and atom ratios. They found that ZrB took FCC structure with space group Fm-3 m No. 225 with a lattice constant a = 4.900 Á whereas ZrB_2 took a hexagonal structure with space group P6/mmm No. 191 with a = 3.170 Á and c = 3.544 Á which were consistent with the available experimental data. The ZrB_2 crystal structure is shown in following images. As shown, the only hexagonal structure is displayed by ZrB_2 for stated phase. Location of Zr and B atoms are easily noticeable from the ZrB crystal structure in Fig. 2-2(a) and ZrB_2 crystal structure in Fig. 2-2(b). A better representation of ZrB_2 crystal structure can be seen in the Fig. 2-3.

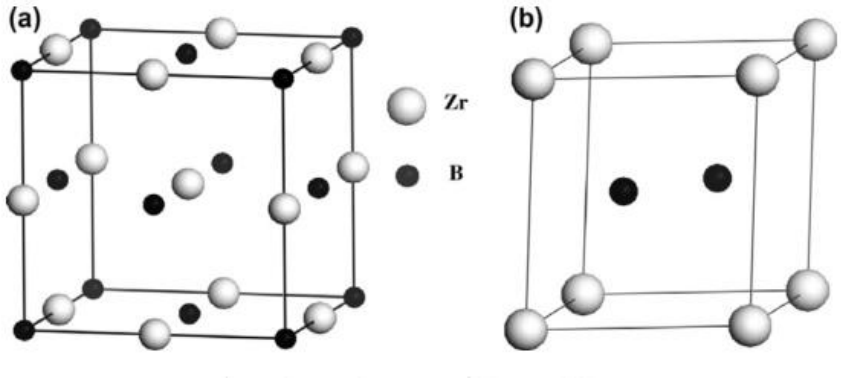

Figure 2-2: A basis unit for (a) ZrB and (b) ZrB_2 [20].

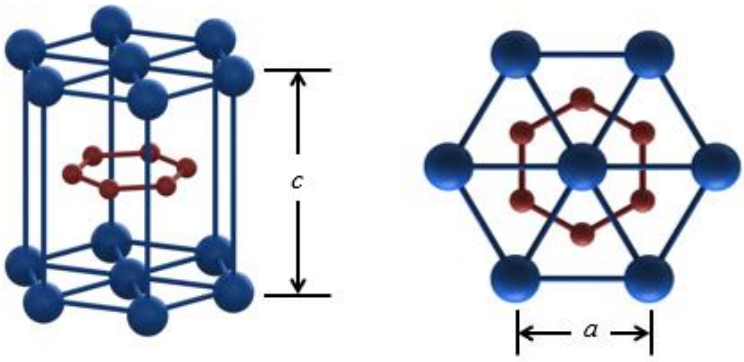

Figure 2-3: 3D Visualization of ZrB_2 crystal structure [146]

2.2 : ZrB_2 - Phase Diagram, Oxidation Behavior, and Mechanical Properties

Phase diagram for Zr-B system is shown in Figure 2-4. Phase diagrams of the materials include information about all the possible phases a material system can be of provided chemical composition and temperature. More than one phase diagram may exist for a particular material. Here only one phase diagram is shown as it is the only one accessible by Zr-B material system.

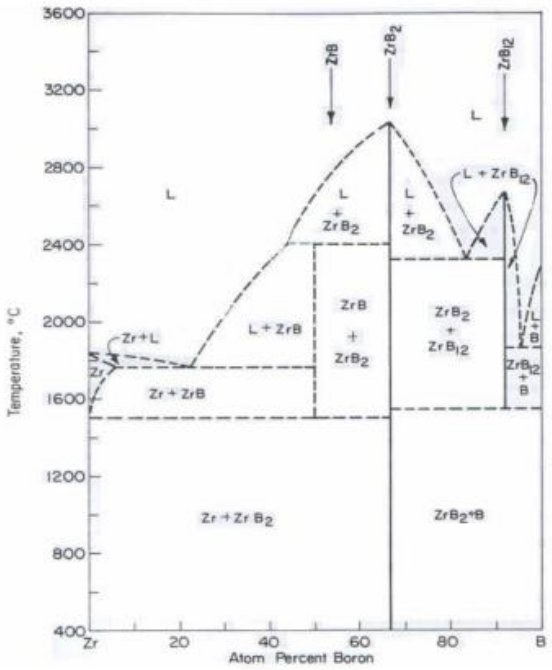

Figure 2-4: Zr-B Phase Diagram [133]

Very high melting temperature, slow solid-state reaction rates, and boron vaporization have been concluded as key factors which complicated the determination of accurate phase equilibration diagram for ZrB_2. Also, limited experimental data is available due to the inability of carrying conventional thermal analysis due to very high liquidus temperature of ZrB_2 [22]. In addition, Boron may have more than one phase present at high temperature due to its vaporization which does not represent material as a whole.

Loehman et al. [21] reported that ZrB_2 prepared by powder metallurgy techniques might have more than one boride phases. Mono-boride and di-boride are two important compounds formed in this system, where ZrB_2 is a dominant phase with a melting point of 3247 °C. Despite this, the ZrB_2 phase has a very limited range of homogeneity as it might end up having ZrB and ZrB_{12} phase in the range of 1500 °C to 2200 °C if not produced carefully.

ZrB_2 resists oxidation for temperatures as high as 1000 – 1300 °C after which oxygen diffuses through the formerly generated porous ZrO_2 phase and reacts with the sub-stoichiometric ZrO_2 to form ZrO_2 for longer heating times. Solid phase transformation of ZrO_2 from monolithic to a tetragonal structure occurs at 1150 °C and from tetragonal to cubic structure at 2370 °C which causes large volume change, which can further result in the destruction of any large-scale component containing them. Hence, ZrB_2 must have some inclusions which have the capability to stabilize this phase transformation to avoid such destructions [21]. Kuriakose and Margrave studied oxidation rate of ZrB_2 at a temperature of 1218 – 1529 °C [23].

Different researchers have reported varying values of mechanical properties for both monolithic as well as a bulk form of ZrB_2 over the time. Overall properties of ZrB_2 are listed in Table 2-2-1, after which, Table 2-2-2 and 2-2-3 represent data from different researchers for monolithic as well as bulk ZrB_2 to get acquainted with the variations into the properties over the time of research.

Table 2-2-1: Overall properties of ZrB_2

Density [31]	6.09 g/cm3
Young's Modulus [24,25]	489.0 – 493.0 GPa
Fracture Toughness [32,33]	5.46 – 6.02 MPa.$\sqrt{\mathrm{m}}$

Table 2.2.1 – *Continued*

Flexural Strength [32,33]	416.0 – 708.0 MPa
Vickers Hardness [24]	21.0 – 23.0 GPa
Melting Temperature [H. C. Starck, "ZrB_2 Grade B.", Germany]	3100 – 3500 °C
Co-efficient of Thermal Expansion [34,26]	5.9×10^{-6} K^{-1}
Thermal Conductivity [24]	60.0 W/mK

The elastic constants of a material describe its response to an applied stress. Stress and Strain have three tensile and three shear components, giving six components in total. The linear elastic constant form 6 x 6 symmetric matrix, having 27 different components and 21 of which are independent. However, any symmetry presented in the structure may reduce the number of these components. Hexagonal ZrB_2 crystal has six different elastic coefficient, namely C11, C12, C13, C33, C44, and C66, but only five of them are independent as C66 = (C11-C12)/2. Mechanical properties of ZrB_2 Single crystal have been reported by many researchers [20,21,24,25].

Table 2-2-2: Experimental as well as calculated Elastic Constants for monolithic ZrB_2

Method	C11	C12	C13	C33	C44
GGA-PBE [20]	504.4	90.5	112.0	427.4	240.9
GGA-PW91 [20]	502.6	94.6	129.8	477.9	269.2
LDA-CA-PZ [20]	547.2	108.6	129.8	477.9	269.2
Exp. [25, 26, 27]	581.0	55.0	121.0	445.0	240.0
Calc. [28, 29]	578.0-586.0	65.0-71.0	121.0-138.0	436.0-472.0	252.0-271.0
Calc. [30]	540.0	56.0	114.0	431.0	250.0

GGA and LDA are Density Functional Theory techniques
GGA: Generalized Gradient Approximation
LDA: Local Density Approximation

Apart from this, reported experimental properties for bulk ZrB_2 by different researchers are presented in Table 2-2-3, below.

Table 2-2-3: Experimental Mechanical Properties of ZrB_2 reported by several researchers [51]

References	Relative Density (%)	Grain Size (μm)	Elastic Modulus (GPa)	Hardness (GPa)	Fracture Toughness (MPa.$\sqrt{m}$)	Flexural Strength (MPa)
[18,35-37]	87	10	346±4	8.7±0.4	2.4±0.2	351±31
[38]	90	-	-	16.1±1.1	1.9±0.4	325±35
[19,39,40]	90.4	6.1	417	-	4.8±0.4	457±58
[41]	95.8	10	-	16.5±0.9	3.6±0.3	450±40
[42]	97	8.1	479±8	16.7±0.6	2.8±0.1	452±27
[43]	97.2	5.4±2.8	498	-	-	491±22
[44,45]	98	9.1	454	14.5±2.6	-	444±30
[46]	>98	-	-	14.7±0.8	-	300±40
[47]	~99	20	491±34	-	-	326±46
[48,49,50]	99.8	~6	489	23±0.9	3.5±0.3	565±53

2.3 : SiC Crystal Structure

Polytopes are repeated number of different structural modifications that a material can be without any change in fundamental composition. SiC has many polytypes, nearly 250 crystalline forms to be precise. The most common of these are 3-Cubic, 2-Hexagonal, 4-Hexagonal, 6-Hexagonal, 8-Hexagonal and 15-Rhombohedral [55]. Alpha-Silicon Carbide (α-SiC) is one of the most commonly seen polymorphs which generally forms at around 1700 °C and ends up having a hexagonal crystal structure. Whereas, Zinc Blend Structure also known as beta-SiC polymorph (β-SiC) forms at a temperature below 1700 °C [52]. 3C-SiC (α) has a cubic unit cell with three different unit cells being repeated.

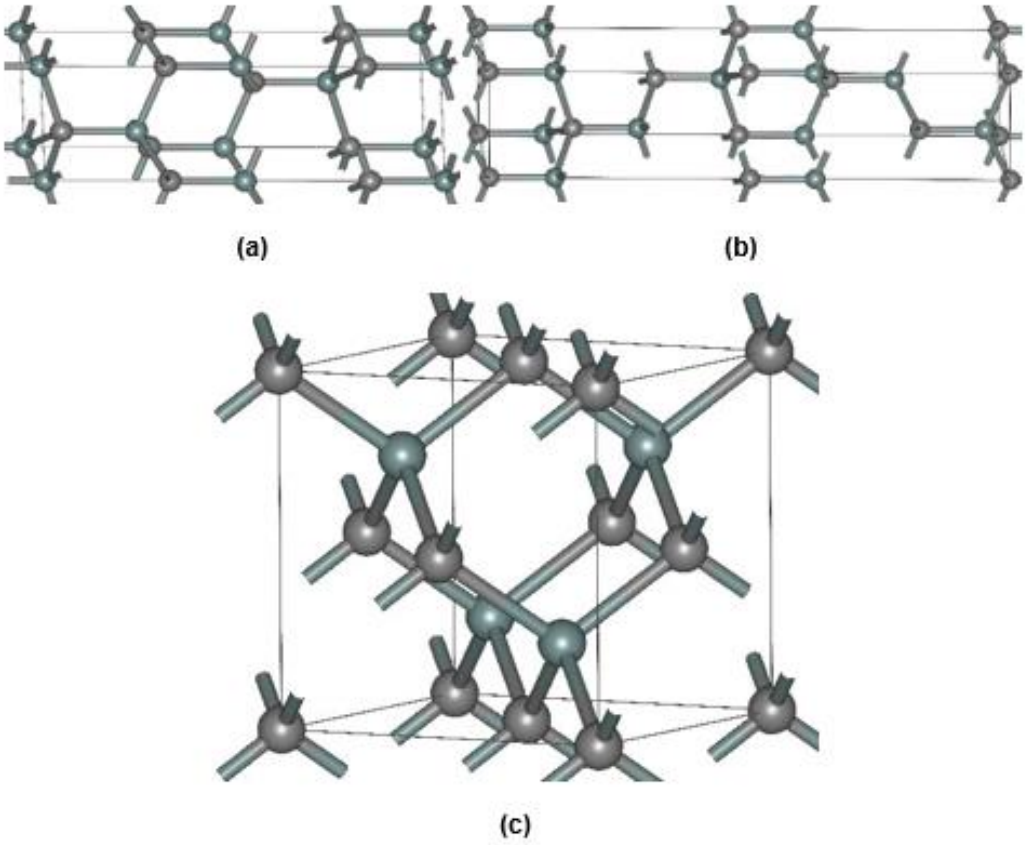

Figure 2-5: (a) 4H-SiC, (b) 6H-SiC(α) and (c) 3C-SiC(β) crystal structure

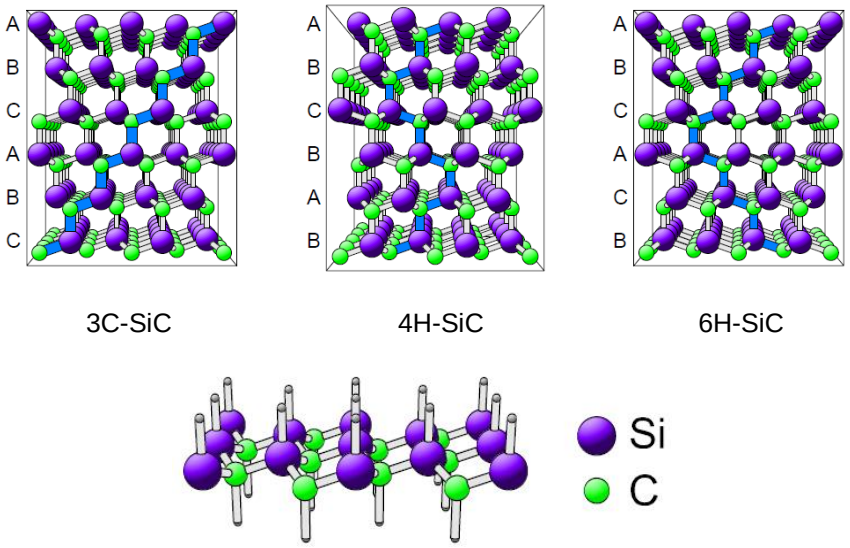

Figure 2-6: SiC crystal polytopes with clear representation of atomistic position of Si and C, [57]

Throughout this research, all the simulation is carried out for 3C-SiC structure. Lattice parameters obtained by different researchers both experimentally and theoretically are listed in Table 2-3-1.

Table 2-3-1: Lattice parameters of Si-C system, reported by different researchers

Material	Method	References	Lattice Parameter a (Å)
Si	Theoretical	[58]	5.432
		[59]	5.433
		[60]	5.435
	Experimental	[61]	5.429
C	Theoretical	[58]	3.56
		[59]	3.561
		[60]	3.607
	Experimental	[61]	3.567
3C-SiC	Theoretical	[58]	4.358 (4.354)
		[59] [62] [63]	4.361
		[64]	4.326
		[65]	4.365
	Experimental	[61]	4.36
	-	[53]	4.3596

2.4 : SiC Phase Diagram, Oxidation Behavior, and Mechanical Properties

Si-C phase diagrams are very important as it provides information on SiC, which is very critical material in high-temperature regime. Turkevich et al. [66] recently developed Si-C phase diagram for SiC at high pressure by using information of phase model and dependence of Gibbs free energy on the temperature and concentration of different phases developed by Grobner et al. for SiC at ambient temperature. Figure 2-7 (a) and (b), below, shows different phases in a Si-C system with respect to temperature and the molar fraction of C at a pressure of 0.1 GPa and 4 GPa respectively.

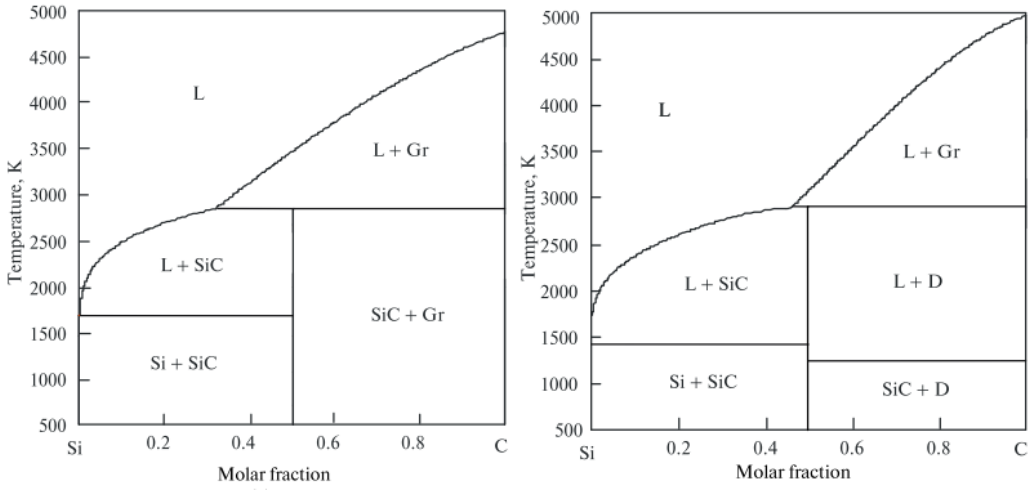

(a) (b)

Figure 2-7: Si-C phase diagram at (a) 0.1 GPa and (b) 4 GPa. [66]

Comparing phase diagrams obtained by different researchers, it is seen that there remains a slight difference in reported Si-C phases depending upon the method by which the phase diagram was produced and on the method by which the SiC powder was produced. Change in phase diagrams can also attribute to different polytypes being generated during the SiC phase formation. As one can see, there are not as many phases for the Si-C system as portrayed for Zr-B system.

SiC is very important material owing to its superior properties like low density, high strength, low thermal expansion, high hardness, high thermal conductivity, high melting point, large bulk modulus, high elastic modulus as well as excellent thermal shock resistance. SiC, when heated above 1350 °C, generates protective oxide scale (SiO_2) over the UHTC material, increasing its oxidation resistance as it prevents oxygen from diffusing further into sub-level material [9]. Opila et al. [69] found that two processes took place constantly one after another. Firstly, generation of protective oxide scale and then formation of gaseous SiO responsible for building above atmospheric pressure due to active oxidation above 1700 °C leading to rupture of the oxide scale.

Yamamoto et al. [68] accomplished consolidation of SiC nano-powder by spark plasma sintering at 1700 °C under 40 MPa pressure for 10 min. They found increment in relative density from 68% to 98% during holding time of 10 minutes and concluded that relative density could be controlled easily by holding time in the sintering process. They also experimentally obtained Vickers hardness, bending strength and Young's modulus of the sintered material and found increment in each with an increase in relative density.

As Yoon soo, et al. [53] studied 3C-SiC is Zinc blende type structure and have space group of T^2_d-F$\bar{4}$3m. 3C-SiC having a B3 phase (i.e., Zinc Blende structure) has been studied by many researchers for its structural and thermal stability and behavior at elevated pressure with the help of ab initio and molecular dynamics simulations [59, 70-75]. Varshney et al. [70] calculated aggregate second order elastic constant C11, C12 and C44, aggregate bulk modulus and Young's modulus and compared it with that of obtained by previous researchers [71-75]. Table 2-4-1 represents them.

Table 2-4-1: β-SiC, Elastic constants, Bulk modulus and Young's modulus reported by different researchers

Method	C11 (GPa)	C12 (GPa)	C44 (GPa)	Bulk Modulus (GPa)	Young's Modulus (GPa)
LDA [84]	436.0	120.0	255.0	225.0	-
MD [72]	390.0	144.0	179.0	225.0	-
DFT [79]	371.0	169.0	179.0	225.0	-
Exp.	390.0 [77]	142.0 [77]	256.0 [77]	227.0 [76]	
	363.0 [79]	154.0 [79]	149.0 [79]	225.0 [80, 81]	-
Exp. (Second order constants)	352.3 [78]	140.4 [78]	232.9 [78]	-	437.0 [82]
Cals. [70]	371.1	223.4	279.3	273.0	-
Calc. (Second order Constants) [70]	676.5	831.0	199.9	28.1	549.0

General mechanical properties are mentioned in Table 2-4-2 below found by different researchers experimentally or theoretically.

Table 2-4-2: General Mechanical Properties

Density [53]	3.21 g/cm^3
Young's Modulus [68]	380 ± 40 GPa
Fracture Toughness [68]	3.6 ± 0.6 MPa.$\sqrt{\text{m}}$
Flexural Strength [68]	520 ± 50 MPa
Vickers Hardness [68]	~20 GPa
Melting Temperature	-
Co-efficient of Thermal Expansion	4.0 x 10^{-6} K^{-1} [67], 4.7 x 10^{-6} [83]
Thermal Conductivity [85]	~170.0 W/mK

In upcoming section different composite systems with ZrB_2, the significance of SiC as an additive and effect of various toughening mechanisms will be discussed.

2.5 : Diboride based Ultra High-Temperature Ceramics and Significance of SiC

In this section, firstly, the phase diagram of the ZrB_2-SiC material system is presented and then along with the processing methods the experimentally and theoretically obtained mechanical properties at ambient as well as elevated temperature is presented. Effect of SiC as an additive will be discussed by comparing various mechanical properties such as Young's modulus, Flexural strength, Fracture toughness and hardness.

Only one phase diagram for the ZrB_2-SiC system could be found, which is shown in Figure 2-8. Seeing the phase diagram, one notices a eutectic point at 2270 °C at 23 % molar concentration of ZrB_2 into the system. A eutectic point is defined as the temperature at which a eutectic mixture changes its phase. Also, the reason why only one phase is labeled into the diagram is that, authors were only interested in studying the system when it turns into liquid [86].

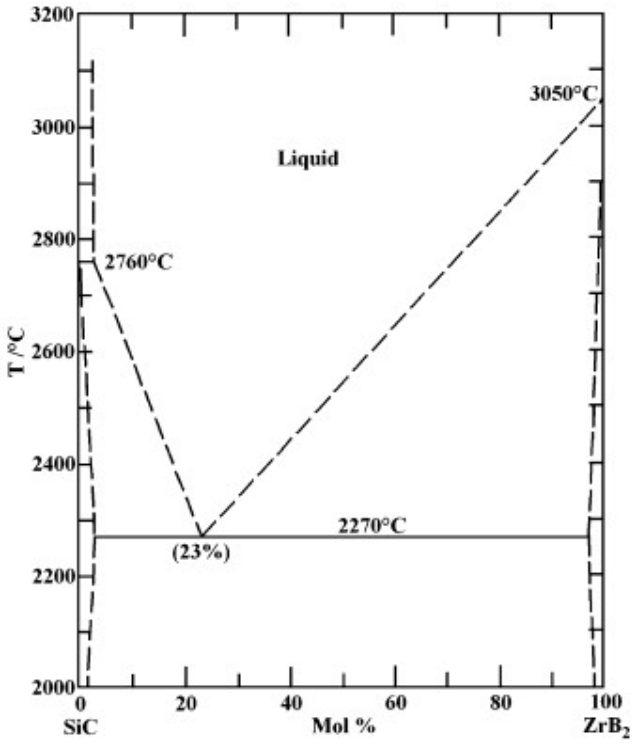

Figure 2-8: ZrB_2-SiC Phase Diagram [86]

Hunt for the material for hypersonic flight systems is continued since 1950. During 1950-1960 Nasa suggested the future need of the material which can hold itself at the temperature as high as 3300 °C. Initial studies during this decade were limited to tungsten, pyrolytic graphite, hafnium carbide and tantalum carbide [87]. During the 1960s, the U.S. Air Force supported numbers of studies to focus on refractory diborides and carbides as a candidate for future materials for aerospace vehicles. Soon, the preparation and characterization, thermodynamic data, reaction kinetics, oxidation of ZrB_2 and HfB_2 and vaporization of refractory compounds such as ZrO_2, HfO_2, ThO_2, ZrB_2, and HfN were studied by various researchers [23,88,90,91]. A number of studies were also made on increasing relative density of the ZrB_2 material and hence increasing desired functional property. One of such studies was carried out by Takashi et al. [92] in which ZrB_2 ceramics were prepared by both hot-pressing and Spark Plasma Sintering methods. They concluded that the average diameter of grains was smaller when obtained through Spark Plasma Sintering technique due to very short sintering time and low temperature and there were no oxygen impurities into the Spark Plasma Sintered ZrB_2 unlike the hot pressed one. The whole point of such study was that smaller grain size elucidates the densification mechanism which is grain boundary diffusion through the liquid film where major impurities are concentrated.

ManLabs, Inc., also did the similar kind of studies for the refractory borides. One of their studies examined early transition metal borides such as TiB_2, ZrB_2, HfB_2, NbB_2 and TaB_2 for potential hypersonic and re-entry structural applications [93]. In a subsequent the effect of boron-to-metal ratio on oxidation behavior, thermal conductivity, emissivity and electrical resistivity were examined [94]. This study also included densification behavior of ZrB_2 under different temperature.

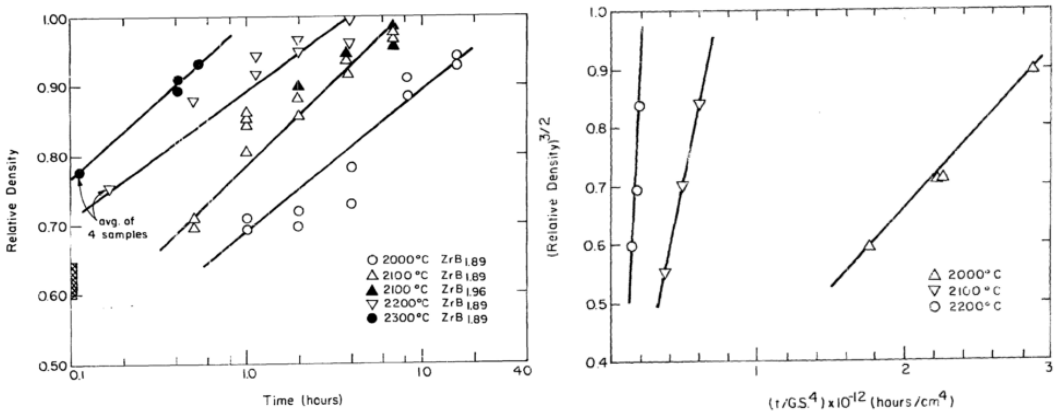

(a) (b)

Figure 2-9: (a) Relative Density with respect to Sintering time for ZrB_2 having different boron to metal ratio, (b) Relative Density Vs. Grain size as a function of densification temperature [94]

In the following study, they investigated the effect of carbon additives on thermal shock resistance and SiC additives on oxidation resistance of the diborides. The presence of SiC was found to be beneficial in oxidation improvement and inhibition of grain growth. Results of oxidation testing of SiC added ZrB_2 was published in series of reports [95,96,97], including one presented by Clougherty et al. [96] justifying SiC additives in diborides. Presented below is Figure 2-10 displaying bend strength of ZrB_2 at different temperature without any additives.

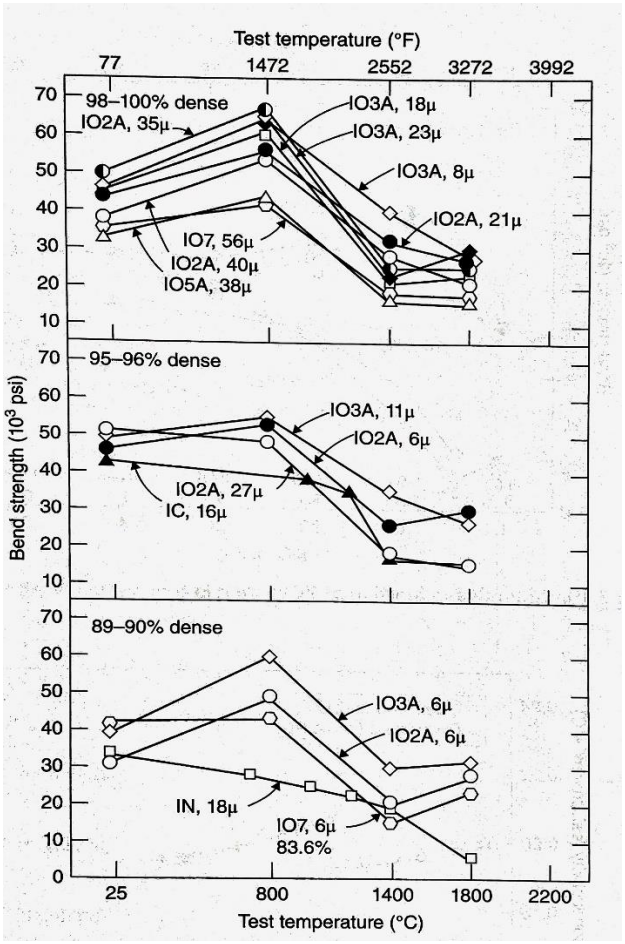

Figure 2-10: Strength Vs. Temperature for nominally pure ZrB_2 [97]

As one can see from figure 2-10, for nominally pure ZrB_2 the strength increased to maximum from room temperature to 800 °C. Strength decreased from 800 °C to 1400 °C and then again increased till 1800 °C. Authors attributed this initial increase in strength from room temperature to 800 °C to the relaxation of residual thermal stresses which may exist due to processing. On the other hand, the increment in strength after 1400 °C was attributed to the plastic behavior of material leading to blunting of the cracks.

Authors reported increment in mechanical strength at elevated temperatures as a result of SiC addition into diborides. They found that SiC contributed in reducing the grain

growth during densification resulting in improved strength at higher temperatures. However, mechanical testing and compressive creep studies done by them revealed increased plasticity is owing to grain boundary sliding as a result of SiC additions. Figure 2-11(a) below, shows increment in bend strength for ZrB_2+SiC compared to nominally pure ZrB_2's data in Figure 2-10. Figure 2-11(b) shows a change in bend strength in diborides due to SiC addition at 99-100% density.

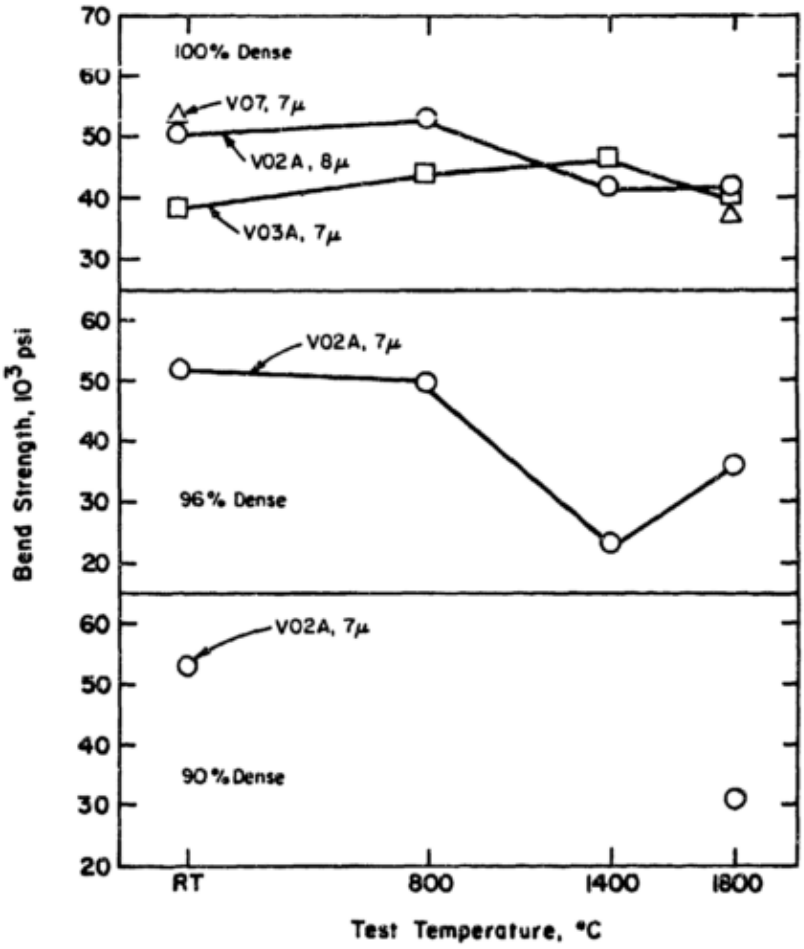

Figure 2-11: (a) Bend Strength of ZrB_2 + SiC (10-50 %vol) Vs. Test temperature [97]

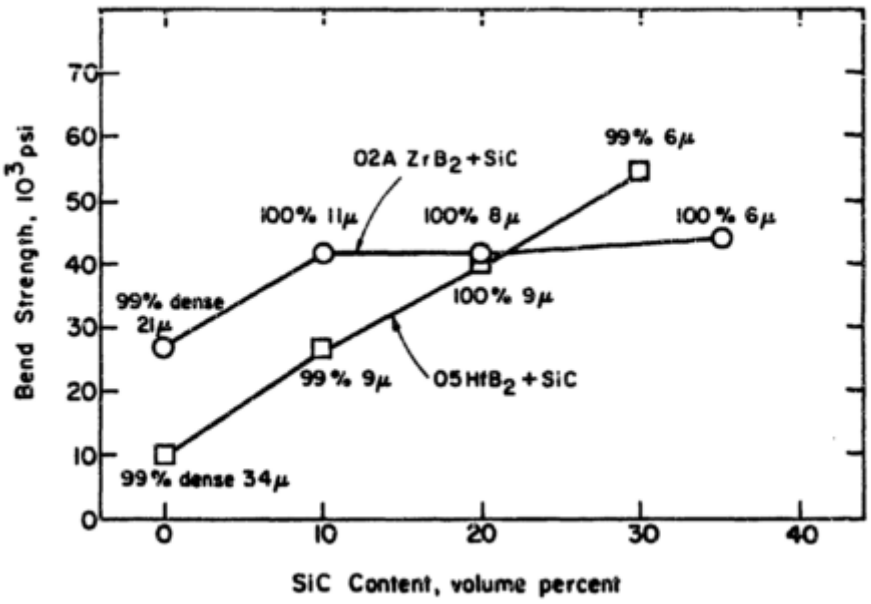

Figure 2-11: (b) Bend strength of diborides (ZrB_2 / HfB_2) as a function of SiC content (99-100 % density) [97]

In one of their last reports as part of ManLabs, Inc. research, Kaufman et. al. [98,99] reported the oxidation behavior of the stated diborides mixed with SiC under high velocity of hot gas environment. They reported that for furnace tests below 2100 °C, the lowest oxidation rates were found when diborides were mixed with 20 %vol SiC. Above that temperature oxidation rates were similar as in nominally pure ZrB_2 due to depletion of SiC from the composites. Initially, at lower temperature oxide scales formed over the surface of materials (e.g. ZrO_2 in the case of ZrB_2 + SiC composites) was found to be puffy and was less protective whereas at high temperature (e.g. above ~1900 °C) the scale was denser and protected the borides.

Hence, one could justify the use of SiC as additives to increase strength and oxidation resistance in harsh environments as well as sintering capability of diborides.

2.6 : ZrB_2-SiC Ceramics' Processing and Microstructure-Property Relation

Considering the literatures, one can find that two of the most common processing methods for ZrB_2-SiC based ceramics are Hot Pressing and Spark Plasma Sintering. Electron Beam Sintering as well as Reactive Spark Plasma Sintering have also been used by some researchers [101,102]. Lots of research has been done on materials processed by Hot Pressing (HP) but the majority preference has been shifted towards spark plasma sintered ZrB_2-SiC in past decade or so. A schematic diagram of Hot pressing machine is illustrated in Figure 2-12 below.

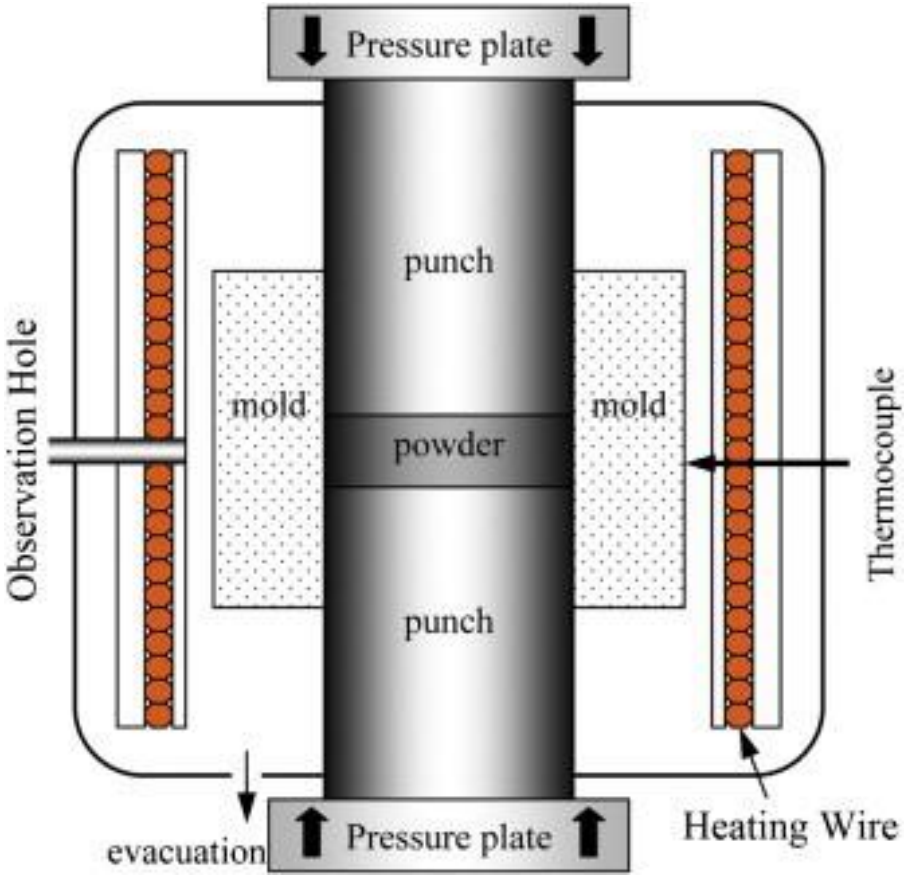

Figure 2-12: Hot Pressing Manufacturing method [103]

The hot pressing machine uses heating elements by which the sample is heated first to the required temperature, and then the pressure is applied by pressure plates under vacuumed condition while the pulsating electric current is passed through the powder under process in Spark Plasma Sintering method for heating purpose which generates discharge within the voids among the particles leading to particle surface activation, local melting, and evaporation on the surface of the powders rendering neck formation between the particles [114]. In addition, the sample (i.e., mixture powder) is placed under externally applied pressure and vacuum during the total processing time. Figure 2-13 illustrates Spark Plasma Sintering process. Some of the merits of using Spark Plasma Sintering process is that pulsating electric current provides higher heating and cooling rates, which significantly reduces the time for production of ZrB_2-SiC ceramics to 1-2 hours instead of the prolonged process of Hot Pressing.

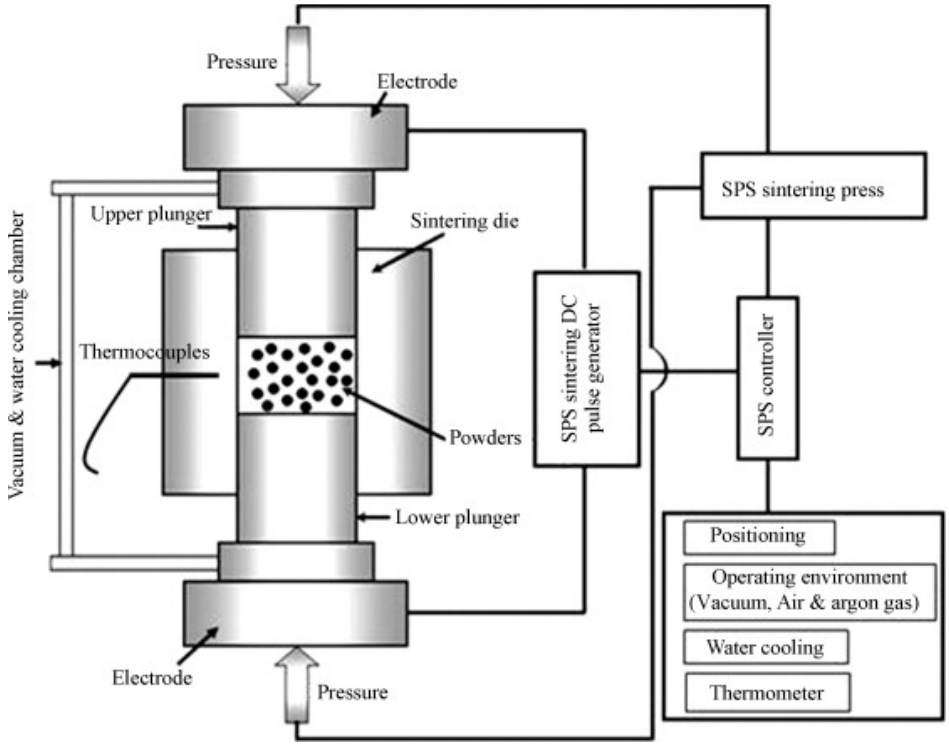

Figure 2-13: Spark Plasma Sintering Process Illustration [104]

Knowing the effect of processing parameters on properties of produced materials is extremely important. Hence, few researchers studied the effect of heating rate and initial composition on produced ZrB_2-SiC ceramics' mechanical properties [105, 106]. The motivation for this research is to find the parameters which can lead to full density material in a shortest amount of time and lowest required process temperature with the desired mechanical properties in Spark Plasma Sintering process. Akin et al. prepared ZrB_2-SiC composites with Spark Plasma Sintering firstly at a temperature of 1800-2100 °C with holding time of 180-300 s under 20 MPa pressure and secondly at a temperature of above 2100 °C without a holding time under 10 MPa with ZrB_2 and 20-60 mass% SiC. While sintering at 2000 °C and 2100 °C for 180 seconds, manufactured samples were found to have 99% relative density with different microstructure compared to samples sintered above 2120 °C [100]. Figure 2-14 and 2-15 shows SEM images of these sintered composites at different temperature and for a different holding time.

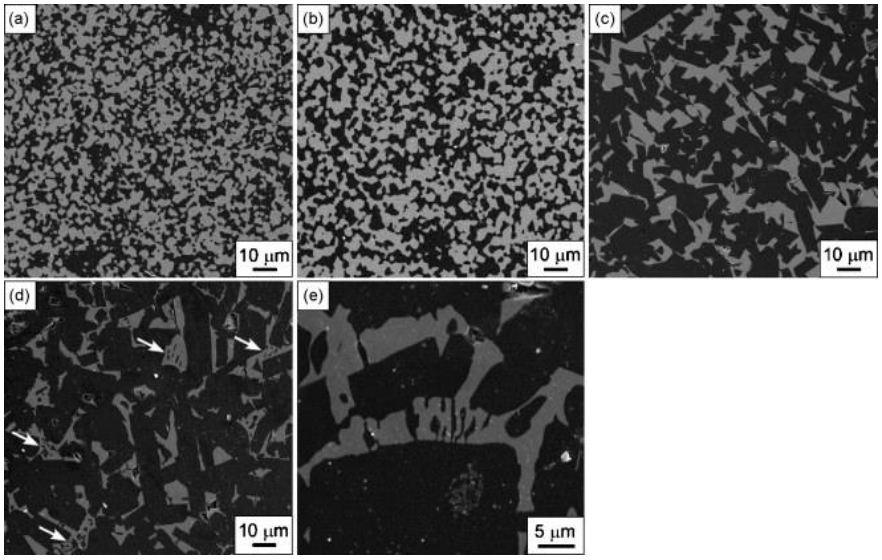

Figure 2-14: SEM images of polished ZrB_2-SiC composites with 40 mass% SiC sintered at (a) 1900 °C for 300 s (b) 2100 °C for 180 s (c) 2120 °C, without holding (d) 2200 °C, without holding and (e) 2200 °C, without holding [100]

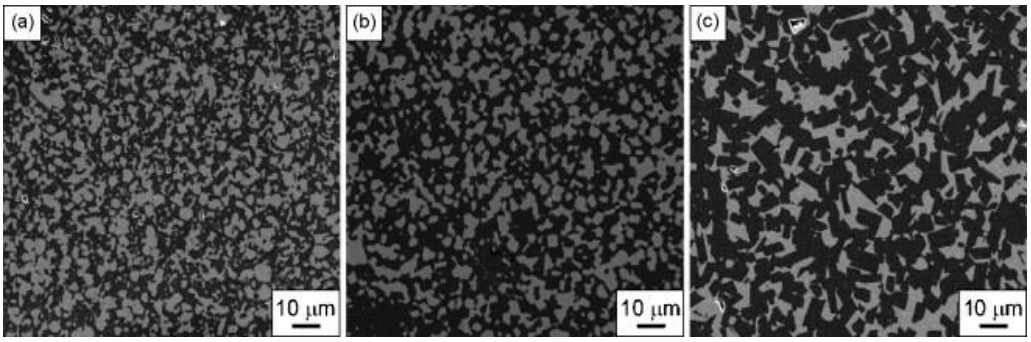

Figure 2-15: SEM images of polished surface of ZrB_2-SiC composites with 50 mass% SiC sintered at (a) 1900 °C for 300 s (b) 2100 °C for 180 s and (c) 2165 °C, without holding

Similarly, Zhang et al. [101] studied the ZrB_2 composites having 10-30 vol% SiC content. The composite material was sintered without any aid of external pressure and achieved near the full density of 97% relatively. While doing flexural tests on the processed composites, they found that adding carbon at 10 %wt of SiC into the composite reduced the flexural strength whereas, the carbon content of 5 %wt of SiC improved material's various mechanical properties such as Elastic modulus, hardness, flexural strength and fracture toughness. Figure 2-16 shows, the microstructure of ZrB_2 ceramics with 10-30 vol% of SiC having 5 wt% carbon. Figure 2-17 shows the Flexural strength of these pressure-less sintered ZrB_2-SiC composites as a function of ZrB_2 and SiC initial grain sizes as well as the concentration of SiC in vol%. They concluded that the strength of hot-pressed ZrB_2-SiC increased with decreasing initial SiC particle size. Using the SiC powder with the middle starting particle size around ~1.05 um resulted in equiaxed SiC grain structure and the smallest ZrB_2 and SiC grains which led to the highest flexural strength of 600 MPa compared to composites made with finer or coarser particles of SiC.

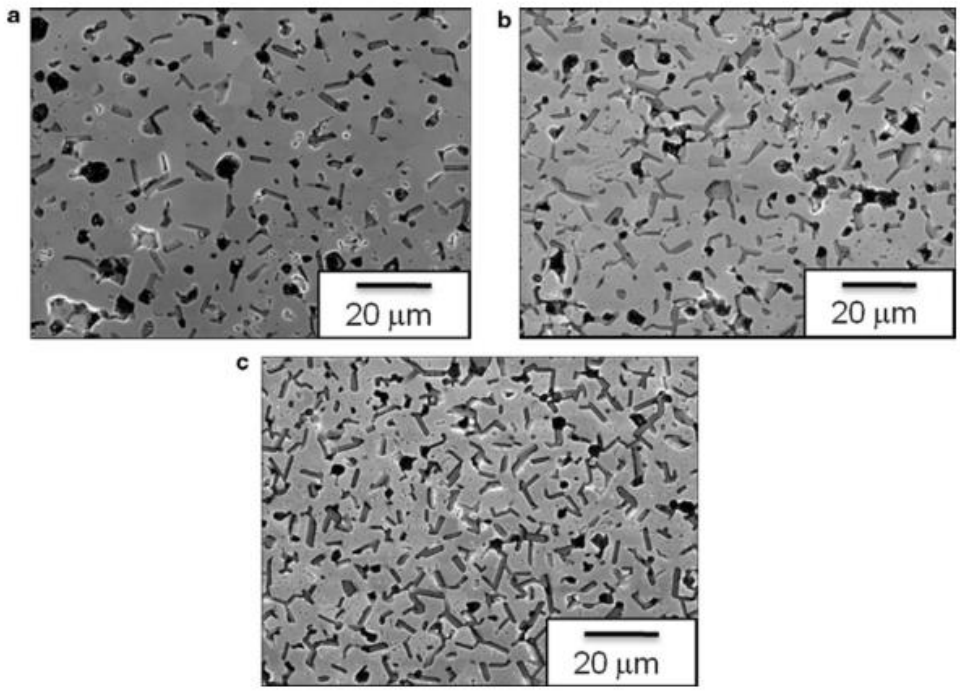

Figure 2-16: Microstructure of ZrB_2 ceramics containing (a) 10 vol% (b) 20 vol% and (c) 30 vol% SiC with 5 wt% of carbon [101]

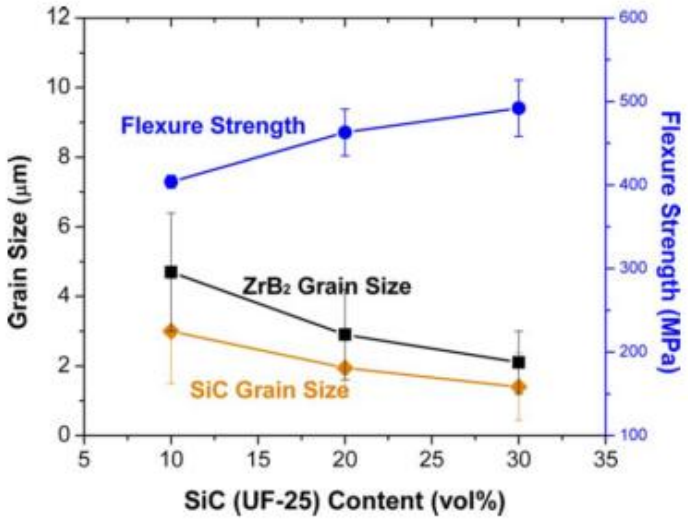

Figure 2-17: Flexural Strength at room temperature as a function of initial ZrB_2-SiC grain sizes and SiC volume fraction [101]

As discussed earlier Young's Modulus for ZrB_2 and SiC was found to be around ~490 and ~380 respectively from different researchers. From the theory of mixers, one can say that the composite made from mixing of these two will yield Yong's modulus somewhere near more than SiC's and little lesser than ZrB_2's. Many researches have been carried out to analyze mechanical properties under different process parameters and usage environments, some of them are mentioned in upcoming tables. Table 2-6-1 represents data obtained by Watts et al. [107]. It shows that with a decrease in SiC maximum grain size there was an increment in strength, hardness and Young's modulus of composite ceramic. UF-25 refers to material samples prepared by attrition milling of ZrB_2 and SiC powder, and UF-10 and UF-5 refer to Ball Milled samples of ZrB_2 and SiC powder. Composition M1, M2, M4, M8, and M0 were prepared by 1, 2, 4, 8 hours of ball milling and no ball milling respectively.

Table 2-6-1: Mechanical Properties of ZrB_2-SiC ceramics for different SiC particle size (All sample contains 30 vol% SiC) [107]

Composition	Maximum SiC particle size (um)	Strength (MPa)	Elastic Modulus (GPa)	Vickers Hardness (GPa)	Knoop Hardness (GPa)
UF-25 grade (HC Starck SiC)	4.4	1150 ± 115	541 ± 22	21.4 ± 0.6	17.2 ± 0.2
UF-10 grade (HC Starck SiC)	6.4	924 ± 100	532 ± 13	21.7 ± 0.6	17.1 ± 0.3
UF-5 grade (HC Starck SiC)	8.2	892 ± 120	534 ± 20	21.2 ± 0.4	17.0 ± 0.2
M8 Unasil 600 Green (Universal Photonics)	11.5	825 ± 118	531 ± 14	21.2 ± 0.6	17.1 ± 0.3
M4	11.8	724 ± 83	520 ± 12	19.3 ± 1.8	16.1 ± 0.3
M2	12.0	460 ± 47	518 ± 16	18.6 ± 0.5	15.6 ± 0.4
M1	13.0	280 ± 34	505 ± 7	18.4 ± 1.3	15.6 ± 0.4
M0	18.0	245 ± 23	484 ± 6	17.3 ± 1.4	15.2 ± 0.3

There is plenty of literature which reported mechanical properties such as Elastic modulus, Vickers Hardness, fracture toughness etcetera for particulate ZrB_2-SiC ceramics. Some of them are gathered by E. Neuman and G. Hilmas [89], which are presented below in Table 2-6-2.

Table 2-6-2: Various mechanical properties of particulate ZrB_2-SiC ceramics [89]

Composition	ZrB_2 + 10SiC (vol%)	ZrB_2 + 15SiC (vol%)	ZrB_2 + 20SiC (vol%)	ZrB_2 + 30SiC (vol%)
Relative Density (%)	-	96.5	-	-
	93.2		97.3	97.2
	97.1		99.7	97.5
	97.4	99	99.7	99.8
				99.4
	99.8		5.62 g/cm^3	99.8
				>99
ZrB_2 Grain size (um)	3	4.4 ± 1.7	1.8	3
	~3		4.2 ± 1.9	2.2 ± 1.2
	2.2		~3	3.9 ± 0.9
	4.5 ± 1.6	2	4.0 ± 1.1	1.5 ± 1.2
				~3
	4.3 ± 1.4		4.1 ± 0.9	1.2 ± 0.4
				10.6
SiC Grain size (um)	-	0.9 ± 0.5	~0.2	~0.2
	-		0.9 ± 0.5	1.2 ± 0.6
	~0.2		-	-
	0.8 ± 0.4	-	-	-
				-
	-		-	1.0 ± 0.4
				1.6
Elastic modulus (GPa)	507 ± 4	-	-	-
	450		-	516 ± 3
	-		466	487 ± 12
	-	480 ± 4	506	510
				-
	500 ± 16		505 ± 3	520 ± 7
				541 ± 22
Hardness (GPa)	-	-	-	-
	24 ± 0.9		-	20 ± 0.2
	-		24 ± 2.8	24.4 ± 0.6
		17.7 ± 0.4		24.0 ± 0.7
	18 ± 0.9		21.3 ± 0.7	20.7 ± 1.0
				21.4 ± 0.6

Table 2.6.2 – *Continued*

Fracture Toughness (MPa.$\sqrt{m}$)	4.8 ± 0.3 [a]	-	6.8 ± 0.1 [c]	5.9 ± 0.2 [c]
	4.1 ± 0.3 [b]		-	5.5 ± 0.3 [b]
	5.7 ± 0.2 [c]		4.4 ± 0.2 [b]	4.4 ± 0.5
	-	4.1 ± 0.1 [a]	4.2 ± 0.8	2.1 ± 0.1
				5.3 ± 0.5 [b]
	3.8 ± 0.3		3.9 ± 0.3	4.6 ± 0.1 [b]
				-
Flexural Strength (MPa)	835 ± 35	714 ± 59	1009 ± 43 [d]	860 ± 70 [d]
	713 ± 48		608 ± 93	1063 ± 91
	720 ± 55 [d]		1003 ± 94 [d]	425 ± 35 [d]
	524 ± 63	795 ± 105	487 ± 68 [d]	800 ± 115
				1089 ± 152
	393 ± 114 [d]		937 ± 84 [d]	909 ± 136
				1150 ± 115

a: Chevron notched beam
b: Indentation strength in bending
c: Single-edge notched beam
d: Three-point flexure

Drawing onto the toughening mechanism for ceramic materials, a promising approach from recent developments, is by fabricating laminated structure at micro level to improve the toughness of ceramics [108]. Using stronger matrix layers and comparatively weaker interlayers alternatively have been successfully implemented by several researchers and have shown some promising improvements in mechanical as well as other properties of such composites. Some of such studies includes laminated SiC/TiB2, Al_2O_3/ZrO_2, Si_3N_4/BN, ZrB_2/SiC, ZrB_2-SiC/BN in ceramic/ceramic multilayers [109-119] and Cu/TiN, Ti/TiN, Nb/NbC, Al/TiN in metal/ceramic multilayers. The main advantage of these laminated structure is that it helps ceramic composites to absorb more energy and gives ability to resist catastrophic failure ultimately leading to higher fracture toughness. Composition and structure of Si_3N_4/BN laminates were controlled and apparent fracture toughness of 15.1 MPa.$\sqrt{m}$ was achieved by Huang and Wang [123, 124]. Wang achieved

even higher fracture toughness of 28.1 MPa.$\sqrt{m}$ by adding secondary phase of whisker SiC to BN interface.

Owing to these noticeable improvements due to laminated compositions, many researchers have tried to fabricate ZrB_2 based laminated composites with various additives and/or interlayers [114-119]. By making layered ceramics, the strength is enhanced due to implemented low energy paths for crack propagation or presence of residual stresses into the system. H. Wang et al. fabricated SiC/ZrB_2 laminated ceramic by roll-compacting and spark plasma sintering at 1600 °C [114]. They were able to fabricate laminated SiC/ZrB_2 ceramic having different SiC concentration. ZrB_2 powder, having ~95% purity with ZrO2 as the main impurity and mean particle size of ~6.7 µm was mixed with β-SiC powder having 99.9 % purity with a mean particle size of 1 µm. Matrix layered comprised ZrB_2 powder with 10 vol% of SiC whiskers and 10 vol% SiC particles whereas interlayers (i.e., weak layers) comprised of SiC and 0-50 % ZrB_2 powder. SiC whiskers and particles, after dispersing into ethanol by the ultrasonic device were mixed with ZrB_2 for 4 hours of ball milling, after which, a mixture containing sufficient binding agents was roll-compacted until ~0.2 mm thick matrix sheets were formed. Matrix layers were then dip-coated with the slurry containing SiC, 0-50% ZrB_2 powder and binders resulting in the interlayers upon heating. Their flow chart adapted for fabrication of laminated SiC/ZrB_2 ceramic has been displayed below in figure 2-18. Figure 2-19 represents SEM images of the produced laminated SiC/ZrB_2 ceramic.

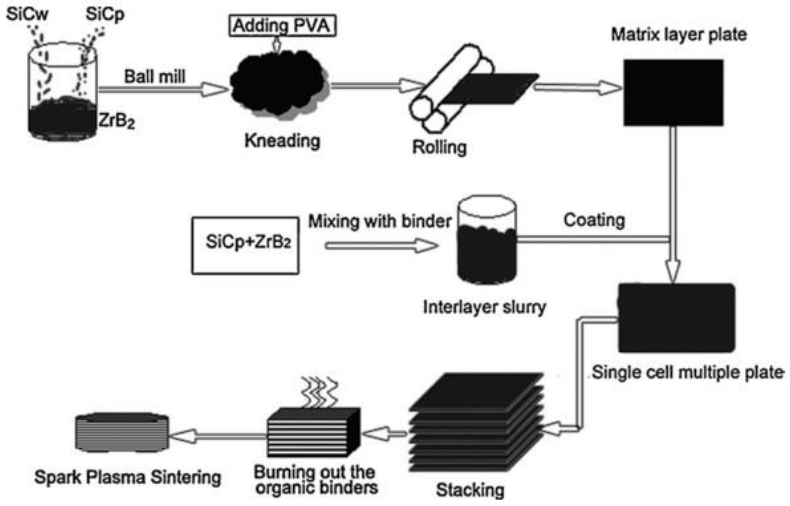

Figure 2-18: Overview of fabrication method adapted by Wang et al. for the ZrB_2/SiC laminated ceramic [114]

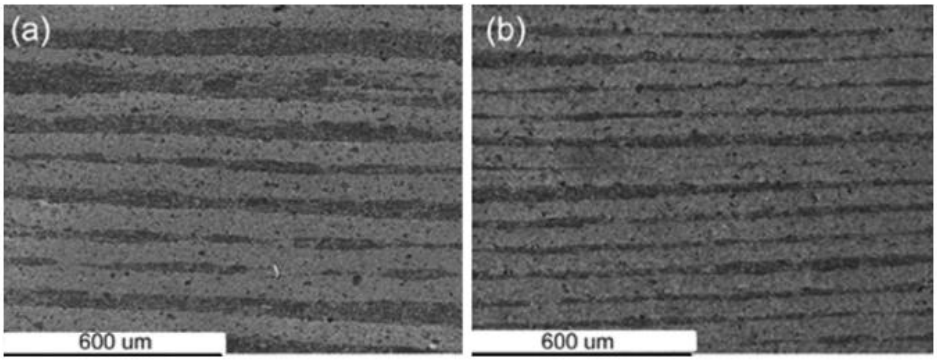

Figure 2-19: Produced laminated SiC/ZrB_2 samples (a) ZSSPS1 and (b) ZSSPS2 [114]

They were able to achieve apparent fracture toughness as high as 12.3 ± 0.3 MPa.$\sqrt{m}$ for laminated SiC/ZrB_2 ceramics and concluded that, the material demonstrated non-catastrophic failure behavior due to increased fracture toughness. The observed advance in fracture energy was attributed to the delamination and deflection of crack. Table 2.6.3 represents several mechanical properties obtained for these laminates. Since the interlayer is the weaker of the two, the material's capability is better assessed as function

of material proportions in interlayer. As one can see, increasing the concentration of ZrB_2 up to 30% increased the fracture toughness, after which it had detrimental effect on the ceramic.

Table 2-6-3: Mechanical properties of ZrB_2/SiC laminated ceramic fabricated by Wang et al. [114]

Sample Names	ZSSPS1	ZSSPS2	ZSSPS3	ZSSPS4	ZSSPS5
Composition	SiC	SiC ± 10%ZrB_2	SiC ± 20%ZrB_2	SiC ± 30%ZrB_2	SiC ± 50%ZrB_2
Bending Strength (MPa)	216 ± 75	117 ± 98	388 ± 44	379 ± 64	277 ± 26
Fracture Toughness (MPa.$\sqrt{m}$)	6.1 ± 0.3	6.9 ± 0.2	9.9 ± 0.4	12.3 ± 0.3	7.8 ± 0.8
Elastic Modulus (GPa)	550	543.7	537.4	531.3	519.1
Poisson's ratio	0.14	0.143	0.146	0.149	0.155
Co-efficient of Thermal Expansion ($x10^{-6}\ K^{-1}$)	4.7	4.9	5.1	5.3	5.7
Tensile stress in Matrix layer (MPa)	261	227	193	160	95
Compressive stress in interlayer (MPa)	-1331	-1158	-984	-816	-485

The study presented above is relatively new and represents highest achieved apparent fracture toughness for the laminated ZrB_2/SiC ceramics prepared by Spark Plasma Sintering technique. But a lot of studies has been done on hot-pressed laminated ZrB_2/SiC composites which will be presented now. Zhou et al. [116] produced laminated ZrB_2-SiC ceramics by stacking layers having different SiC concentration in ZrB_2 phase to develop residual stress profile through the material system. ZrB_2 and SiC powders were first ball-milled, then layers containing a different concentration of SiC (vol% 20 and 30) were stacked upon each other in a graphite mold and were hot pressed at 1950 °C and 30

MPa for 60 minutes in Ar atmosphere. Figure 2-20 below shows SEM images of samples produced by Zhou et al.

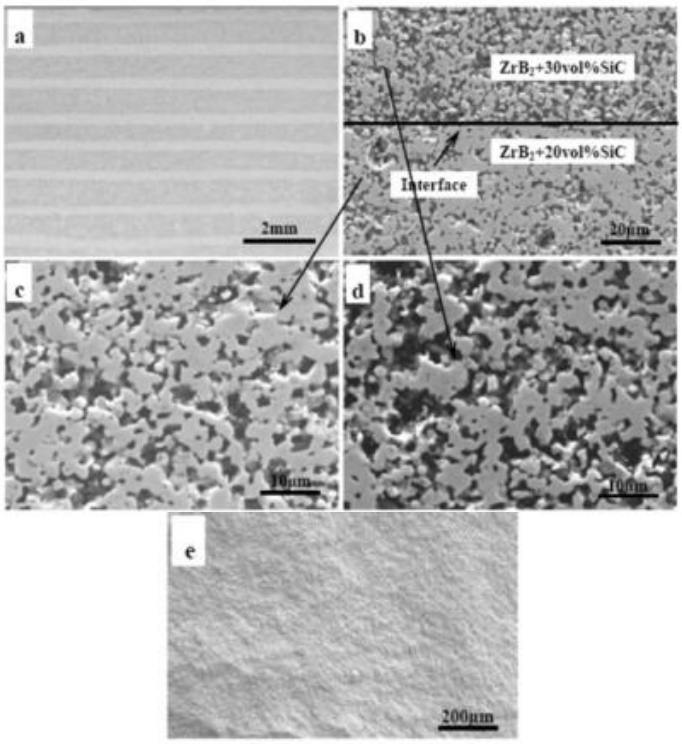

Figure 2-20: ZrB_2/SiC laminated ceramic (a) Optical micrograph of cross-section (b-d) SEM images of the system (e) fracture in monolithic ZrB_2-SiC composite [116]

The flexural strength and fracture toughness were measured with the help of three-point bending, and single-edge notched beam on 3 x 4 mm x 36 mm bars and 2 x 4 mm x 22 mm bars respectively. Table 2.6.4 compares flexural strength and fracture toughness of laminated ZrB_2/SiC ceramics to the monolithic ZrB_2-SiC ceramic material.

Table 2-6-4: Mechanical Properties of the laminated ZrB_2-SiC and monolithic ceramics [116]

Sample	Laminated ZrB_2-SiC ceramic	ZrB_2 + 30 vol.% SiC monolithic ceramic	ZrB_2 + 20 vol.% SiC monolithic ceramic
Flexural Strength (MPa)	960 ± 84	517 ± 63	362 ± 39
Fracture Toughness (MPa.$\sqrt{m}$)	8.8 ± 0.3	5.6 ± 0.5	4.8 ± 0.5

As visible from the tabulated data, Flexural strength and fracture toughness of laminated ceramic composite are much larger compared to its monolithic composition. The improvement in listed properties is attributed to the presence of the residual stresses that came into action due to the thermos-elastic mismatch between adjacent layers, reported the authors. They also mentioned that, the fracture toughness of specimens having crack tips in layers under compression (8.8 ± 0.3 MPa.$\sqrt{m}$) is higher than that of specimens having crack tips in layers under tension.

Interest into the laminated ceramic is high since the strength of these laminated ceramics might not be as high as the monolithic constituent material but the ability to deform without failing catastrophically and energy absorbed before their failure are incredibly high. A similar study as performed by Zhou et al. as presented above was performed by Zhang et al. by preparing ZrB_2-SiC laminated ceramics by hot-pressing while superimposing ceramic layers comprising different material concentrations. Their objective was to use residual surface compression as a toughening mechanism in laminated ZrB_2/SiC ceramics. Their study extended to capture the effect of layer thickness ratio on residual stresses and ultimately on fracture toughness of the laminated ceramics compared to their study performed earlier with Zhou et al. [117]. The toughening effect of residual

compressive stresses was verified by the appearance of crack deflection and pop-in event reported Zhang et al.

ZrB_2 and SiC powders were first ball-milled at 220 rpm for 10 hours with ethanol as grinding media and then put into graphite mold after evaporating the solvent. The hot-pressing of this mixture was performed at 1950 °C and 30 MPa for 60 minutes in Ar environment. Nine specimens were fabricated in total with varying concentration of constituent material (mainly SiC) such as it introduced residual stresses due to the difference in coefficient of thermal expansion between two adjacent layers. In all nine specimens compressive layer was made of ZrB_2 and 30 vol% SiC whereas the tensile layer was formed with ZrB_2 and 10 vol% SiC for sample LZS-1 and 20 vol% SiC for LZS-2-9 but with varying thickness with respect to compressive layer. They measured both intrinsic fracture toughness K_0 of the monolithic sample and the apparent fracture toughness K_{IC} of the laminated sample with the single-edge notched beam. The concept is for laminated ZrB_2-SiC ceramic with residual stresses, the stress intensity factor at the tip of the crack as a function of crack length, is given by $K_{tip}(a)$, which is further summation of externally applied stress intensity factor $K_{appl}(a)$ and internal residual stress intensity factor $K_{res}(a)$. To elaborate when a crack propagates through the compressive layer, the presence of residual stresses and stress intensity factor due to it cause a negative contribution to tip stress intensity factor, leading to increment in fracture toughness of the material. Apart from this, elastic modulus was measured by a three-point bending test. Figure 2-21 displays optical micrographs of samples LZS1-9 prepared by Zhang and team.

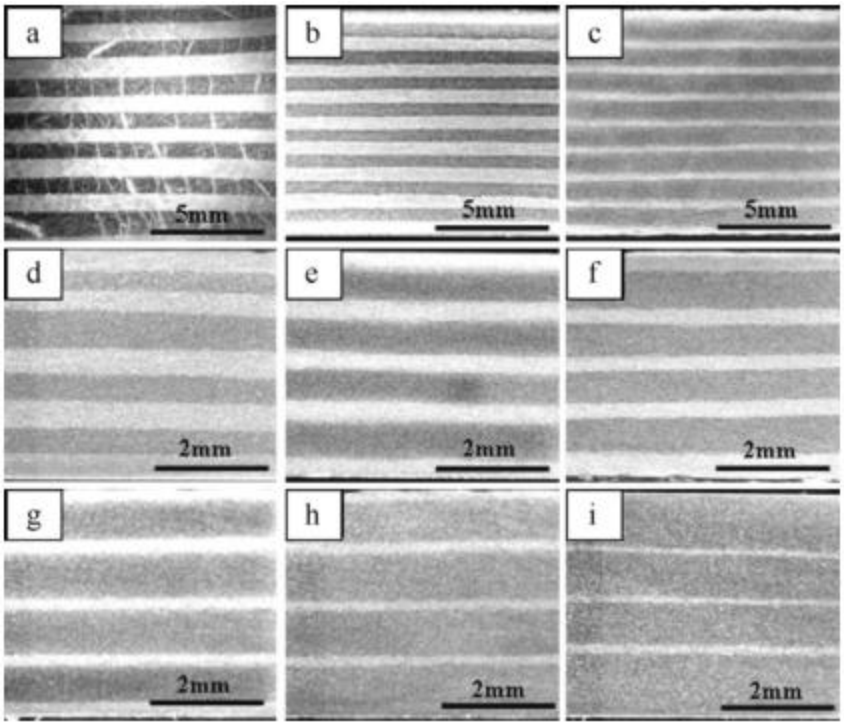

Figure 2-21: Optical micrographs of (a) LZS-1 [10 vol%, 0.89] (b) LZS-2 [20 vol%, 0.89] (c) LZS-3 [20 vol%, 1.78] (d) LZS-4 [20 vol%, 1] (e) LZS-5 [20 vol%, 1.5] (f) LZS-6 [20 vol%, 2] (g) LZS-7 [20 vol%, 2.5] (h) LZS-8 [20 vol%, 3] (i) LZS-9 [20 vol%, 5]; *brackets contains content of SiC in Tensile layer and Layer thickness ratio respectively*

[117]

As one can see from Figure 2-21 (a), there are many cracks present through the tensile layers in LZS-1 sample but there are not many in rest of the samples, confirming that, the thermal coefficient setting is very crucial and effective in laminated ceramics. Zhang et al. also studied the residual stresses as a function of layer thickness ratio and concluded that higher layer thickness ratio (λ) resulted into higher residual compressive stresses. However, the highest fracture toughness did not correspond with the highest

residual compressive stress. This phenomenon can be better understood by the figure 2-22 given below.

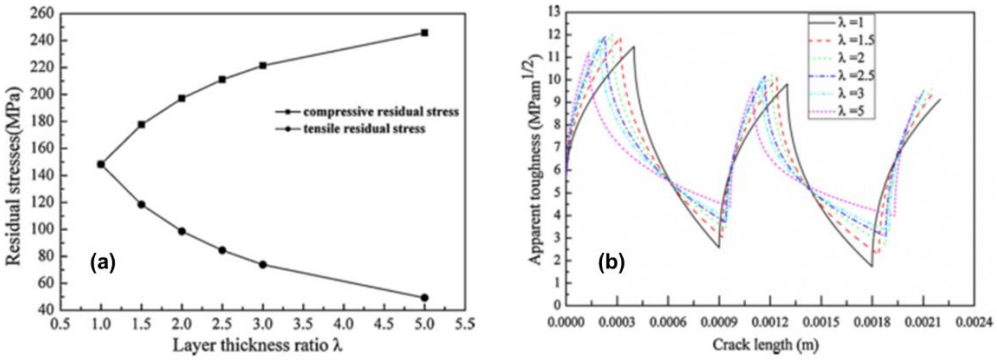

Figure 2-22: (a) Residual stresses as a function of layer thickness ration (b) Crack length and apparent fracture toughness for samples with different layer thickness ratio

Zhang commented that, the laminated ZrB_2-SiC architecture maximized the apparent toughness at the first interface, and increased toughness was observed in the compressive layers with increasing crack length, which reached a local maximum at the ZrB_2 + 30 vol% SiC / ZrB_2 + 20 vol% SiC interfaces and gave local minimum at the interface of ZrB_2 + 20 vol% SiC/ZrB_2 + 30 vol% SiC. To express the significant difference between crack propagation in monolithic and laminated ceramics, the SEM images of cracked monolithic ceramics (Figure 2-23, e and f) and laminated ceramic (Figure 2-23, a, b, c and d) was given with their load-displacement curve produced by three-point bending test with the single-edge notched beam. As one can see, crack propagation was shifted due to the presence of residual stresses. Load-displacement curve in Figure 2-23 a-d corresponds to the LZS-9 sample which had composition of ZrB_2 + 30 vol% SiC (visible as dark phase)/ ZrB_2 + 20 vol% SiC (visible as light and thicker phase). The picture in the picture represents the SEM images of cracked laminated ceramic during SENB test. Comparing them with figure 2-23 e and f, one can see, there is no crack deflection present in monolithic material

compared to the laminated one. Moreover, Zhang commented that the modes of propagation of these cracks depended upon the location of their tips. For example, when located in the compressive layer (e.g., Figure 2-23 b and c), the initial crack deflection took place at tips whereas crack just penetrated through the tensile layers when tips were located into the tensile layers (e.g., Figure 2-23 a). The load-displacement curves also showed stepped response with pop-in event corresponding to change in crack propagation direction after a certain amount of load. It represented that the catastrophic failure did not happen even after first crack deflection due to the presence of internal compressive residual stresses. Hence, Zhang concluded that the change in crack propagation direction implied that the residual compressive stresses could weaken the driving force responsible for crack propagation and fracture enhancing the crack resistance, making the laminated ceramics having strong interfaces with high fracture toughness.

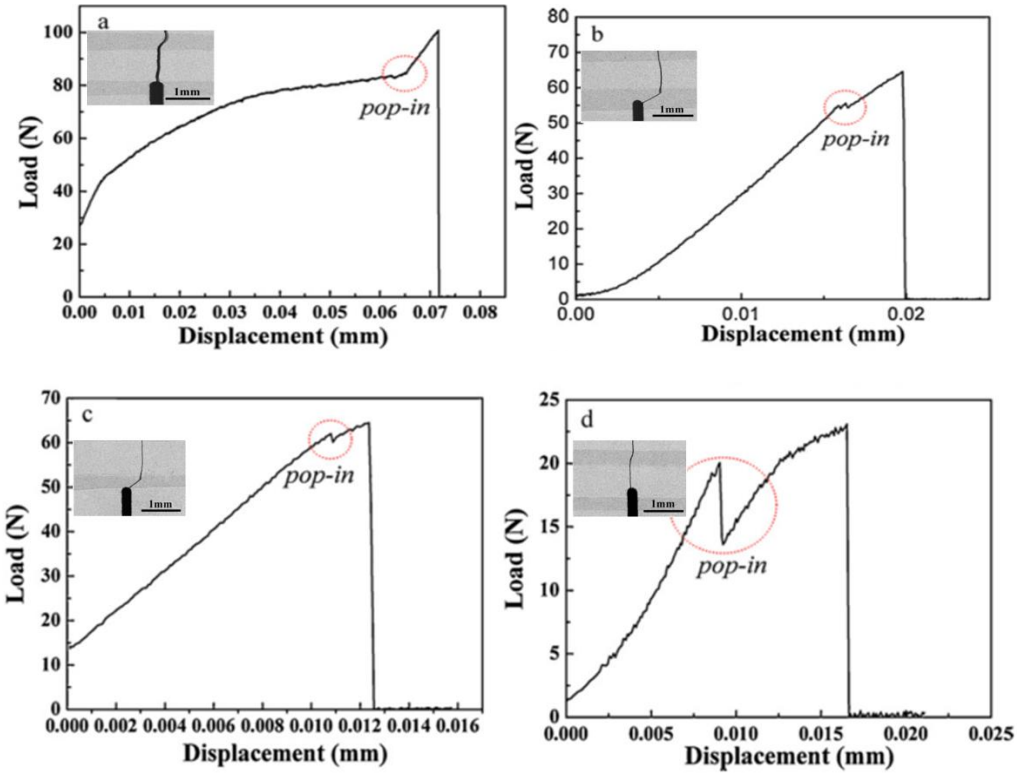

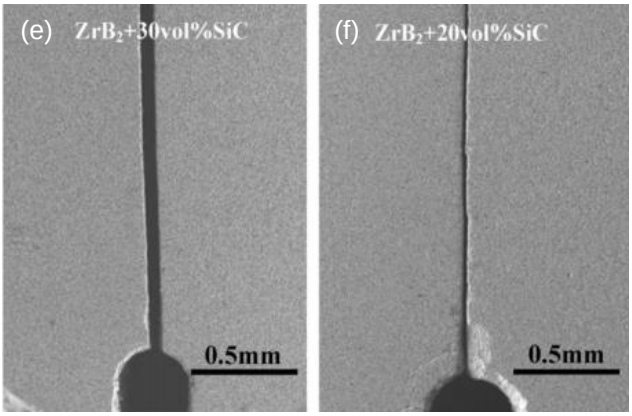

Figure 2-23: (a)-(d) Load-Displacement curves for LZS-9 sample having different crack tip position (e) Crack propagation in monolithic ZrB_2 + 30 vol% SiC (f) Crack propagation in monolithic ZrB_2 + 20 vol% SiC (SEM images after SENB test)

L*ü* et al. [115] studied oxidation behavior of ZrB_2-20 vol% SiC and ZrB_2-30 vol% SiC ceramics at 1500 °C. Based on these oxidation results they were able to decide the sequence for laminated ZrB_2-SiC ceramics such as it can have lower weight gain in the presence of oxidizing temperature and it can have higher residual stresses ultimately leading to toughening of the ceramics. Show in figure 2-24 below is the weight gain by the ceramic due to grain growth of SiC in undertaken composite systems ZrB_2 + 20 vol% SiC (ZS20) and ZrB_2 + 30vol% SiC (ZS30). L*ü* mentioned that, the flexural strength of ZrB_2-SiC ceramics was controlled by the size of SiC grains. In the case of ZrB_2 + 30 vol% SiC, the SiC particles in the matrix formed large agglomerated, leading to decrement in mechanical performance of the material. Conducting the oxidation experiments Lu reported, the outer layer of SiO2 on the surface of ZrB_2-SiC ceramics which acted as a barrier to oxygen diffusion and resulted into passive oxidation protection. For both the material case undertaken ZS20 and ZS30, the parabolic weight gain kinetics were visible

through the mass gain curve obtained. Oxidizing both the samples at 1500 °C for 10 hours, the weight gain by ZS20 and ZS30 was 7.55 mg/cm^2 and 6.59 mg/cm^2 respectively.

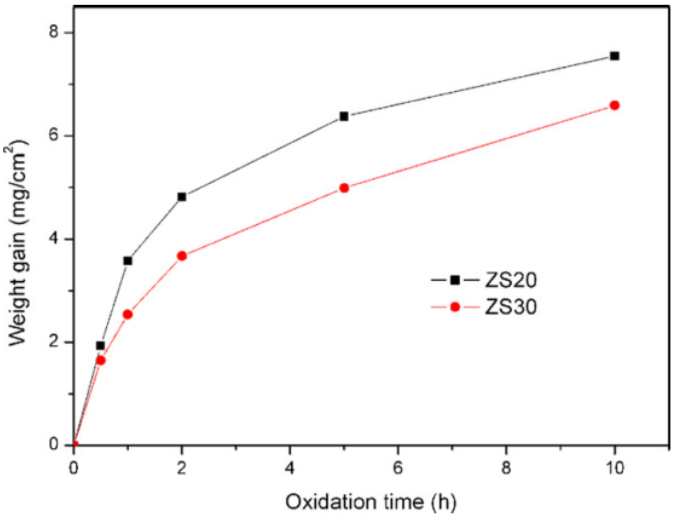

Figure 2-24: Weight gain with oxidation time [115]

Concluding from this result, Lu et al. selected ZrB_2 with 30 vol % SiC as outer laminate and fabricated laminated symmetric ceramic composite consisting ZS30/ZS25/ZS30 structure. Several mechanical properties were obtained for the selected laminate which is presented in Table 2-6-5. Similarly, as Zhang et al. Lu and team also varied the layer thickness ratio and observed its influence on the mechanical properties of fabricated laminated ceramics. On the contrary, to Zhang's work, they found decrement in residual compressive stress with increment in layer thickness ratio.

Table 2-6-5: Mechanical Properties of laminated ceramic composite ZS30/ZS25/ZS30 [115]

Layered Ceramic Composition	Layer Thickness Ratio	Residual Compressive Stress (MPa)	Flexural Strength (MPa)	Fracture Toughness (MPa.$\sqrt{m}$)
ZS30/ZS25/ZS30	1	56	562.6 ± 36.1	10.03 ± 1.26
ZS30/ZS25/ZS30	0.5	78	580.1 ± 36.4	10.73 ± 0.91

Table 2.6.5 – *Continued*

ZS30/ZS25/ZS30	0.2	102	596.3 ± 27.2	9.53 ± 0.93
ZS30/ZS25/ZS30	0.1	114	624.1 ± 63.5	8.47 ± 1.14

Some researchers have also carried out a first-principles studies on bond energy between ZrB_2 and SiC by Density Functional Theory and Crack propagation in different laminated ceramics by molecular dynamics [120-122], which will be discussed in detail in upcoming sections since the main interest of this research is in assessing molecular dynamics simulations as an experimental tool.

These were some of the studies which talked about the effect of ZrB_2 and SiC concentration, their initial grain size, process parameters such as fabrication technique and externally applied environment (i.e., pressure and temperature), oxidizing/ablative environment, laminated architecture, crack tip position and residual stresses in produced ceramics on several mechanical properties. Effect of particulate phase and a laminated structure in the produced ceramics have already been discussed, but there is number of another toughening mechanism which helps in increasing mechanical properties and is researched by many people over the time. Structures found in nature, such as biological hard tissues, shells, and teeth, are made of layered architecture-combining materials with different properties that lead to laminates with different propertied leading to mechanical behavior superior to their constituents. Other examples are certain tree branches with fibrous media to give exceptional strength to highly tensile environment. The point is, these kinds of structures found in nature is the source of inspiration for humankind to imitate them into the synthesized materials. Soboyejo et al. gave a nice brief representation of toughening mechanism undertaken by different material researchers over the years [7].

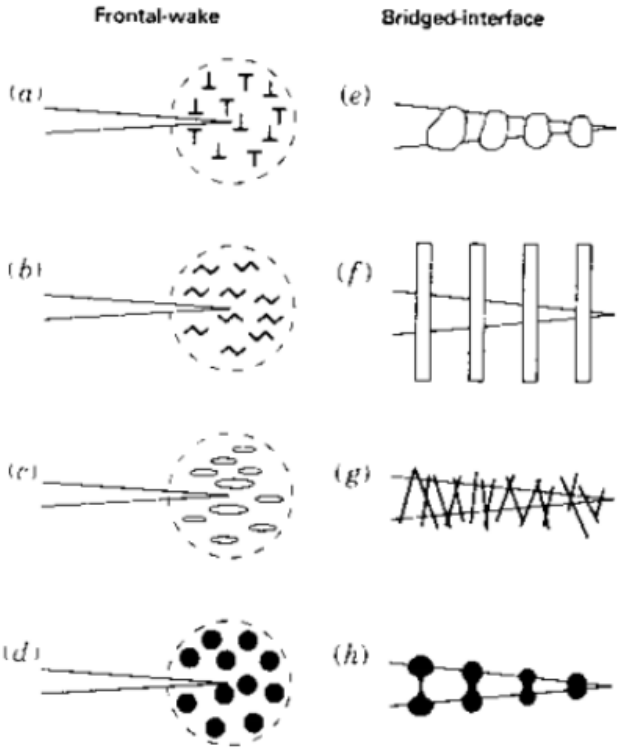

Figure 2-25: Crack-tip shielding mechanisms by, Frontal Zone (a) dislocation cloud (b) micro-crack cloud (c) phase transformation (d) ductile-second phase and by, Crack-wake bridging zone (e) grain bridging (f) continuous fiber bridging (g) short-whisker bridging (h) ductile second phase bridging [7]

Apart from making laminated ceramics, researchers have tried many other conventional ways to toughen the materials, such as incorporation of fibers [125], whiskers [32, 126, 127], particle reinforcements [129,130], and phase transformation reinforcing techniques [128, 131]. Even though mechanical properties, particularly fracture toughness achieved by some of these conventional methods are not as high as in the case of laminated ceramics, they are worth mentioning as a part of the process of development over the years.

2.7 : Fracture in Materials

The historical world events such as Boston molasses floods due to tank failure, the liberty ships, destruction of space shuttle Columbia etcetera represents excellent walkthrough on the development of fracture mechanics. Fracture mechanics peaked after the world war II and saw its prime growth period from 1960 to 1980. Since 1960, the fundamentals of linear elastic fracture mechanics (LEFM) were well established, and researchers had started to learn more about crack-tip plasticity. Several fracture theories were developed by different researchers. For example, Wells [141] tried to apply LEFM to low- and medium-strength structural steel and found that, those materials were too ductile to apply LEFM techniques and led him to observe that crack separation happened with plastic deformation, and new parameter was developed to capture this effect which is now known as crack tip opening displacement (CTOD) technique. In 1968, Rice introduced the concept of j-integral which was basically a line integral expressing nonlinear energy release rate for plastic deformations at the crack tip [142]. At the same time, Hutchinson [143] and Rice and Rosengren [144] related j-integral to crack-tip stress fields in nonlinear materials and demonstrated that j-integral could be considered as non-linear stress-intensity parameter and as energy release rate. To successfully apply fracture mechanics concept into materials and design one must develop a mathematical relationship between toughness, stress and flaw size. Shih and Hutchinson first provided a relationship for fracture design analysis based on J integral. The contribution of Shih is remarkable in many fracture mechanics applications, who also demonstrated the relationship between J integral and CTOD and reported that both parameters were equally valid for fracture characterization.

One can see from the figure 2-26 that, the conventional strength of material approach compares anticipated design stress with the flow properties of the material and

the material is considered safe if its strength is greater than the applied stress. But fracture mechanics approach considers three important variables such as flaw size, fracture toughness which replaces the strength in the case of conventional strength of materials approach and the relevant materials property.

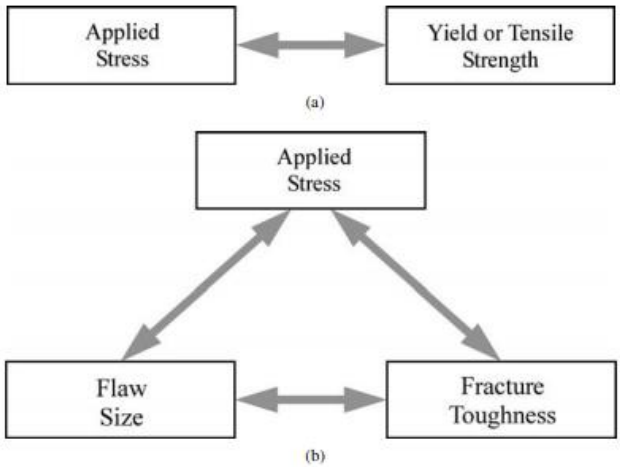

Figure 2-26: Comparison between (a) conventional strength of materials approach and, (b) Fracture mechanics approach [145]

Even after such intense research in the field of fracture mechanics, the behavior of the materials at micro and nano level are still obscure, and plenty of research is being done to develop a microstructural model for fracture and models to relate local and global fracture behavior of materials. Efforts are also being made to understand and characterize geometry dependent fracture in materials as traditional so-called single parameter fracture mechanics breaks down when it comes to linking local fracture phenomenon to global failure. Also crack propagation under mixed mode loading is yet to understand fully to couple the nanoscale fracture to total material failure. Molecular dynamics has the capability to provide a great insight of fracture phenomena at nano levels, and advancements in computational technologies have helped to the great extent to make

computationally exhaustive problems of simulating systems as big as containing million atoms. The present study is an effort to understand crack propagation under mixed mode loading at atomistic level of materials. Upcoming subsections discusses different fracture mechanics theories to predict mixed mode fracture in materials.

In the field of fracture mechanics, the main interest lies in knowing that (1) in which direction the crack is propagating and (2) under what specific circumstances. It is well known that for the fracture in the case of mode-I loading conditions, the crack continues to propagate in the direction in which it was initially oriented. For such fracture, Irwin's stress intensity factor K_I or Energy release rate (G_I) by Griffith's criterion are well known for prediction of fracture conditions. But that is not the case with the mixed mode fracture, in other words, due to introduction of mode-II loading (or any different loading that mode-I) the crack growth does not take place in its original direction and K_{II} (other loading modes) significantly affects the crack propagation, which serves as a motivation to develop an appropriate fracture which can predict mixed mode crack propagation.

There are two main approaches found in the field of mixed mode fracture analysis as in the case of the mode I fracture. One of them is energy approach, which is mathematically more rigorous than other one, and it considers detailed analysis of energy release rate of branched crack. Once the small branch of the main crack is obtained, its tip is used to determine the energy release rate along that direction. The energy released by the branched crack is maximized and it determines the crack propagation direction. Another approach uses near-tip stress field around a crack. In this criterion number researchers have developed phenomenological models which are based on stress intensity factors at the tip of the main crack which can be further used to describe the stress field near the crack. The merits of second approach is that with experimental calibration, phenomenological models based on stress intensity factors at the main crack tip can be

used in the stress field approach. One can easily avoid the complicated analysis required by branched cracks by using these already derived solutions for stress intensity factors to predict the crack growth directions.

There are many criteria to predict this kind of mixed mode fracture. Some of them are well-known, such as elliptical model, Maximum tensile stress criterion, Strain-energy-density criterion and Maximum energy release rate criterion, which are discussed below.

2.7.1 Simple Elliptical Model

As one knows, fracture criterion for mode-I fracture is given by,

$$K_I = K_{IC} \tag{2.6.1}$$

or similarly in energy approach as,

$$GI = G_{IC} \tag{2.6.2}$$

But to include mixed mode of fracture (i.e. mode-I and mode-II), one can extend (2.6.1) into,

$$F_{12}(K_I, K_{II}) = 0 \tag{2.6.3}$$

Where, F_{12} is a function of mode-I and mode-II stress intensity factors respectively K_I and K_{II} and some material constants. Now such function can be rewritten in the form of total energy release rate and one gave the relation as,

$$G = \frac{k+1}{8\mu}\,(K_I^2 + K_{II}^2) \tag{2.6.4}$$

And the crack will propagate when $G = G_C$, where G_C is the critical energy release rate. Thus, equation 2.6.4 can be re-written as,

$$\left(\frac{K_I}{K_C}\right)^2 + \left(\frac{K_{II}}{K_C}\right)^2 = 1 \tag{2.6.5}$$

Where, $K_C = \sqrt{\frac{8\mu G_c}{(k+1)}}$

One can see that; the above equation 2.6.5 is nothing but a circle having radius K_c presented in plane defined by $K_I \& K_{II}$. But here, given equation represents a special case, where $K_{IC} = K_{IIC} = K_C$ and K_{IIC} is the critical value of K_{II} and in general, is related to K_{IC}. But in reality, K_I and K_{II} do not follow circular trajectory at the point of failure and K_{IC} and K_{IIC} are not equal. Equation 2.6.5 would have been justified if we were to talk about crack growth in its original direction only, which is not a mixed mode fracture and growth of crack observed under mixed mode loading is not generally in the original direction as crack orientation. One can use following equation to account for this disparity.

$$\left(\frac{K_I}{K_{IC}}\right)^2 + \left(\frac{K_{II}}{K_{IIC}}\right)^2 = 1 \qquad (2.6.6)$$

One can observe from this equation that now the equation represents an ellipse in plane defined by $K_I \& K_{II}$. Where, K_{IC} and K_{IIC} is the fracture toughness for Mode-I and Mode-II fracture respectively, and K_{IIC} is generally determined by fitting equation 2.6.6 with the experimental data. This criterion does not discuss about crack growth direction. There are many ways to induce mixed mode fracture, in-fact most of the loading in real-life scenario is mixed mode loadings. One of the ways to perform mixed mode fracture is using a tension panel having a crack oriented at some angle as shown in the figure 2-27 (a). To make the tension panel behave as an infinite panel, the crack length is kept very small compared to in-plane panel size, so that the panel can be treated as an infinite one. Hoskin et al. [135] and Pook et al. [134] chose aluminum alloy sheets as specimens and performed mixed mode fracture analysis. They found the results to be similar to those obtained by equation 2.6.6 as shown in Figure 2-27 (b). Curves represents the solution obtained from equation 2.6.6 and data points are obtained by Hoskin and Pook experimentally on Aluminum sheet.

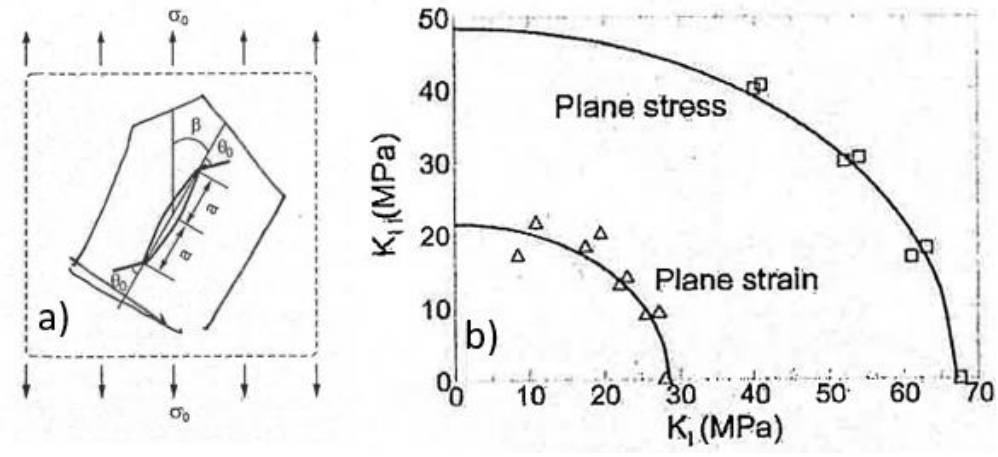

Figure 2-27: (a) An oblique crack in tension panel having much larger in-plane size compared to crack (b) Experimental data of aluminum sheets observed for crack initiation and theoretical curves from equation 2.6.6 [134,135]

As one can see, both plane-stress and plane-strain condition was considered. DTD 5050 aluminum alloy was loaded in plane strain condition, and K_{IC} = 28.5 MPa.$\sqrt{m}$ and K_{IIC} = 21.5 MPa.$\sqrt{m}$ was used for equation 2.6.6. Aluminum alloy of grade 2024-T3 was used for experiments whereas the critical values required by the criterion to obtain theoretical solution were 67 and 48.5 MPa.$\sqrt{m}$ for K_{IC} and K_{IIC} respectively.

2.7.2 Maximum Tensile Stress Criterion

Maximum Tensile Stress criterion for mixed mode fracture was first coined by Erdogan and Sih [136]. The criterion postulates (1) at the crack tip where the circumferential stress ($\sigma_{\theta\theta}$) becomes maximum with respect to θ the crack will extend in that direction, and (2) once $(\sigma_{\theta\theta})_{max}$ is reached to the value of stress responsible for Mode-I fracture the fracture will happen.

As one knows, the stress field around the crack-tip region is given by,

$$\sigma_{xx} = \frac{K_I}{\sqrt{2\pi r}}\cos\frac{1}{2}\theta\left[1-\sin\frac{1}{2}\theta\sin\frac{3}{2}\theta\right] - \frac{K_{II}}{\sqrt{2\pi r}}\sin\frac{1}{2}\theta\left[2+\cos\frac{1}{2}\theta\cos\frac{3}{2}\theta\right]$$

$$\sigma_{yy} = \frac{K_I}{\sqrt{2\pi r}}\cos\frac{1}{2}\theta\left[1+\sin\frac{1}{2}\theta\sin\frac{3}{2}\theta\right] + \frac{K_{II}}{\sqrt{2\pi r}}\sin\frac{1}{2}\theta\cos\frac{1}{2}\theta\cos\frac{3}{2}\theta$$

$$\sigma_{xy} = \frac{K_I}{\sqrt{2\pi r}}\sin\frac{1}{2}\theta\cos\frac{1}{2}\theta\cos\frac{3}{2}\theta + \frac{K_{II}}{\sqrt{2\pi r}}\cos\frac{1}{2}\theta\left[1-\sin\frac{1}{2}\theta\sin\frac{3}{2}\theta\right]$$

(2.6.7)

And, as figure 2-28 demonstrates the crack tip, the tip corresponds to origin of the polar coordinates (r) and (θ) and as known, its transformation with respect to cartesian stress tensor can be given by,

$$\begin{Bmatrix}\sigma_{xx}\\ \sigma_{yy}\\ \sigma_{xy}\end{Bmatrix} = \begin{bmatrix}\cos^2\theta & \sin^2\theta & -\sin 2\theta\\ \sin^2\theta & \cos^2\theta & \sin 2\theta\\ \frac{1}{2}\sin 2\theta & -\frac{1}{2}\sin 2\theta & \cos 2\theta\end{bmatrix}\begin{Bmatrix}\sigma_{rr}\\ \sigma_{\theta\theta}\\ \sigma_{r\theta}\end{Bmatrix}$$

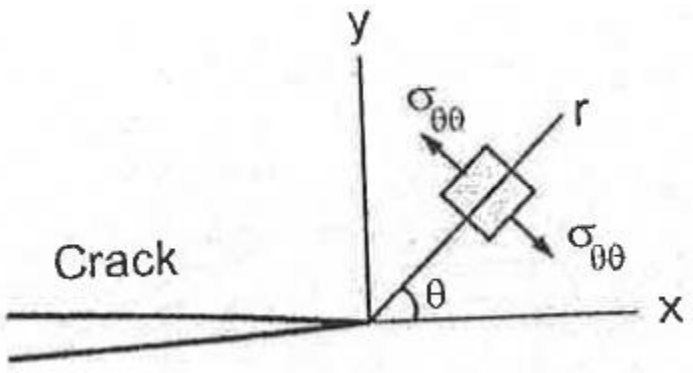

Figure 2-28: Coordinate system at the crack tip and the circumferential stress $\sigma_{\theta\theta}$

And hence, stress field near crack tip in polar coordinates can be obtained as,

$$\sigma_{rr} = \frac{K_I}{\sqrt{2\pi r}}\left[\frac{5}{4}\cos\frac{1}{2}\theta - \frac{1}{4}\cos\frac{3}{2}\theta\right] + \frac{K_{II}}{\sqrt{2\pi r}}\left[-\frac{5}{4}\sin\frac{1}{2}\theta + \frac{3}{4}\sin\frac{3}{2}\theta\right]$$

$$\sigma_{\theta\theta} = \frac{K_I}{\sqrt{2\pi r}}\left[\frac{3}{4}\cos\frac{1}{2}\theta + \frac{1}{4}\cos\frac{3}{2}\theta\right] + \frac{K_{II}}{\sqrt{2\pi r}}\left[-\frac{3}{4}\sin\frac{1}{2}\theta - \frac{3}{4}\sin\frac{3}{2}\theta\right]$$

$$\sigma_{r\theta} = \frac{K_I}{\sqrt{2\pi r}}\left[\frac{1}{4}\sin\frac{1}{2}\theta + \frac{1}{4}\sin\frac{3}{2}\theta\right] + \frac{K_{II}}{\sqrt{2\pi r}}\left[\frac{1}{4}\cos\frac{1}{2}\theta + \frac{3}{4}\cos\frac{3}{2}\theta\right]$$

(2.6.8)

Further, trigonometric function simplifications lead to,

$$\sigma_{\theta\theta} = \frac{1}{\sqrt{2\pi r}}\cos\frac{\theta}{2}\left[K_I\cos^2\frac{\theta}{2} - \frac{3}{2}K_{II}\sin\theta\right]$$

$$\sigma_{r\theta} = \frac{1}{\sqrt{2\pi r}}\cos\frac{\theta}{2}\left[\frac{1}{2}K_I\sin\theta + \frac{1}{2}K_{II}(3\cos\theta - 1)\right]$$

(2.6.9)

Now, at $\theta = \theta_0$ it is known that, $\sigma_{r\theta} = 0$ and $\sigma_{\theta\theta}$ reaches maximum $\sigma_{\theta\theta\max}$. Hence, equation 2.6.9 gives,

$$\mathrm{Cos}\frac{\theta_0}{2}[K_I\sin\theta_0 + K_{II}(3\cos\theta_0 - 1)] = 0 \qquad (2.6.10)$$

Which means, either,

$$\cos\frac{\theta_0}{2} = 0$$

Or,

$$K_I\sin\theta_0 + K_{II}(3\cos\theta_0 - 1) = 0$$

(2.6.11)

Therefore, from equations 2.6.11, the solution from first equation yields $\theta_0 = \pm\pi$ and it represents $\sigma_{\theta\theta} = 0$ corresponding to the original crack surfaces. Hence, crack propagation angle will be governed by second equation. And as Erdogan and Sih postulated, the fracture occurs when, $(\sigma_{\theta\theta})_{\max}$ is equal to the stress that leads to Mode-I fracture, that is,

$$(\sigma_{\theta\theta})_{max} = \frac{K_{Ic}}{\sqrt{2\pi r}}$$

Substituting, this condition into first equation of 2.6.9 (at $\theta = \theta_0$) yields fracture criterion satisfied by K_I and K_{II},

$$K_I \cos^2\frac{\theta_0}{2} - \frac{3}{2}K_{II}\sin\theta_0 = \frac{K_{Ic}}{\cos\frac{\theta_0}{2}}$$

(2.6.12)

Hence, Maximum stress criterion for specimen subjected to mixed mode loading can be described by equations 2.6.11 and 2.6.12. Critical stress intensity factor due to mode-I cracking (K_{Ic}) is the only material property showing up in this failure criterion which is worth noticing. If we were to analyze only mode-I or mode-II fracture,

Then, for Mode-I fracture the crack extension direction from equation 2.6.11 will yield $\theta_0 = 0$ (i.e. the original crack direction), as mode-II stress intensity factor will be zero. And when it is Mode-II fracture taking $K_I = 0$ gives crack propagation direction as,

$$\theta_0 = \cos^{-1}\frac{1}{3} = -70.5°$$

2.7.3 Strain-energy-density Criterion

Mixed mode fracture criterion based on strain energy density concept was proposed by Sih [137]. Strain energy stored in cracked body element dV = dxdy having unit thickness can be given as,

$$dU = \left[\frac{1}{2\mu}\left(\frac{k+1}{8}\left(\sigma_{xx}^2 + \sigma_{yy}^2\right) - \frac{3-k}{4}\sigma_{xx}\sigma_{yy} + \sigma_{xy}^2\right)\right]dV$$

Where, for plane strain and plane stress condition $k = 3 - 4v$ and $k = (3-v)/(1+v)$ respectively. Substituting the stress field for mixed mode loading, as given in equation 2.6.7 at the crack tip into the above expression, the criterion becomes,

$$\frac{dU}{dV} = W = \frac{1}{r}(a_{11}K_I^2 + 2a_{12}K_IK_{II} + a_{22}K_{II}^2)$$

(2.6.13)

And the coefficient $a_{ij}(i,j = 1,2)$ are given by,

$$a_{11} = \frac{1}{16\mu\pi}[(k - \cos\theta)(1 + \cos\theta)]$$

$$a_{12} = \frac{1}{16\mu\pi}\sin\theta\,[2\cos\theta - (k - 1)]$$

$$a_{22} = \frac{1}{16\mu\pi}[(k + 1)(1 - \cos\theta) + (1 + \cos\theta)(3\cos\theta - 1)]$$

(2.6.14)

In strain-energy-density criterion the stress field intensity is given by strain-energy-density factor as given by Sih in 1974 owing to the presence of singularity at the region very close to the crack tip as given by equation 2.6.13. and the factor as function of 'θ' is given by,

$$S = a_{11}K_I^2 + 2a_{12}K_IK_{II} + a_{22}K_{II}^2$$

(2.6.15)

The strain-energy-density criterion mainly postulates (1) minimum strain energy density with respect to θ will determine the crack growth direction, and (2) when the minimum strain energy density factor 'S_{min}', will reach its critical value 'S_{cr}', the crack propagation will take place.

Hence, sufficient and necessary conditions for W to have the minimum value at $\theta = \theta_0$ are,

$$\frac{\partial S}{\partial \theta} = 0 \;\; at\; \theta = \theta_0$$

(2.6.16)

$$\frac{\partial^2 S}{\partial \theta^2} > 0\; at\; \theta = \theta_0$$

(2.6.17)

Equation 2.6.16 and 2.6.17 helps us find crack propagation angle θ_0, and the fracture will then take place if,

$$S(\theta_0) = S_{cr}$$

(2.6.18)

Now if we were to study again only mode-I or mode-II fracture by applying the strain energy density criterion and subjecting an infinite panel to remote tension and shear respectively, we will get, For the Mode-I problem as shown in Figure 2-29(a),

$$K_I = \sigma_0\sqrt{\pi a} \quad and \quad K_{II} = 0$$

And,

$$S = \frac{{\sigma_0}^2 a}{16\mu}(k - \cos\theta)(1 + \cos\theta)$$

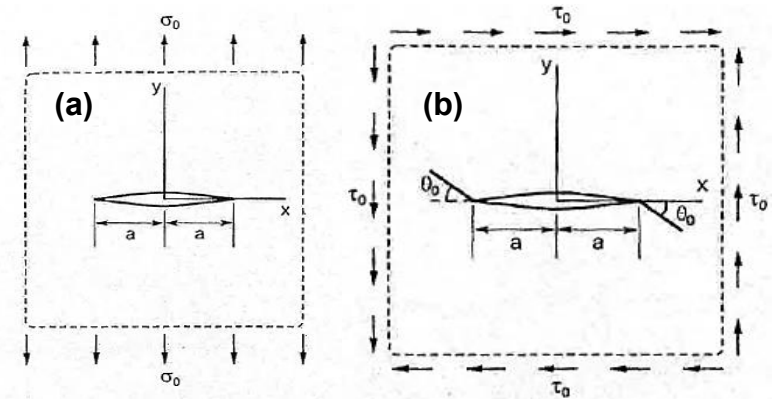

Figure 2-29: (a) Mode-I loading and crack initiation angle, $\theta = \theta_0$ (b) Mode-II loading and crack initiation, $\theta = \theta_0$

Then S will be minimum if,

$$\frac{\partial S}{\partial \theta} = 0, \quad \rightarrow \quad \sin\theta\,[2\cos\theta - (k-1)] = 0$$

Which yields two solutions, $\theta_0 = 0\ or\ \theta_0 = \cos^{-1}\frac{k-1}{2}$. But as,

$$\frac{\partial^2 S}{\partial \theta^2} > 0 \text{ at } \theta_0 = 0$$

$$\frac{\partial^2 S}{\partial \theta^2} < 0\ at\ \theta_0 = \cos^{-1}\frac{k-1}{2}$$

S will hence take minimum value at $\theta_0 = 0$, and the crack propagation will occur in the original direction of crack orientation. And the $S_{\min}$ is given by,

$$S_{min} = \frac{(k-1){\sigma_0}^2 a}{8\mu} \; at \; \theta_0 = 0°$$

Therefore, from above result and as mentioned in second condition of failure criterion that crack will propagate once S_{min} reaches S_{cr}, σ_{cr} can be given as,

$$\sigma_{cr} = \left[\frac{8\mu S_{cr}}{(k-1)a}\right]^{\frac{1}{2}}$$

Hence, the critical value S_{cr} can be represented in the form of fracture toughness K_{Ic} while keeping, $k = 3 - 4v$ for plane strain as,

$${K_{Ic}}^2 = \left(\sigma_{cr}\sqrt{\pi a}\right)^2 = \left[\frac{4\mu\pi}{1-2v}\right] S_{cr}$$

Hence,

$$S_{cr} = \frac{1-2v}{4\mu\pi}{K_{Ic}}^2$$

And, similarly for structure subjected to only mode-II loading, as shown in Figure 2-29(b),

$$K_{II} = \tau_0\sqrt{\pi a} \quad and \quad K_I = 0$$

$$S = \frac{{\tau_0}^2 a}{16\mu}[(k+1)(1-\cos\theta) + (1+\cos\theta)(3\cos\theta - 1)]$$

And for S to take the minimum value, it should satisfy,

$$\frac{\partial S}{\partial \theta} = 0, \quad \rightarrow \quad \sin\theta\,[(k-1) - 6\cos\theta] = 0$$

Which gives two solutions,

$$\theta_0 = 0 \; or,$$

$$\theta_0 = \mp \cos^{-1}\frac{k-1}{6}$$

Hence, $\theta_0 = 0$ gives S_{max} and the solution from second equation will give S_{min}. And the crack extension angle from the fact that $\sigma_{\theta\theta}$ is negative can be given by,

$$\theta_0 = -\cos^{-1}\frac{k-1}{6}$$

(2.6.19)

And the corresponding S is,

$$S_{min} = \frac{(14k - 1 - k^2){\tau_0}^2 a}{192\mu}$$

Since, $k = 3 - 4v$, it is conspicuous that growth of crack in a particular direction is affected by material's Poisson's ratio (v). If one obtains θ_0 values for different Poisson's ratio, it is noticed that under plane strain condition, solution obtained by maximum tensile stress criterion matches with the value obtained by Strain-energy-density criterion under Poisson's ratio = 0.

2.7.4 Maximum Energy Release Rate Criterion

This is a mathematically exhaustive criterion which requires a laborious analysis of rate of released energy under mixed mode fracture. It is basically an extension to Griffith's fracture theory. As a fracture condition, the criterion uses potential energy and determines crack propagation direction by maximizing the potential energy release rate. The criterion considers a small branch separated from the original crack tip, as shown in Figure 2-30, where α is denoted as a kink angle. if k_I& k_{II} are the local stress intensity factors at the kinked crack tip then one can represent the energy release rate at the kink tip as,

$$G_{kink} = \frac{k+1}{8\mu}\left({k_I}^2 + {k_{II}}^2\right)$$

(2.6.20)

One can see that, k_I and k_{II} here are functions of the kink angle α. A kink having length much lesser than the K-dominance zone is selected around the main crack tip to analyze the crack propagation direction. Having consider these, k_I and k_{II} can be expressed in

terms of K_I and K_{II} (stress intensity factors associated with main crack tip) and the kink angle α as,

$$k_I = C_{11}(\alpha)K_I + C_{12}(\alpha)K_{II}$$

$$k_{II} = C_{21}(\alpha)K_I + C_{22}(\alpha)K_{II} \tag{2.6.21}$$

Figure 2-30 shows a problem with a kinked crack and the functions listed in equation 2.6.21 needs to be evaluated for its analysis. Hussain et al. [138] reported expressions for $C_{ij}(\alpha)$ as given in equation 2.6.22.

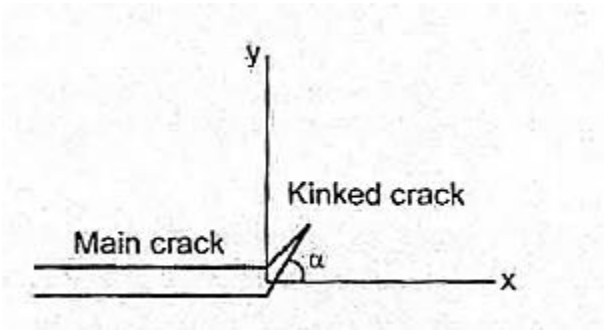

Figure 2-30: Kinked crack in mixed mode fracture

$$\begin{pmatrix} C_{11} & C_{12} \\ C_{21} & C_{22} \end{pmatrix} = \left(\frac{\pi-\alpha}{\pi+\alpha}\right)^{\alpha/2\pi} \left(\frac{4}{3+\cos^2\alpha}\right) \begin{pmatrix} \cos\alpha & \frac{3}{2}\sin\alpha \\ -\frac{1}{2}\sin\alpha & \cos\alpha \end{pmatrix} \tag{2.6.22}$$

Many other researchers such as Cotterell and Rice [139] and Lo [140], studied the kinked crack problem. Lo, obtained different expressions than Hussain and are presented below,

$$C_{11} = \frac{1}{4}\left(3\cos\frac{\alpha}{2} + \cos\frac{3\alpha}{2}\right)$$

$$C_{12} = -\frac{3}{4}\left(\sin\frac{\alpha}{2} + \sin\frac{3\alpha}{2}\right)$$

$$C_{21} = \frac{1}{4}\left(\sin\frac{\alpha}{2} + \sin\frac{3\alpha}{2}\right)$$

$$C_{22} = \frac{1}{4}\left(\cos\frac{\alpha}{2} + \cos\frac{3\alpha}{2}\right)$$

(2.6.23)

Lo et al. showed that above equations were valid for α up to 40º.

Substituting equation 2.6.21 into 2.6.20 one comes up with,

$$G_{kink} = \frac{k+1}{8\mu}[(C_{11}^2 + C_{21}^2)K_I^2 + (C_{12}^2 + C_{22}^2)K_{II}^2 + 2(C_{11}C_{12} + C_{21}C_{22})K_I K_{II}]$$

(2.6.24)

As we know, the crack will grow when strain-energy release rate is maximum. Hence, crack growth angle α_0, is determined by maximizing equation 2.6.24. Thus,

$$G_{kink}(\alpha_0) = \max_{-\pi \le \alpha \le \pi}\{G_{kink}(\alpha)\}$$

(2.6.25)

Crack growth direction of kink obtained by equation 2.6.25 gives the confirmation that strain energy near the crack tip in that direction becomes critical and crack propagates under local mode-I condition. Hence, according to maximum energy release rate criterion once can represent condition for crack to extend as,

$$G_{kink}(\alpha_0) = G_{Ic}$$

(2.6.26)

And, substituting 2.6.24 into 2.6.26 will give,

$$(C_{11}^2 + C_{21}^2)K_I^2 \; + \; (C_{12}^2 + C_{22}^2)K_{II}^2 + 2(C_{11}C_{12} + C_{21}C_{22})K_I K_{II} = \frac{8\mu}{k+1}G_{Ic}$$

(2.6.27)

One notices that, once where energy release rate reaches maximum, k_{II} will vanish and the equation 2.6.26 can be given as,

$$k_I(\alpha_0) = C_{11}(\alpha_0)K_I + C_{12}(\alpha_0)K_{II} = K_{Ic}$$

(2.6.28)

Equation 2.6.28 is also known as Local Symmetry Criterion (LS-Criterion), and fracture angle α_0 is determined by,

$$k_{II}(\alpha_0) = C_{21}(\alpha_0)K_I + C_{22}(\alpha_0)K_{II} = 0$$

(2.6.29)

It is noted that the fracture angles obtained from equation 2.6.25 and 2.6.29 using expressions given in 2.6.23 are almost identical, whereas the angles obtained using expressions in 2.6.22 deviates from each other when the Mode-II fracture becomes dominant.

Number of experiments have been done to assess the crack growth under mixed mode loading. One of such preliminary experiment was executed by Erdogan and Sih [136]. They used plexiglass sheets comprising an oblique crack subjected to tensile loading to induce mixed mode fracture as shown in Figure 2-27(a). The specimen sizes were 9" wide and 18" long with thickness of 3/16". The initial crack length introduced into the specimen was 2" long. Different crack orientation angles were selected to assess the behavior of crack growth. The orientation angles were measured from the direction of applied tension and were represented as β ranging from 30º to 80º. $(\theta_0)_L$ and $(\theta_0)_R$ corresponding to initial fracture angle at right and left ends of crack were measured and corresponding average value was obtained and are listed under $(\theta_0)_{avg}$ in Table 2-7-1. Along with these experiments, researchers also performed theoretical crack propagation analysis for similar models by maximum stress criterion, the strain energy density criterion, the maximum energy release rate criterion and the local symmetry criterion. One can see from the table that, all theories were able to predict the crack propagation angle with good accuracy to experimental values except for LS criterion predictions using C_{ij} expressions

given by Hussain et al. Crack propagation angle obtained by MS-criterion and ME-criterion with C_{ij} expressions of Cotterell and Rice [139] are quite close to the experimental values.

Table 2-7-1: Measured and Predicted Values of the Fracture Angle

β		30º	40º	50º	60º	70º	80º
$(\theta_0)_L$	1	-64º	-55.5º	-50º	-40º	-29º	-17º
	2	-60º	-52º	-50º	-43.5º	-30.5º	-18º
	3	-63º	-57º	-53º	-44.5º	-	-15.5º
	4	-	-57º	-52º	-43.5º	-	-
$(\theta_0)_R$	1	-65º	-58º	-50.5º	-44º	-31.5º	-18.5º
	2	-	-53º	-52º	-40º	-31º	-17.5º
	3	-60º	-55º	-51.5º	-46º	-31.5º	-17º
	4	-	-57º	-50º	-43º	-	-
$(\theta_0)_{avg}$		-62.4º	-55.6º	-51.1º	-43.1º	-30.7º	-17.3º
MS-Criterion		-60.2º	-55.7º	-50.2º	-43.2º	-33.2º	-19.3º
S-Criterion		-63.5º	-56.7º	-49.5º	-41.5º	-31.8º	-18.5º
ME-Criterion [139]		-60º	-55.6º	-50.3º	-43.2º	-33.3º	-18.9º
ME-Criterion [138]		-64.6º	-60º	-54.3º	-46.6º	-36º	-20.6º
LS-Criterion [139]		-60º	-55.6º	-50.3º	-43.2º	-33.3º	-18.9º
LS-Criterion [138]		-73.9º	-67.2º	-59.2º	-49.1º	-36.1º	-19.4º

Similar work has been done in the current work, the crack propagation angle in three different materials Al, SiC and ZrB_2 for initial crack orientation angle from 30º to 80º has been predicted using Maximum Energy release rate criterion. The predicted values are then compared with the crack propagation angle obtained from Molecular Dynamics simulations. The importance and capability of Molecular Dynamics to serve as an alternative to experiments, detailed methodology and results are explained in upcoming sections of this work.

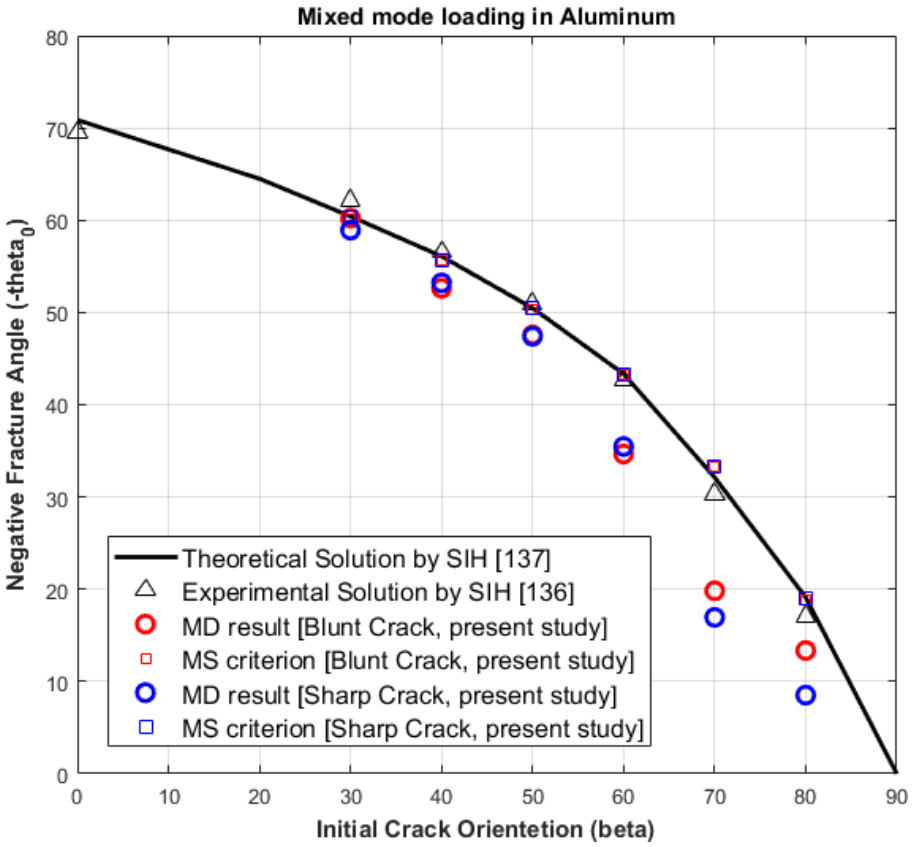

Figure 2-31: Results obtained for crack propagation under mixed mode loading in Aluminum

2.8 : Computational material modeling and simulations using molecular dynamics

Having discussed the processing techniques and mechanical strength improvement in ZrB_2 based ceramics, it is important to discuss the tools and technologies that have to enable us to tailor the materials from Nano-scale as per our requirements over the past three decades or so. For example, high-resolution electron microscopes have enabled the visualization to the scale as small as an atom, and to add, the scanning probe techniques led us to manipulation of those individual atoms. Technology to tailor-design systems from as small as molecules to as large as the fuselage of a plane has become possible owing to the synthesis of advanced materials. It has been possible to develop protective coatings more wear-resistant compared to diamond owing to exploitation of the material properties at the nanoscale. Also, fabrication of alloys and composites which are stronger than ever has become possible because of nano-engineering. A different regime where nanoscale materials have potential application is material reinforcements, field emission panel display, chemical sensing, drug delivery, nanoelectronics and tailor-designed materials. Coupled continuum-molecular-quantum mechanics has shown great promises to model microscale phenomenon which can explain macroscopic behavior of the materials and this is facilitated by advanced computational tools and enhanced experimental tools efficient enough which can synthesize systems at the nano-scale. The following section is dedicated to the discussion of current nanoscale engineering horizons and importance of multi-scale modeling.

2.8.1 Nanoscale Engineering and Multi-Scale Modeling

Contribution of mechanics' principles have contributed immensely in development of nanoengineering. Liu et al. [147] divided the major application of nanoengineering in research into three major fields, namely cell mechanics and neurobiology,

microelectromechanical systems (MEMS), Protective coatings (i.e., nanoceramics) and energy-absorbing polymer-based nanomaterials.

Cell mechanics principles are being applied to understand neurobiology and cancer research. Some of the limitations in the field is the understanding of different cell structure, interactions and adhesive forces, which when understood will lead to the development of novel treatment methodologies for cancer. Application of DNA into nanotechnology and biotechnology has enabled researchers to design and produce materials from the atomic scale. Research so far have led us to understand about how DNA strand reacts with each other, and this information is being used to design solid material purely by manipulating its properties by changing underlying DNA strands as a basic building block.

Nanotechnology has also been proven a boon for developing nanoscale sensors which are highly mobile and capable of detecting illegal and harmful chemical substances which are airborne during unlikely events like chemical attacks. Other than this, energy-absorbing polymer-based nanomaterials are being developed to provide a stronger material with lightweight which can provide ballistic protection to army personnel.

Protective coating and materials tailoring is another great areas being benefitted by nanotechnology. As discussed earlier with the help of scanning probe experimental techniques and molecular dynamics computational techniques, researchers have been able to explore unchartered territories of super-strong materials. The protective coating is one of such technology applicable to gear and bearings in automotive and aerospace industries and naval vessels for the military. The fundamental motivation is to design inherently stronger materials or to bring advancement in readily known hard materials. For example, nanoscale diamond ceramics in tribological applications as wear resistant

constituent. Certainly, such development will lead to the greatly reduced maintenance cost and increased material life.

As described earlier, microelectromechanical (MEMS) and nanoelectromechanical (NEMS) systems are also key development field being benefitted by nanoengineering. Development of magnetic materials which are only a few nanometers thick have significantly increased the capacity of a hard-drive to store the data. Apart from that Moore's law suggests twofold increment in computation power on and average every 18 months. Many of these advancements in processing capabilities are due to nanoengineered materials.

Along with nanotechnology, multiscale modeling has brought about vast changes in the field of molecular-scale mechanics and materials. For examples in solids, research in plasticity and damage has gained some success in advancing microscale component design. There are plenty of applications in which coupling of different physics is required. For example, in fluids, coupling physics phenomena at the nanoscale is crucial in designing components at the microscale. Similarly, electrophoresis and electro-osmotic flows coupled with particulate motion in a liquid is another example of coupled physics phenomena. Once the governing models based on multi-physics are developed for such phenomena, computational techniques are employed to solve such complexly coupled problems. The problem with continuum-based computational capabilities is, its incapability to capture the operative conditions of any physical phenomenon for wide range of system state. Non-continuum behavior is present and always observed in large deformation behavior of nanotubes, ion deposition processes, gas-dynamic transport, and material mechanics as characteristic scales drop toward the micron scale. Also, interactions between different physics like thermal effect and mechanical response of the material becomes increasingly important. Another need for Multi-scale modeling is because

nanoscale components will be used along with larger components that respond at different timescales. In such hybrid system, the interactions between different time and length scales may play a crucial role in the performance of the complete system.

Multi-scale techniques for the most part suggest usage of data at one length scale to hence show the reaction of the material at bigger length scales, which can be additionally isolated into two classifications as hierarchical and concurrent as specified by Liu et al. The hierarchical multi-scale techniques straightforwardly utilize the data obtained at the lower scale length as a contribution for the substantial model with the assistance of averaging process. For example, such techniques use averaging methods to homogenize the effect of defects generally found at micro or nano level to describe material property like Young's modulus at macro level. On the other hand, concurrent multi-scale methods while executing a run, simultaneously obtain data at the lower lengths (i.e. Micro/nano scale) and input it into the macro models. Thus, evidently, as finite elemental methods have brought about great advancements in computer-aided engineering at the microscale, one may expect the multiscale analysis tools to enhance the nanoscale methods at hand by developing and validating the predictive multiscale models which can fit in material design into viable engineering process. Also, to model more realistic state of system, the developed multi-scale models should span over statistical distribution of defects and uncertainty.

Liu et al. also discussed some examples of material microstructure strengthening mechanisms at different length scales as shown in figure 2-32. As shown, there exists, number of complex distortion mechanisms prevailing at different material dimensions in a particular high-strength steel. One can see that the structural properties of the ship at macro scale is controlled by flaws present at various scales, secondary additives and the interactions among them and with matrix. Decohesion/debonding is primarily responsible

mechanism which controls fracture toughness and is facilitated by primary inclusions of TiN at micro level and the secondary inclusions such as TiC which have nanoscale structure, provides strength by resisting interfacial parting after the material is yielded. Thus, one can conclude that the property of the steel in the present case is due to different inclusions interacting at different length scales in different ways. Hence, developments so far have rendered hierarchical modelling of steel's mechanical response with the help of averaged properties obtained at atomic scales to predict the macroscopic behavior possible, but concurrent modelling of such phenomenon still seems hard to achieve which spans over atomistic to continuum scales along with important interactions described at sub-length scales (i.e. mesoscopic length scales). Thus, it is an immense challenge to design a material model which accurately defines interactions between atomic and continuum length-scales, and a lot of work is being done to produce efficient algorithms and computational techniques that can give out the useful information at different scales using lesser computational power progressively.

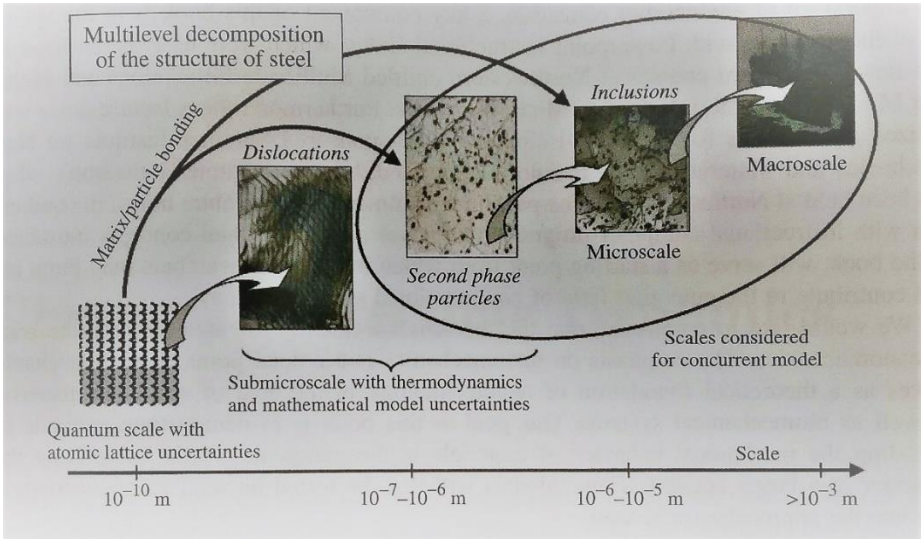

Figure 2-32: Multiscale properties of steel [147]

2.8.2 Applications of Molecular Dynamics (MD) Simulations

As mentioned earlier, in molecular dynamics Lagrangian or Newtonian equations are solved numerically for classical multi-particle systems. Once, time-dependent solutions are obtained one can also postprocess the data as per need using these codes.

Park and Zimmerman [148] performed tensile test on gold nanowires using MD simulations as shown in figure 2-33. The objective of the research was to investigate the yield and fracture properties of the nanowires. They presented via MD experiments using two different EAM (Embedded Atom Method [156]) potential that the accurate modeling of stacking fault and surface energies is critical in capturing the fundamental deformation mechanism in gold nanowires by MD simulations.

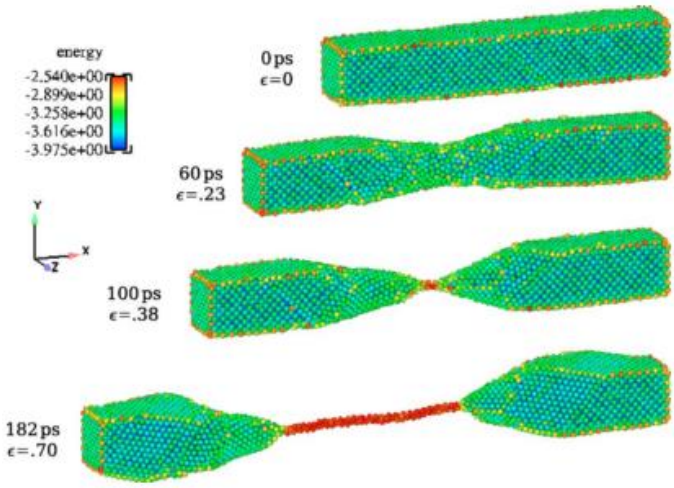

Figure 2-33: Tensile test of a Gold nanowire by molecular dynamics simulations using EAM potentials. [148]

As one can see from the simulation results in figure 2-33, failure phenomena such as necking and yielding which is generally found in macroscopic samples under tensile load is also presented by molecular dynamics. Apart from that MD results also depicted

extremely ductile behavior of gold nanowires by elongation of gold nanowires in extremely thin nanobridges, which are referenced as atom-thick chains (ATC) by Zimmerman, before the fracture of the nanowire. Initially, the wire was 16 nm long and had a square cross-section of 2.588x2.588 nm^2. Quasi-static relaxation of the wire having free boundaries was firstly performed to minimize energy configuration, followed by thermal relaxation while keeping the system's volume constant at 300K by Nosé-Hoover thermostat to finally load it at one of the free ends with strain rate of 3.82e-9 S^{-1} while keeping the other one fixed.

Another experimental setup that is commonly performed on MD simulations is nanoindentation. Researchers have analyzed materials properties of thin films and nanoscale materials by simulating atomic-scale indentation as an experimental technique. During the experiment, matrix/substrate material being studied is pressed with the help of diamond (i.e. a hard material) coated indenter. Then with the help of obtained tip properties and resultant load-defect curve, and also substrate's plastic response the property of the matrix material is obtained. When modelling such phenomenon with molecular dynamics simulations one must utilize Newton's equations to solve for position and velocities of N number of particles where velocity is obtained through force on each particle given by gradient of function determining the interatomic potential forces. Apart from nano-indentation, some of such phenomena which requires solving newton's equations of motion in MD simulations are crack propagation, tensile and shear deformation of single and polycrystalline materials etc. Again, in the case of nanoindentation experiments, this interatomic potential defines the interactions between the substrate atoms and the interaction from matrix atoms to indenter atoms and vice versa as well as between all the atoms of indenter. In most of the cases of such research, indenter atoms are generally applied with boundary conditions defining constant displacement all over the indenter domain along with the particles which can accommodate required indenter load rendering

required inter-atomic potentials to be defined only for substrate atoms. As far as no external force is applied, the atoms in solid substrate do not move freely as they are bound by the potential function to vibrate around the equilibrium conditions defined through local minima of that function. For solid domains this potential is such as the substrate atoms, in the absence of external force, cannot move freely in the domain and they are only able to vibrate near some equilibrium configuration determined by the local minima of an applied potential function. Once the system is equilibrated the configuration is used as the initial position of the atoms and the velocities which are generally obtained through Maxwell-Boltzmann distribution throughout the system, are considered as initial velocities comprised by each atom. One of the key observation generally made from such study is that how the substrate shows plastic deformation by beginning and progression of lattice dislocations. To reduce the computation time many researchers while using Lennard-Jones potential function, introduce parameter known as cut-off distance referencing to second or third near neighbors, beyond which atomic interactions are neglected.

Surface engineering, physical chemistry and mechanics of thin films have extremely benefitted by Molecular dynamics simulations. One of the many problems in this field is nano-deposition, which is basically computational modelling of substrate and vapor molecules being deposited on it. Here the solid substrate is modelled atomically surrounded by gaseous atoms interacting through a certain potential function. In some cases, if a particular orientation of deposited material is required along with a specific modulus of the incident velocity vector then external electromagnetic field is provided to achieve necessary directionality in deposited material with respect to the surface of substrate. This phenomenon is generally known as ion-beam deposition (i.e. physical/chemical vapor deposition process). J-Y Raty et al. [149] reported the result of ab

initio molecular dynamics simulations to help understand the early stages of CNT's growth on metal nanoparticles.

Apart from these, there is plenty of literature on the successful application of MD simulations of atomic-scale fracture mechanics which is greatly dynamic in nature. Sakib et al. [150] studied shear fracture in confined NaCl nanofilms with the help of Molecular Dynamic simulations and obtained several mechanical properties such as failure strain, stress, and stress intensity factors. The objective of the research was to assess the mode of crack propagation in two differently oriented single crystals of NaCl under shear loading. Consistent with the experiments initial kink was observed for any orientation and confinement of the nanofilms. Also, the mode of crack propagation was heavily depended upon crystal orientation, but one can see from the figure 2-34, that crack propagates into a zig-zag fashion, and it opened vertically first with critical angle always being 90°. Different values of crack-opening slope angle and mode-II stress intensity factor was observed for differently confined NaCl single crystal. The interatomic potentials used for the model comprised long-range columbic electrostatic interactions potential as well as short-range Buckingham potentials and core to core repulsive as well as attractive Van der Waals interactions. Simulations were carried out at 0.0005 ps time steps with a constant strain rate of 0.1/picosecond.

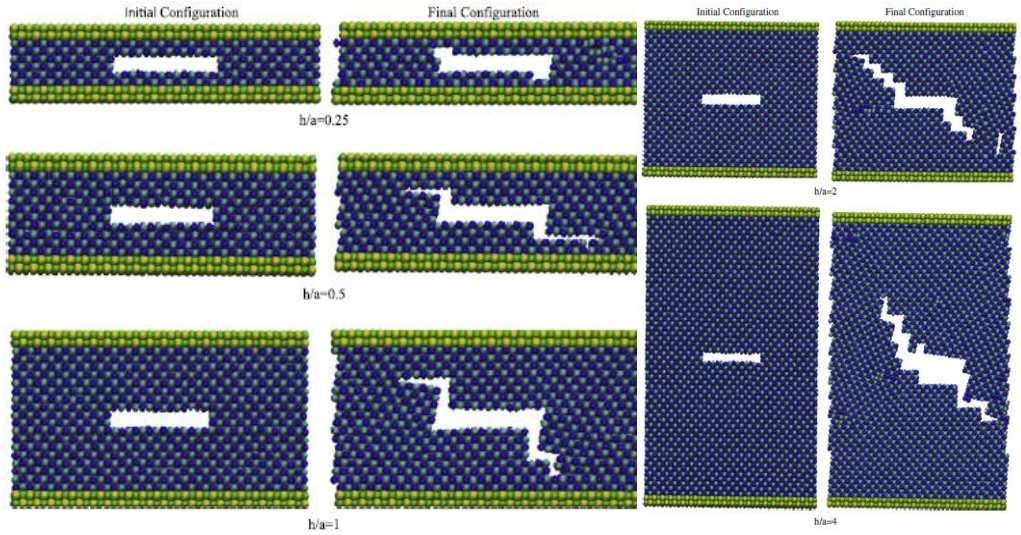

Figure 2-34: Before and after shear test snapshots of the single crystal NaCl Nanofilms with different confinement [150]

S. Ferdous and A. Adnan reported on tailoring fracture toughness of Silicon Carbide by nanoscale multilayering with diamond [151]. Multilayered ceramic was designed at atomic scale by altering layers of SiC and diamond, and the thickness of the nanodiamond film was varied between 2 nm to 10 nm. Center crack was initially generated into the SiC layer, and calculations for fracture toughness were made by integrated MD-FEM simulations. They concluded that, the fracture toughness of multilayered film can be varied by changing the SiC layer thickness and that, fracture toughness under mode-I fracture conditions can be increased by 20% by changing SiC layer thickness from 2nm to 5 nm. The MD simulation comprised a total of around 35,200 atoms with the interaction between Si-C, Si-Si, and C-C defined by tersoff potential [158, 159]. As one can see from the figure 2-35, crack was initially placed into the SiC layer. The system was relaxed using NPT ensemble for 10 picoseconds with step-size of 0.5 fs.

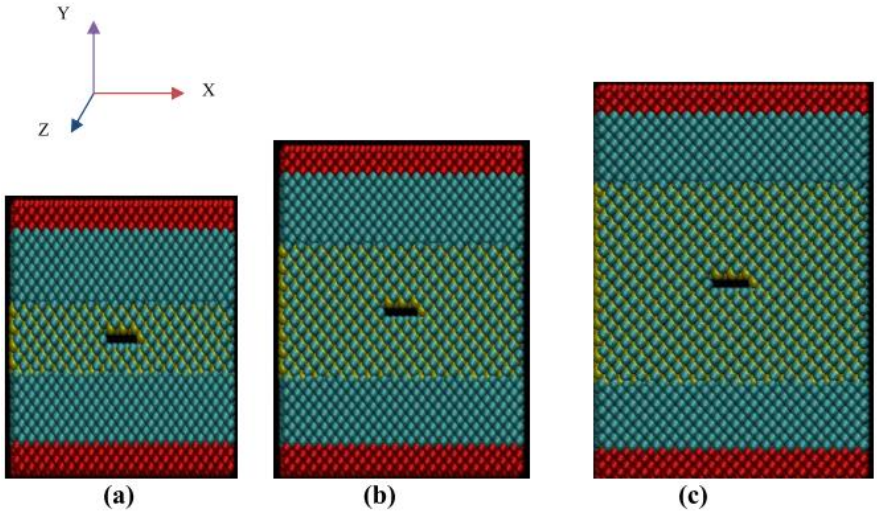

Figure 2-35: SiC/diamond nanoscale multilayered ceramic with center crack in SiC layer with varying layer thickness ratio of (a) SiC/ND = 1:1 (b) SiC/ND = 2:1 (c) SiC/ND = 3:1 [151]

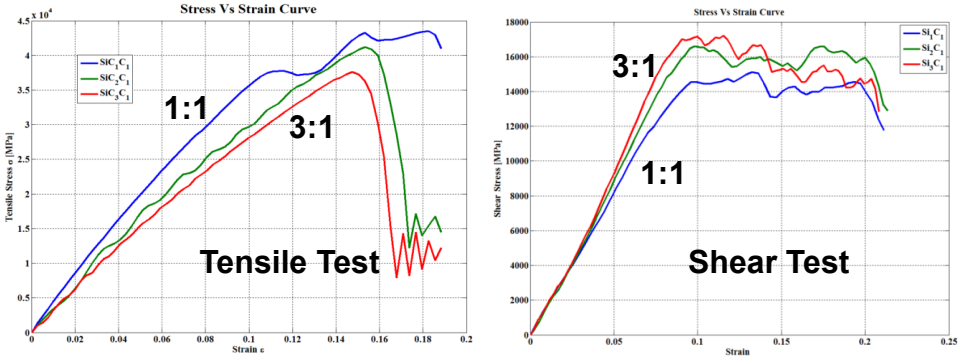

Figure 2-36: Stress-Strain curves after Tensile and Shear test of the three undertaken models [151]

The results clearly indicate that decreasing distance between crack position and nanodiamond increased mode-I fracture toughness but is not the case for mode-II fracture.

Effect of carbon enrichment in SiC single crystals was also studied by Adnan and Ferdous in a separate research [152]. MD simulations were performed to study the effect

of carbon enrichment by 10%, 20%, 30%, 40% and 50% in SiC on configuration energies, densities, coordination number and radial distribution functions and tensile as well as shear strength. From the free energy profiles obtained via MD simulations, they concluded that, for all the undertaken enrichment, configuration energy achieved minimum value and thus enabling the system to remain stable for long period of time. Also, the density of the system initially decreased by around 6% for carbon enrichment up to 20%, after which the density increased monotonically. Figure 2-37 shows a stress-strain curve for the tensile test. One can see that system became more brittle as the carbon enrichment increased, but optimum performance was reported for 20% and 30% enrichment considering both performances under tensile and shear loading [152].

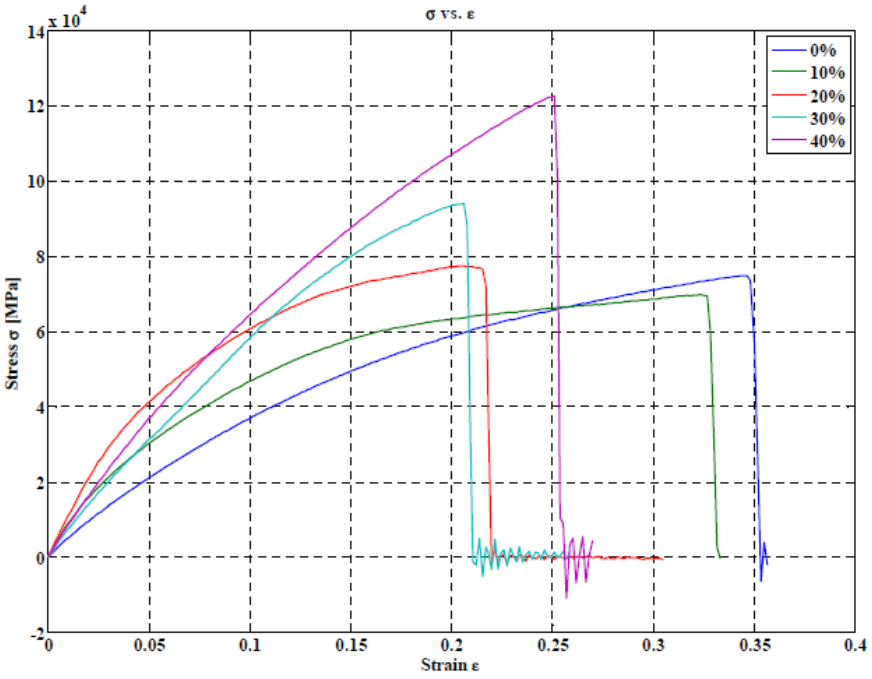

Figure 2-37: Stress-Strain curves from MD simulations for different enrichments [152]

Drawing on to the prediction of mode-I fracture toughness of diamond at nanoscale, Adnan and Ferdous reported the fracture process of nanoscale diamond using atomistic simulations and fracture toughness of the nanodiamond using Griffith's energy

release rate, crack-tip opening displacement method (CTOD), Irwin's K-based method and the modified crack closure method [153]. Three different models having crack length of 5, 7 and 9 times the lattice constant of diamond were selected for the study, and fracture toughness was obtained by only MD simulations in the case of Griffith's energy approach and CTOD method, whereas MD and FEM were employed to determine fracture toughness using Irwin's K-based method and modified crack closure method. While reporting the fracture toughness in terms of critical stress intensity factor (K_{IC}), authors found the obtained fracture toughness for nanodiamond consistent regardless of undertaken theory or crack length, which is evidenced from figure 2-38 given below. Authors closed the discussion with concluding very important phenomenon that, the continuum fracture-mechanics theories are well applicable at the nanoscale and MD simulations at atomic scale are efficient enough to capture the true mechanical behavior of the system.

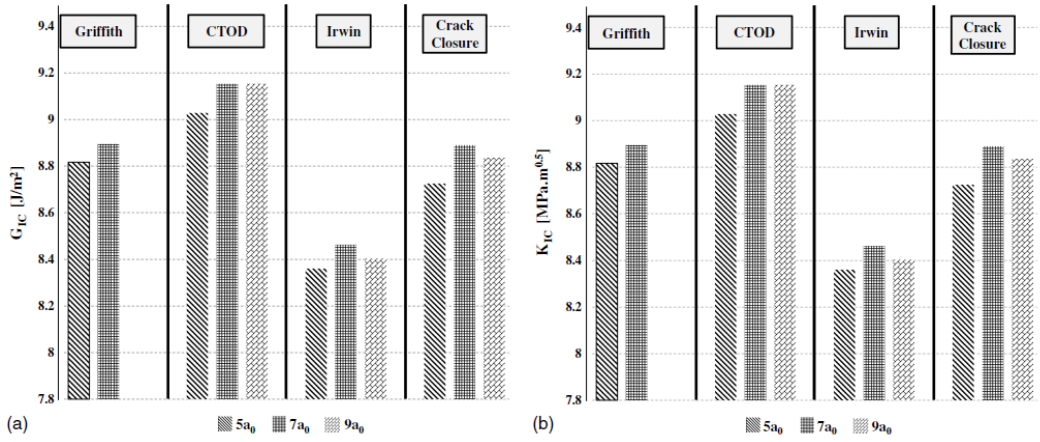

Figure 2-38: Predicted fracture toughness of nanoscale diamond using four different theories and MD simulations [153]

Shao-Huan Cheng and C. T. Sun reported on the effect of size on fracture toughness of nanoscale structures while demonstrating crack-strip approach in molecular dynamics [173]. Having considered the local virial stress, the authors overcame the barrier

of the ambiguous crack-tip stress field in molecular dynamics simulations and performed direct calculations of fracture toughness. The distinctive difference between this study and prior similar work was that their studies did not talk about the existence of inverse square root singular stress field at the atomic level. Hence crack-tip stresses were assessed via molecular dynamics simulations in the study. NaCl single crystals were adopted throughout the simulations. Authors successfully demonstrated that the opening stress distribution ahead of the crack tip could be matched for atomic-level simulations and corresponding continuum models. The MD calculated crack-tip opening stress was used to determine the fracture toughness by FEM model. The significant result was that, fracture toughness measured by stress intensity factor cannot be used as a material constant while the crack length is below 100Å, but once the size ok singular stress zone (i.e., K-dominance zone) is large such as in case of crack longer than 100Å, fracture toughness approaches the theoretical value of surface energy, making Griffith's approach valid. They also reported that the size-dependent behavior was the result of the continuum fracture mechanics that was developed based on continuum models which take singular stress field as stress intensity factor and in the cases where singular stresses are not dominant the two-parameter model presented in the study accounted for both singular and non-singular stress terms which predicted the failure load more accurately.

In the upcoming section, working methodology of current work will be presented. The study includes an atomistic model of the core-shell type of structure for ZrB_2-SiC nanoceramic and molecular dynamics simulations for prediction of crack propagation under mixed mode fracture conditions in different materials.

Chapter 3 Set-up and methodology

Having discussed different fracture mechanics theories for prediction of crack growth direction under mixed mode loading and strengthening mechanisms in ZrB_2-SiC based ceramics, the details are provided about the simulation environment, considered atomistic models and sequence of test methods in this section. As molecular dynamics simulations are used exclusively for all the work, firstly, the overall working methodology of molecular dynamics simulations is discussed along with the particular program used to carry out the simulations.

3.1 : Molecular Dynamics as a tool

As discussed in the earlier section, computer simulations act as a bridge between microscopic length scale and macroscopic material behaviors. With the provided initial positions and guesses interactions between the molecules, MD algorithm predicts the dynamic properties of the system over the time, and the accuracy of this prediction directly depends upon how well the physical model is prescribed via interacting potentials and available computational power. Should one consider computer simulations as theories or experiments will remain everlasting debate, as some believe that the MD simulations cannot be considered as experiments as no direct interaction with system is done like real experiments whereas others believe that for many times MD simulations (i.e., computer simulations) are used as an alternative to the experiment when creating the particular test environment is difficult in practical situation but probing the system behavior in such environment will give significant insights. Resolution to this dilemma can be presented as one should not take MD simulations as an alternative to experiments, in fact as mentioned by J. M. Haile in his excellent review on Molecular dynamics [154], simulations as elementary methods, MD simulation must be used to bridge the gap between theories and

real experiments. In other words, MD simulations can serve as an alternative to reductionism (method of presenting system close to the real system but with the help of reduced dependent components) and which might lead to a new way of presenting the science or it can serve as a method in reductionism. Figure 3-1 given below gives an idea about this latter part that the computer simulations can offer, simulation data on models which can be used to test the theories or the data that one can compare with the experimental behavior of a model to test the realism of simulated models. It is this fundamental on which current work is based on. MD simulations are performed to simulate crack propagation under mixed mode loading for various material models and mechanical properties obtained via these simulations are checked against available experimental work and theoretical solutions to check the capability of atomic model to pick up the real material behavior, which once recognized gives the confidence to use MD simulations to predict such dynamic responses of the materials.

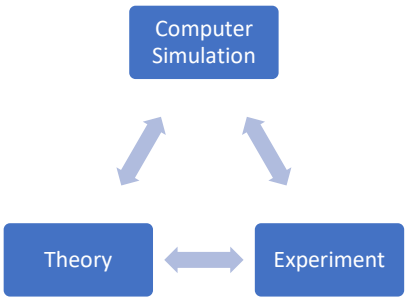

Figure 3-1: Interplay between Theory, Experiments and Computer Simulations [154]

The atomistic simulations in the present study were carried out with LAMMPS (Large-scale Atomic/Molecular Massively Parallel Simulator) [174]. Provided the appropriate force fields and boundary conditions, LAMMPS is able to model atomic, polymeric, biological, metallic, granular, and coarse-grained system. The capability of parallel computing through spatial decomposition is what makes LAMMPS significantly faster and better than most of the other open source MD codes.

3.2 : Atomic Interactions

There are two versions of MD simulations. One is classical MD, and another one is *ab initio* methods. Classical MD addresses the problem while considering atoms as classical entities (i.e., only position and momentum) whereas *ab initio* methods treat electronic and ionic degrees of freedom separately where electrons are represented as a wavefunction. The former approach of Classical MD is used throughout this work.

MD simulation process is carried out by a step-by-step solution of the classical equation of motion. Initial particle positions and some interatomic potential function is given as an input of an MD code. For any instance of time *t,* the particles can be represented by position vector in 3N dimensions as, $r^{3N}(t) \equiv \{r_1(t), r_2(t), \ldots, r_N(t)\}$, where vector r_I represents 3 coordinates of an atom *i*. One can say that system will have an initial condition having prescribed initial positions by $r^{3N}(t_0)$ and velocity by $\dot{r}^{3N}(t_0)$ at time $t = t_0$. As the simulation proceeds, position and velocity of particles are updated at every timestep and force on each particle is evaluated for the next iteration. A General working algorithm of an MD code presented by Li et al. [155], is given below in figure 3.2. During the whole process of MD code force evaluation is the most computationally expensive step. Also, this force on each atom is evaluated by the gradient of potential function *U*. Therefore it is the potential function, which determines the compromise between a physical representation of the system and computational efficiency. The classical equation of motion which is evaluated at every timestep is given in following equations.

$$m_i \ddot{r}_i = f_i \qquad f_i = \frac{\partial U_i(r^N)}{\partial r_i} \tag{3.2.1}$$

Where, m_i represents mass of an i^{th} atom; f_i represents force on i^{th} atom and as discussed earlier r_i is position vector of the same atom. Now, for any system comprising *N* number of particles, one should first come up with appropriate potential function which should be capable enough to capture the material behavior under study within sensible

computational time. Over the years number of researchers have presented several types of interatomic potential function to capture certain physical phenomenon.

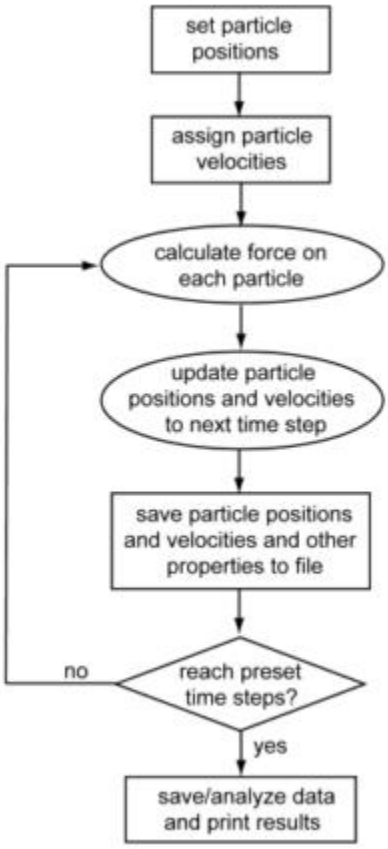

Figure 3-2: General Flowchart of an MD code [155]

As practically all atomistic simulations are based on Born-Oppenheimer adiabatic approximation which hypothesize that, electron motions can be treated differently from nuclear motions; as electron move much faster than nuclear owing to their smaller mass one can treat the nuclei as fixed for an instance of time and analyze for the position and velocity of electrons or equivalently electron wavefunction following the nuclear motion adiabatically, which results into consideration of electrons into their ground state while only position of nuclei changes. One can consider the expansion of such potential function *U* in

terms of one-body, two-body, three-body or n-body interactions as depicted in the following equation.

$$U(\mathrm{r}^{3N}) = \sum_{j=1}^{N} V_1(\mathrm{r}_j) + \sum_{i<j}^{N} V_2(\mathrm{r}_i, \mathrm{r}_j) + \sum_{i<j<k}^{N} V_2(\mathrm{r}_i, \mathrm{r}_j, \mathrm{r}_k) + \cdots \quad (3.2.2)$$

Unless any external force-field is applied to each atom, the first term of the equations is absent. Pairwise additives from two-body interactions generally contribute to the second term of the equations, and similarly, three-body interactions are presented by the third term into the equations. Many researchers have developed many-body potentials as to provide an improved description of the interatomic interactions, especially for most of the engineering materials with cubic crystal. During the whole study different interatomic potential functions were employed to model different materials and interface between two materials in the later part of the simulations. The work is done in two parts. The first part of the study includes fracture analysis of atomistic system under mixed mode loading and the second part includes computational designing of the novel material system, as so the fracture toughness of the compound can be increased.

3.2.1 Embedded-Atom Method potential function

Aluminum was used as a benchmarking material as both theoretical as well as experimental data is available on crack propagation under mixed mode loading. Hence, the first study was done on single crystal aluminum's atomic model to check the applicability of MD simulations for rest of the materials. Daw and Baskes developed a many-body semi-empirical model of metals and impurities known as Embedded Atom Method (EAM) [156] to describe a potential function for transition metals. EAM potential works perfectly well to assess fracture in transition metals such as Ni, Cu, Ag, Au, Pd, Pt etcetera. Later, EAM potential was developed for Al and Ni by Mishin et al. [157] based on the data obtained through experiments and a large set of energies of different alternative

crystalline structures of the material generated by *ab initio* calculations. In EAM method, the potential energy of an atom is generally given by the following equation.

$$U_i = \sum_i F(\bar{\rho}_i) + \frac{1}{2} \sum_{ij, j \neq i} \varphi(r_{ij})$$

$$\text{where, } \bar{\rho}_i = \sum_{j \neq i} \rho(r_{ij}) \qquad (3.2.3)$$

In the equation, $\varphi(r_{ij})$ is a pair potential as a function of the interatomic distance r_{ij} between atoms *i* and *j* within the cutoff distance, F is the embedding energy as a function of electron density which is further a function of atom positions at an instance. The factor 1/2 in the second term accounts for double counting the pairwise interactions. The simulation of crack propagation in aluminum was carried out with potential developed by Mishin et al.

3.2.2 Tersoff Potential function

Being convinced that a three-body potential is not adequate to accurately describe the cohesive energy of silicon over a wide range of bonding geometry and coordination, Tersoff abandoned the use of N-body form in its newly proposed potential function in 1988 [158]. Instead, he developed bond-order type potential which is extensively used to model many covalent systems. He argued that from simple quantum-mechanical arguments, the more neighbors an atom has, the weaker will be the bond to each neighbor and that the bond strength or bond-order depends on geometry in a complex way. He showed that how different type of bonds in the different material can lead to have different coordination number and depend upon local environment and hence, he hypothesized that, owing to the crucial role of bond-order and its dependence upon local geometry, one should include environment-dependent bond order into the potential. He firstly calibrated his potential

function for silicon (Si) and later for carbon (C). Following are the equations that describe simplest form of tersoff potentials.

$$E = \frac{1}{2}\sum_{i}\sum_{j\neq i} V_{ij}$$

$$V_{ij} = f_c(r_{ij})\left[a_{ij} f_R(r_{ij}) + b_{ij} f_A(r_{ij})\right] \tag{3.2.4}$$

Where E is the total energy of the system which ultimately depends upon site energy which further depends upon bond energy V_{ij}. Again, *i* and *j* runs over all the atoms of the system and r_{ij} is the distance between atom *i* and *j*. Term a_{ij} ends up having value equals to 1 as pair-interaction beyond first neighbor are generally not included into the potential function.

$$f_c(r) = \begin{cases} 1, & r < R - D \\ \frac{1}{2} - \frac{1}{2}\sin\left(\frac{\frac{\pi}{2}(r-R)}{D}\right), & R - D < r < R + D \\ 0, & r > R + D \end{cases} \tag{3.2.5}$$

f_c is a smooth cutoff function which limits the range of the potential so that force evaluation require much lesser computation power and still produce desired properties. Parameters R and D are not optimized but are chosen to include first-neighbor shell only for several selected high-symmetry bulk structures of silicon such as Si_2, graphite, diamond, simple cubic, and face-centered cubic structures. Hence, f_c decreases from 1 to 0 in the range, $R - D < r < R + D$.

$$f_R(r) = A \ \exp(-\lambda_1 r)$$

$$f_A(r) = -B \ \exp(-\lambda_2 r) \tag{3.2.6}$$

f_R represents repulsive pair potential, and f_A represents attractive pair potential.

$$b_{ij} = \left(1 + \beta^n {\zeta_{ij}}^n\right)^{-1/2n} \tag{3.2.7}$$

As explained earlier, to introduce the local-environment depended on bond-order into the potential directly is the main feature of tersoff potential. And term b_{ij} does this job. As one can see from the b_{ij} function, it can increase or decrease the attractive part of the total

potential function depending upon local the environment (i.e., Higher bond strength in case the coordination number is low and vice versa). The mentioned coordination number is evaluated by function given below in equation 3.2.8 which is the number of nearest neighbors, while taking into account the distance between two neighbors $r_{ij} - r_{ik}$ and the bond angle θ.

$$\zeta_{ij} = \sum_{k \neq i,j} f_c(r_{ik}) g(\theta_{ijk}) \exp\left(-\lambda_3{}^m \left(r_{ij} - r_{ik}\right)^m\right); m \text{ is generally 3} \qquad (3.2.8)$$

In equation 3.2.9, θ_{ijk} is the bond angle between bonds ij and ik. And function $g(\theta)$ has a minimum for $h = \cos\theta$, which is already considered in equation 3.2.9. Apart from that, parameter d determines sharpness of function for dependence on angle and c represents the strength of the angular effect.

$$g(\theta) = 1 + \frac{c^2}{d^2} - \frac{c^2}{[d^2 + (\cos\theta - \cos\theta_0)^2]} \qquad (3.2.9)$$

During the present study, to simulate the crack propagation under mixed mode loading in SiC, the above mentioned tersoff potentials were employed to define the interactions between Si-Si, C-C, and Si-C. The potential function was again introduced by Tersoff in 1994 [159]. Lammps readable file was contributed by Saurav Goel, which is used as input potential file while running the code. The parameters are as mentioned below.

Table 3-2-1: Tersoff potential parameters used for Si and C for SiC [159]

	C	Si
$A\ (eV)$	1544.8	1830.8
$B\ (eV)$	389.63	471.18
$\lambda\ (\text{Å}^{-1})$	3.4653	2.4799
$\mu\ (\text{Å}^{-1})$	2.3064	1.7322
β	4.1612e-6	1.1e-6
n	0.99045	0.78734
c	19981	100390
d	7.034	16.217
h	-0.33953	-0.59825
$R\ (\text{Å})$	1.8	2.7
$S\ (\text{Å})$	2.1	3.0

Similar kind of potentials (i.e., tersoff potentials) were developed for ZrB_2 and HfB_2 by Daw et al. [160]. One thing worth noticing in the above potentials of SiC and the ZrB_2 one is β, n, c, d, h, m, and λ_3 are the parameters that depend only single type of atom from the pair. For example, in the case of ZrB_2 potentials, these terms will be derived only for individual species that is Zr or B. On the other hand, parameters A, B, λ, μ, R and S would depend upon both the particle type. Table below shows the parameters considered for designing tersoff potential for LAMMPS MD code [174].

Table 3-2-2: Tersoff potential parameters used for ZrB_2[160]

	Zr	B	Zr-B
$A\ (eV)$	3587.869733	1061.984813	1765.9542
$B\ (eV)$	37.10349	36.767392	40.02304
$\lambda\ (\text{Å}^{-1})$	2.91078	3.955278	3.360804
$\mu\ (\text{Å}^{-1})$	0.659036	1.190167	0.922057
β	1	0.541	-
n	1	21.885575	-
c	0	0	-
d	1	1	-
h	0	0	-
$R\ (\text{Å})$	4.6	2.2	3.18
$S\ (\text{Å})$	5.0	2.5	3.54
m	1	1	-
$\lambda_3\ (\text{Å}^{-1})$	1.32308	0	-

For the latter part of current work, MD simulation is done for a computationally tailored compound material system having ZrB_2 as core and SiC as a shell material to assess the mechanical property of the composite into core-shell type structure. To successfully achieve that model interaction at the interface are also required by MD code; that is an interaction between Zr-Si, B-Si, B-C, and Zr-B should be provided via valid potential functions into the MD code. Chen et al. [161] performed a molecular dynamics study to investigate Zr and Si diffusion behaviors during reactive diffusion process and

provided the tersoff potential for interaction between both the particle type. Following table indicates those parameters which were considered in this study while designing the interface of the computationally tailored composite.

Table 3-2-3: Tersoff potential parameter for Zr-Si interactions [161]

	Si-Si	Zr-Si
$A\ (eV)$	7835.380	2251.660
$B\ (eV)$	45.087	175.073
$\lambda\ (\text{Å}^{-1})$	3.851	2.603
$\mu\ (\text{Å}^{-1})$	1.079	1.474
β	0.429	0.468e-5
n	21.161	39.960
c	27340.700	4061.980
d	119.344	3.252
h	-0.330	-0.062
$R\ (\text{Å})$	2.783	3.216
$S\ (\text{Å})$	2.986	3.562

For interactions between boron and carbon, a well-developed tersoff potential is available from Kinaci et al. [162]. Since the potentials are designed for multiple structures between boron, nitrogen, and carbon, the parameters are not provided here, but the reader is suggested to read the corresponding study by Kinaci et al [162].

Interactions between Si and B are depicted by so-called Modified Tersoff potentials. Kumagai et al. added a continuous second-order differential cutoff function to the original tersoff potentials [163], as it found to be more accurate in predicting elastic modulus of the silicon with different isotopes. The following equation shows the modified cutoff function used in modified tersoff potentials.

$$f_c(r) = \begin{cases} 1, \ r \le R_1, \\ \frac{1}{2} + \frac{9}{16}\cos\left(\pi \frac{r-R_1}{R_2-R_1}\right) - \frac{1}{16}\cos\left(3\pi \frac{r-R_1}{R_2-R_1}\right), \ R_1 < r < R_2, \\ 0, \ r \ge R_2 \end{cases} \quad (3.2.10)$$

Where, $R_1 = R$ and $R_2 = S$ when compared to the original tersoff potential function.

And, function $g(\theta)$ takes following form,

$$g(\theta) = c_1 + g_0(\theta)g_a(\theta) \tag{3.2.11}$$

where,

$$g_0(\theta) = \frac{c_2(h - \cos\theta)^2}{c_3 + (h - \cos\theta)^2}$$

$$g_a(\theta) = 1 + c_4 \exp[-c_5(h - \cos\theta)^2]$$

Also, coordination number is derived from the following equation,

$$\zeta_{ij} = \sum_{k \neq i,j} f_c(r_{ik}) g(\theta_{ijk}) \exp\left(-\alpha(r_{ij} - r_{ik})^{\beta}\right) \tag{3.2.12}$$

Lammps, MD simulation package, provides an option to assign modified tersoff pair style via tersoff.mod potential files. In the present study interaction between Si and B was given by this method as mentioned earlier, and parameters used to write lammps readable file were taken from Kumagai et al. [164]

Table 3-2-4: Modified tersoff potential parameters for Si-B interactions [164]

	Si-Si	Si-B	B-Si	B-B
$A\ (eV)$	1830.80	2950.58	2950.58	668.926
$B\ (eV)$	471.180	34.7505	34.7505	70.5639
$\lambda_1\ (\text{Å}^{-1})$	2.47990	4.12560	4.12560	3.31111
$\lambda_2\ (\text{Å}^{-1})$	1.73220	1.03934	1.03934	1.43284
η	0.787340	1.19517	1.62428	4.70000
δ	0.635050	0.418351	0.436657	0.114895
$R_1\ (\text{Å})$	2.7	2.5	2.5	2.3
$R_2\ (\text{Å})$	3.0	2.8	2.8	2.6
$R_e\ (\text{Å})$	2.351	1.93547	1.93547	1.664

Table 3.2.4 – *Continued*

	Si-Si-Si	Si-Si-B	Si-B-Si	Si-B-B	B-Si-Si	B-Si-B	B-B-Si	B-B-B
α	5.1975	1.52454	1.52454	1.26696	0.591417	0.0	0.0	1.05655
β	3	1	1	1	1	1	1	1
c_1	1.09e-6	0.0395	0.0097	0.2890	0.1634	0.1839	0.4233	0.1568

Table 3.2.4 – *Continued*

c_2	42.149	0.8415	0.2072	4.0163	4.5583	2.7999	6.4420	0.2931
c_3	262.99	0.9362	0.9362	7.8984	5.4865	4.3192	4.3192	0.25e-4
h	-0.5982	-0.4285	-0.4285	-0.6464	-0.7	-0.4531	-0.4531	0.37

3.2.3 Lennard-Jones Potentials

Lennard-Jones potential is a mathematically simple model that approximately predicts the interaction between a pair of molecules. John Lennard-Jones presented the first form of this interatomic potential in 1924 [165], and the most known expression of the potential is presented below.

$$V(r_{ij}) = 4\epsilon\left[\left(\frac{\sigma}{r_{ij}}\right)^{12} - \left(\frac{\sigma}{r_{ij}}\right)^{6}\right] \tag{3.2.13}$$

Where ϵ is depth of the potential well, σ is the interatomic distance at which pair potential becomes zero and r is the distance between particles. The term, $(1/r\_ij)$^12 represents the repulsion between atoms when they are brought too close to each other and the term $(1/r\_ij)$^6 which by seeing figure 3-3 one can say that is dominating for large distance and represents the attractive part to describe cohesion between molecules. The following curve represents above mentioned form of potential relating potential energy with interatomic distance.

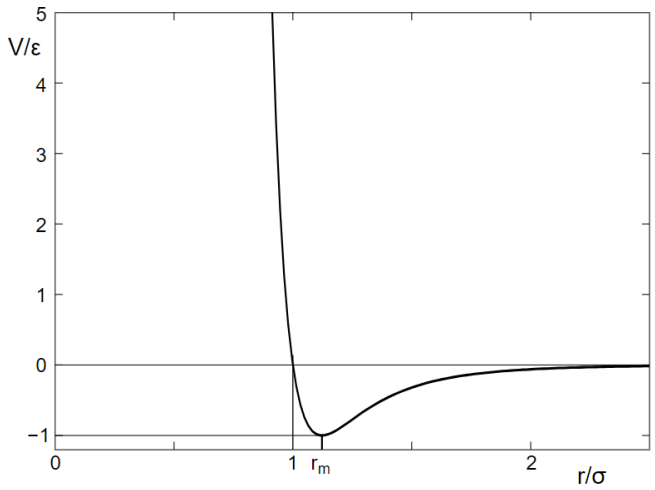

Figure 3-3: LJ-potential curve in reduced units

In the figure 3-3, r_m represents the interatomic distance at which potential energy at equilibrium of the pair, and is related to σ by, $r_m = 2^{1/6}\sigma$. For any interacting pair, with these parameters fitted appropriately, one can reproduce the experimental data or accurate quantum chemistry data. LJ-potentials are widely used into MD simulation even today owing to their simple form and fast performance on computers.

Explicitly, no interatomic potentials are available to define interactions between Zr and C atom at the interface of ZrB_2 and SiC. As developing such interatomic potential is not the aim of the present study, one can look up for the experimental or Density Functional Theory (DFT) simulated data which might give some insight about the cohesive energy, bond length, atomic orientations and surface energy between Zr-C bond. Once sufficient data is collected one can relate these data to find appropriate value of Lennard-Jones parameters ϵ and σ so that projected interaction between Zr-C by Lennard-Jones potential can generate general behavior of the bond. One should keep in mind that LJ potential does not give any idea of material property in detail.

Ju li et al. [166] developed the force-based many-body potential for ZrC in the form of a modified second-moment approximation with emphasis on the strong directional dependence of the C-Zr bond. Following are the equations representing the potential.

$$E^{tot} = \sum_{i \in A} V_i + \sum_{i \in B} V_i,$$

$\forall i \in A$,

$$V_i = \sum_{j \in A \neq i} \phi_{AA}(r_{ij}) + \sum_{j \in B} \phi_{AB}(r_{ij}) - X_i^{1/2},$$

$$X_i = \sum_{j \in A \neq i} h^2{}_{AA}(r_{ij}) + \sum_{j \in B} h^2{}_{AB}(r_{ij}),$$

$\forall i \in B$,

$$V_i = \sum_{j \in A} \phi_{BA}(r_{ij}) + \sum_{j \in B \neq i} \phi_{BB}(r_{ij}) - X_i^{1/2},$$

$$X_i = \textstyle\sum_{j \in A} h^2{}_{BA}(r_{ij}) + \sum_{j \in B \neq i} h^2{}_{BB}(r_{ij}), \quad (3.2.14)$$

Where,

$$\phi_{AB}(r_{ij}) = \phi_{BA}(r_{ij}),$$

$$h^2{}_{AB}(r_{ij}) = h^2{}_{BA}(r_{ij}) \quad (3.2.15)$$

And, A = Zr and B = C

And, function ϕ and h are given as,

$$\phi_{ZrZr}(r) = \exp\left[A_{ZrZr}(B_{ZrZr} - r) + \frac{K}{r - r_c^{ZrZr}}\right](eV),$$

$$h^2{}_{ZrZr}(r) = \exp\left[C_{ZrZr}(D_{ZrZr} - r) + \frac{K}{r - r_c^{ZrZr}}\right](eV^2), \quad (3.2.16)$$

$$\phi_{ZrC}(r) = \phi_{CZr}(r) = \exp\left[A_{ZrC}(B_{ZrC} - r) + \frac{K}{r - r_c^{ZrC}}\right](eV),$$

$$h_{ZrC}(r) = h_{CZr}(r) = \exp\left[C_{ZrC}(D_{ZrC} - r) + \frac{K}{r - r_c^{ZrC}}\right](eV), \quad (3.2.17)$$

$$\tilde{h}_{ZrC}(i = Zr, j = C) = h_{ZrC}(r_{ij}) \times \exp\left[-\frac{\sqrt{S_{ij}}}{h_{ZrC}(r_{ij})}\right], \quad (3.2.18)$$

$$S_{ij} \equiv \sum_{l\in C, l\neq j}\left(\frac{1+\cos\theta_{lij}}{\alpha_{ZrC}}\right)^{\beta_{ZrC}} h^2{}_{ZrC}(r_{il}) + \sum_{k\in Zr, k\neq i}\left(\frac{1+\cos\theta_{kji}}{\alpha_{CZr}}\right)^{\beta_{CZr}} h^2{}_{ZrC}(r_{jk}), \quad (3.2.19)$$

And, corresponding parameters are listed below,

Table 3-2-5: Parameters for Force-based potential of ZrC [166]

	Zr-Zr	Zr-C
A (Å^{-1})	2.9296875	3.24589393669854
B (Å)	2.58787395638939	2.05679804919117
C (Å^{-1})	1.32308467741935	0.82303818052368
D (Å)	4.3672464262563	4.15482225815134
K (Å)	0.1	0.1
r_c (Å)	7.0	3.5
α_{ZrC}	-	1.80853303846249
β_{ZrC}	-	14.59345494373451

Due to unavailability of the above mentioned potential function in the form of LAMMPS readable file, the idea is, to use above mentioned potential model to determine the energy with respect to interatomic distance for some specific number of atoms. Once done, one can achieve the required parameters for LJ potential to describe Zr-C bond and that can be used in LAMMPS MD code. The atomic structure considered here comprises 8 atoms in cubic form. In other words, NaCl type structure for ZrC (i.e., B1-ZrC) is considered, and only 1/4th part of a lattice is chosen to evaluate the bond energy and bond length of the model. Figure 3-4 below shows the undertaken model.

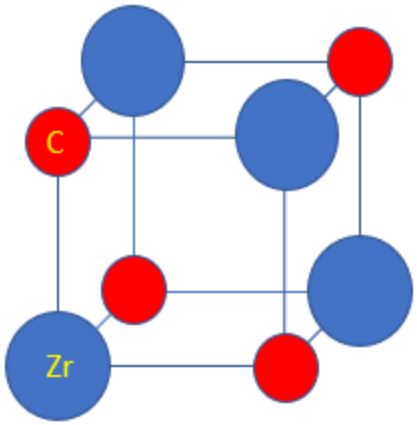

Figure 3-4: considered atom structure to obtain bond energy between Zr-C

As discussed earlier, the above-displayed model was considered, and atomic potential energy was plotted by coding the above-mentioned Ju li's potential function using MATLAB. Figure 3-5 below, displays potential energy curve for an interatomic distance of two adjacent atoms (Zr and C) from 0.5 Å to 8.5 Å. Figure 3-5-b shows magnified the view of the plotted curve, and one can see that the potential energy given by the function is -16.8 eV at a bond length of 2.5 Å, which is close to values achieved by both experiments and simulations. [166, 167].

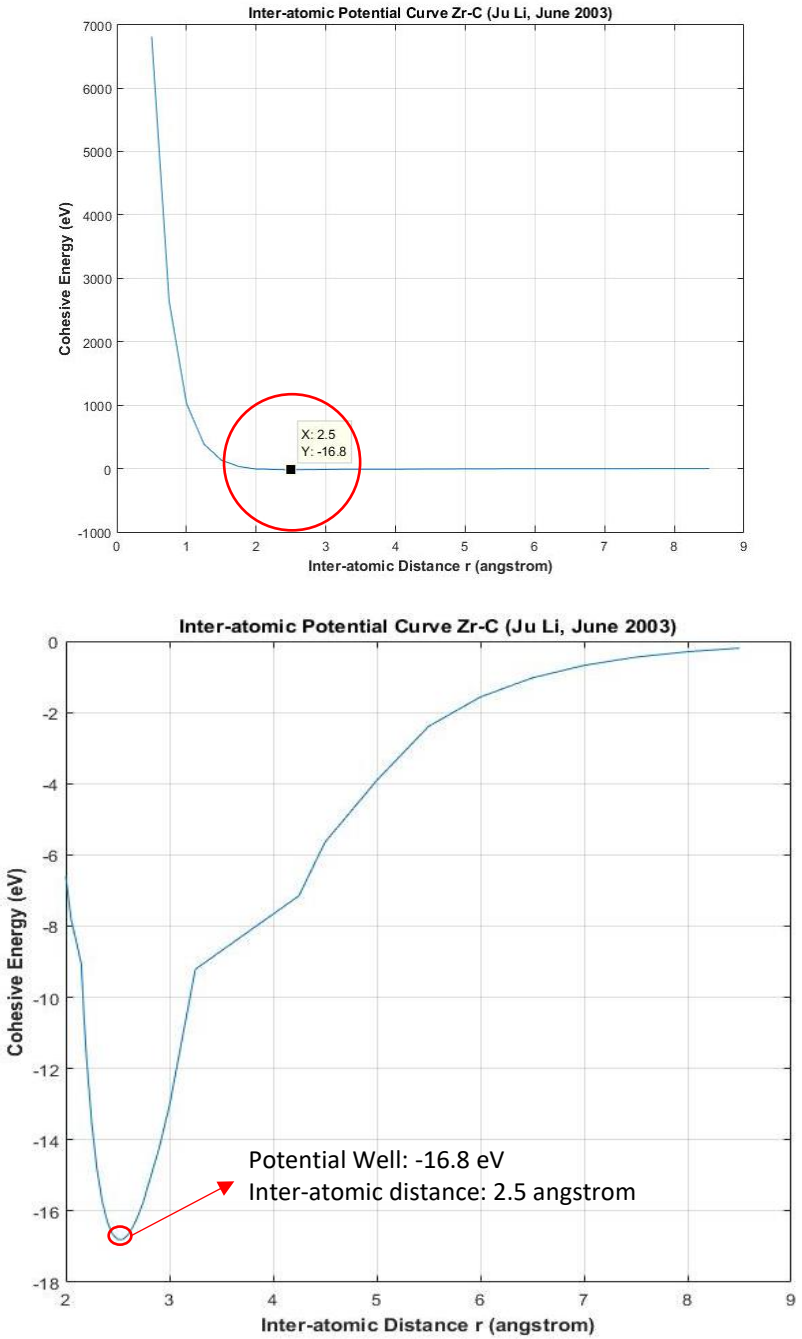

Figure 3-5: Potential curve for 1/4th cell of B1-ZrC (8 atoms, [fig 3-4]) obtained by plotting Ju li's potential function in MATLAB

Hence, one can take following values for LJ potential parameter for MD simulations.

Table 3-2-6: Obtained values of LJ parameters for Zr-C bond

LJ-parameter	The potential energy from Ju li's potential curve [Fig. 3-5]	From Zr-C Bond length (r_m) [167]
ϵ (eV)	$\frac{-16.8}{8} = -2.1\ (per\ atom)$	-
$\sigma = \frac{r_m}{2^{1/6}}$ (Å)	$\frac{2.5}{2^{1/6}} = 2.2272$	$\frac{(2.31 - 2.37)}{2^{1/6}} = 2.05 - 2.11$

But one may argue that the obtained values of LJ parameters are extracted from the result obtained for only 8 atoms, interacting in a very specific way to remain in structure mentioned in figure 3-4. Such structure is certainly not found experimentally to exist between the interface region of ZrB_2 and SiC. Therefore, one might end up selecting cohesive energy very high than the actual one. Also, from the table 3.2.6, one can say the obtained curve minimum r_m of 2.5 Å over-estimates the bond length found in actual ZrC's Zr-C bond. And also, for the fact that Ju li's potential for ZrC (which has mixture of metallic, covalent and ionic bonds) are developed for many-body interactions, considering a limited number of atoms to derive these parameters is not the optimal way.

As an alternative way, one can consider the data available for materials whose interface has a bond between Zr and C atom. Since cohesive energy for any system is scalable, one can derive bond energy for Zr-C bond in such system, and from that, required LJ parameters can be obtained. Y. An et al. [168], carried out interface study of graphene/ZrB_2 ceramic structure by molecular dynamics simulation. Figure 3-6, given below compares bond between Zr and C found in graphene/ZrB_2[168] and SiC/ZrB_2[169].

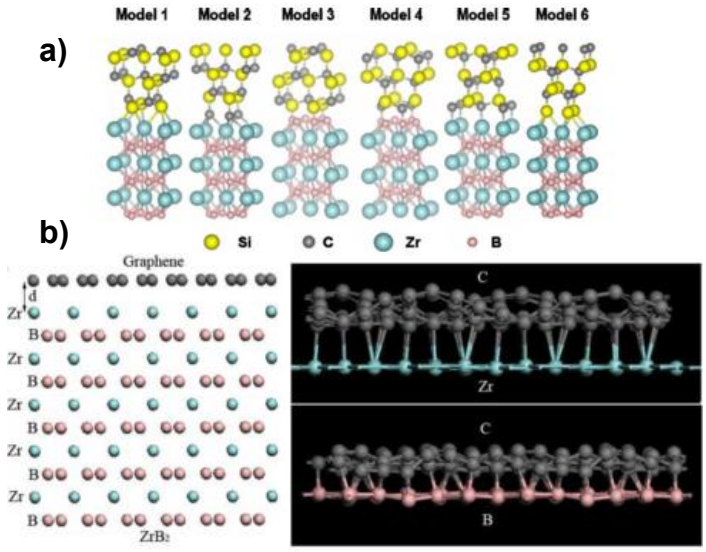

Figure 3-6: Zr-C bond at a) SiC[111]/ZrB_2[0001] interface (Model- 2, 5) [169] b) graphene/ZrB_2[0001] interface [168]

One can see from figure 3-6, very similar type of Zr-C bond exists between the interface of both the ceramic composites. Y. An et al. reported bonding energy of 11.97 J/m^2 for the interface in which carbon atom from graphene is connected with Zr atom of termination layer in ZrB_2. As this simulation was carried out for 8*8 lattice graphene layer and 6*6 lattice ZrB_2(0001) layer, one can determine that number of the atom at the interface will be 186 from the lattice structure of both the materials at the interacting surface area of 286.8978 $Å^2$. Hence, from this data, one can derive bonding energy in the form of per-atom energy to estimate the strength of a single pair of Zr and C atom.

Hence,

$$E_b = \frac{11.97\ (J/m^2) \times 286.8978\ (\ interface\ Area\ in\ Å^2)}{10^{20}\ (1\ m^2\ Area\ in\ Å^2) \times 186\ (no.of\ atoms\ at\ interface)}\ \text{(J/atom)} \qquad (3.2.20)$$

And, as,

1 joule = 0.000239 kcal,

1 mol = 6.022 x 10^{23} atoms &

23.061 kcal/mol = 1 eV,

One can determine bond energy E_b(Zr-C) to be 2.3046 eV, which was used as LJ parameter 'ϵ' for simulation of computationally designed core/shell type ZrB_2/SiC composite system. Bond length was still found to be in range of 2.31-2.37 Å, leading LJ parameter 'σ' equals to 2.05-2.11 Å, as mentioned in table 3.2.6. σ = 2.08 Å was chosen for this study.

3.3 : Integration Algorithm

Velocity-Verlet time stepping algorithm is used by LAMMPS to determine velocity, next position, and force of the particles. As discussed earlier, once the potential function is set, the second order equation of motion presented in Eq. 3.2.1 are solved with the help of Velocity-verlet algorithm, which is presented below.

$$m_i \cdot v_i\left(t + \frac{1}{2}\delta t\right) = m_i \cdot v_i(t) + \frac{1}{2}\delta t \cdot f_i(t)$$

$$r_i(t + \delta t) = r_i(t) + \delta t \cdot v_i(t + \frac{1}{2}\delta t)$$

$$m_i \cdot v_i(t + \delta t) = m_i \cdot v_i\left(t + \tfrac{1}{2}\delta t\right) + \tfrac{1}{2}\delta t \cdot f_i(t + \delta t) \qquad (3.3.1)$$

Above mentioned algorithm, first determines velocity due to initially provided atom positions and sequentially determines new positions, evaluates force and acceleration and determines new velocity before going to the next step. The significance of this algorithm is that it is very simple in nature and intuitive, simple to program, time-reversible as well as, low order in time, thus, permitting simulations to take longer timesteps and requires only one force evaluation per timestep, making the simulation run faster.

3.4 : MD simulations: Model details

3.4.1 Mixed Mode Fracture Analysis in Al, SiC, and ZrB_2

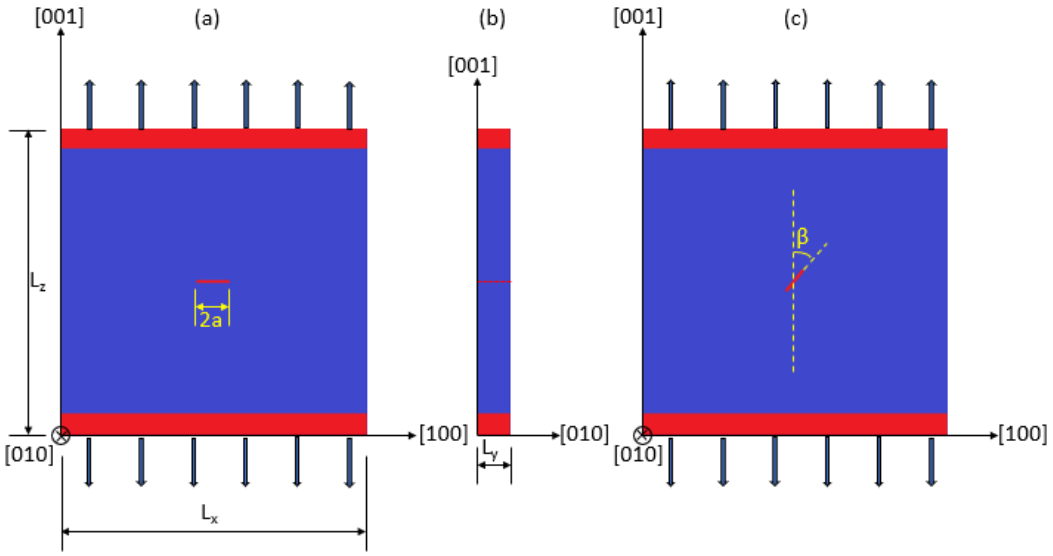

Figure 3-7: Model geometries with a) central planer crack (2a = 5 lattice units), b) side view of the model (L_y, dotted line represents through the plane crack), c) Planer crack inclined by angle 'β' from loading direction

In present work, the crack propagation in three different single crystal materials with initial planer crack under mixed mode loading is studied. As one can see, from figure 3-7(a), critical stress intensity factor was obtained from propagation of central crack under mode-I loading and to study effect of mixed mode loading, crack at some angle β from the uniaxial loading direction was introduced, as it has been proved that inclined crack under uniaxial tension induces mixed mode fracture. For all three materials, Al, SiC and ZrB_2 seven atomistic models with different crack orientation were selected to check the effect of crack inclination angle on fracture toughness and crack growth direction. Effects of blunt crack and sharp crack were also studied. To induce the effect of crack in infinitely large and thin plane, the dimension of the atomic model in X and Z direction was kept much

higher than in Y direction. For both Al and SiC length of the model before relaxation was kept 50 lattice units in X and Z directions and 5 lattice units in the Y direction. As ZrB_2 has a hexagonal lattice with different lattice units in all three directions, the dimension of ZrB_2 single crystal model was chosen so as to approximately match the dimension with undertaken Al and SiC model lengths. For blunt crack 5 lattice unit's worth atoms were deleted from the crystal to create the initial defect, whereas to create sharp crack molecular interactions were turned off between the pair of atoms on opposite side of the crack. Following figure displays, a molecular model with different orientation of cracks undertaken for the study.

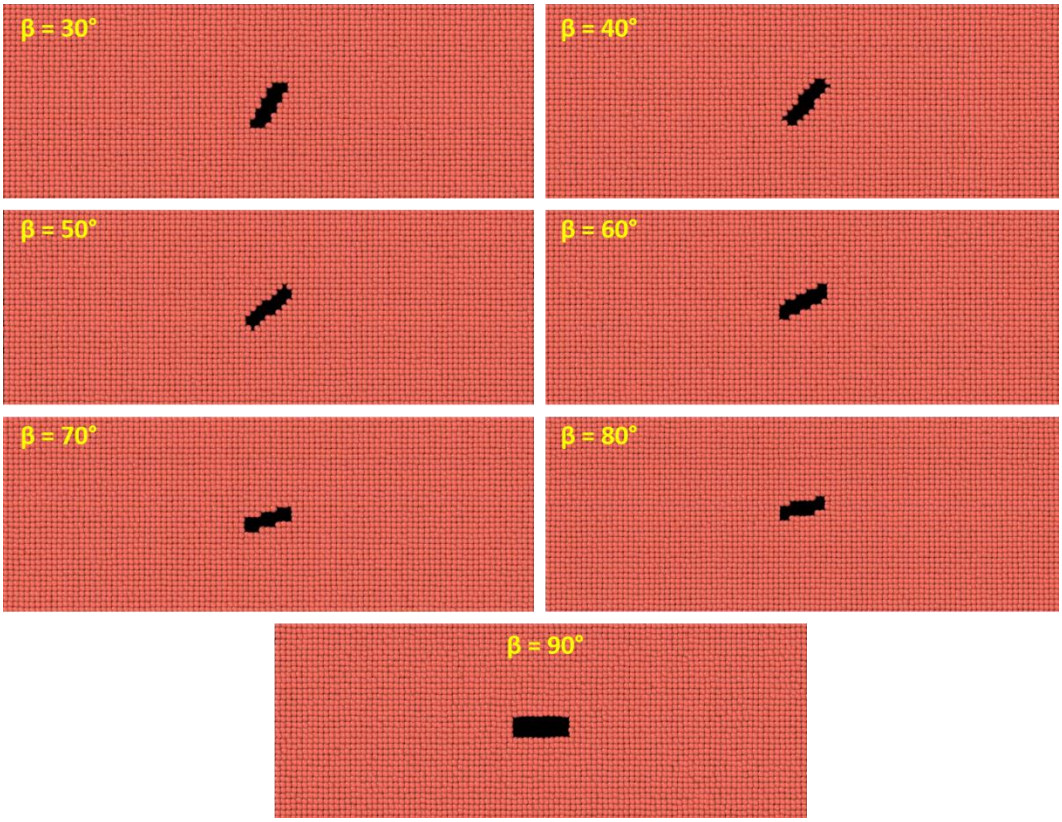

Figure 3-8: Atomistic models of blunt crack with different orientations in Al single crystal

As shown in Figure 3-8 and 3-9, models having a blunt crack and sharp cracks at different orientations were considered for MD simulation for all three materials, Al, SiC, and ZrB_2. Uniaxial loading was applied as shown in figure 3-7, along the Z direction.

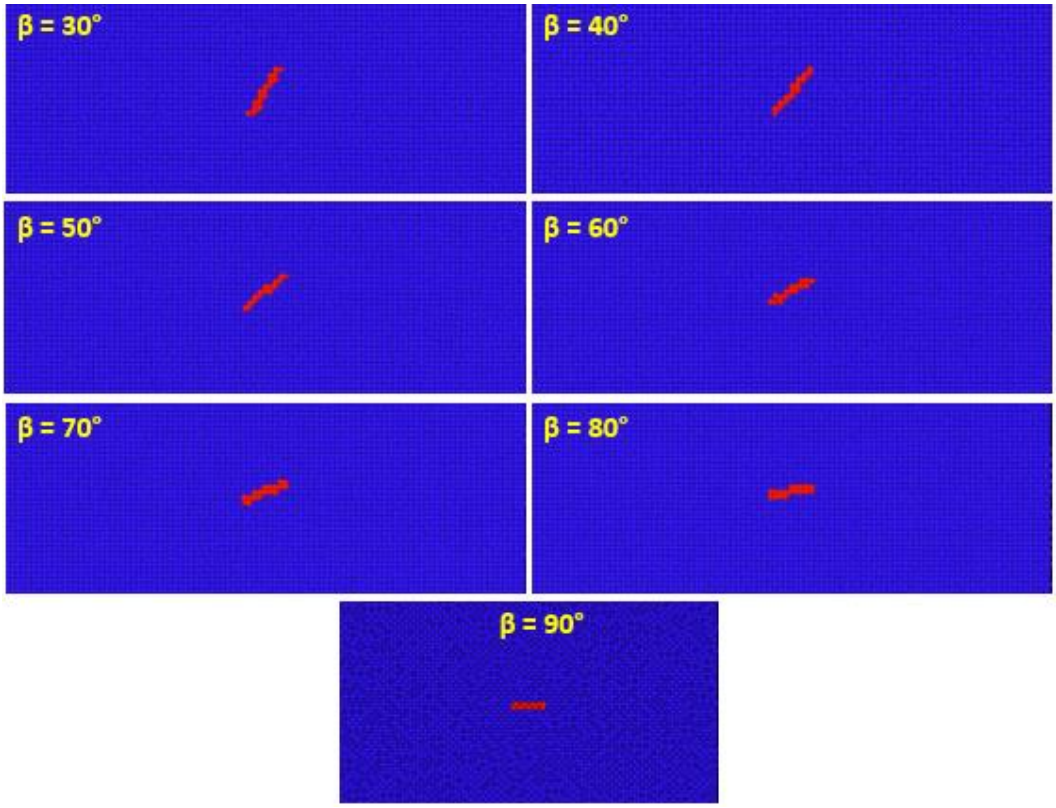

Figure 3-9: Atomistic models of sharp crack with different orientations in Al single crystal

One must know that results from MD simulations greatly depends upon what boundary condition is chosen for the model under analysis and it is very critical to choose the boundary conditions as close as possible to real experimental set-up. Especially, in the cases like the present study where the main aim of the study is to check the agreement of MD simulations with experimental and analytical results. From the model represented in figure 3-7, the simulation region has 6 faces, none of which should act as a free boundary

as our aim is to simulate the crack propagation in bulk material and also, atoms on the free surface have considerably high energy than atoms present inside the material/bulk. Hence, periodic boundary conditions were chosen all around the region to simulate the effect of infinite material bulk. What periodic boundary conditions really does is, it creates an infinite array of images of the original region and behavior like the motion of the atoms are connected across the boundaries, that is, an atom leaving the boundary of one region will enter from adjacent boundary to neighbor image of the simulation cell. Also, periodic boundary condition not only defines the interaction between atoms at the boundary of two adjacent simulation cells but also adds the forces from all the images the particles are in infinitely many repeated simulation cells as shown in figure 3-10 below.

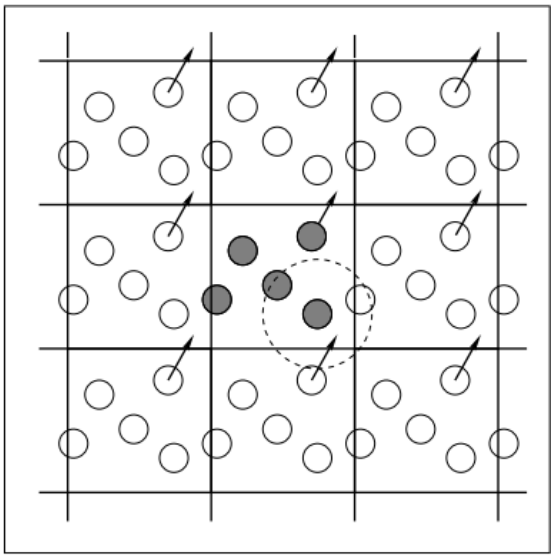

Figure 3-10: Ideology of Periodic Boundary Conditions [170]

Hence, one can easily avoid the effect of free surfaces in atomic simulations by applying periodic boundary conditions with slight increment in computational complexity. While creating the atomic model for present study, the care has been taken to avoid interactions between cracks in two adjacent image cells, by keeping dimension of

simulation cell much larger than a crack along the crack direction. The corresponding model dimensions are listed in table 3.4.1.

The atomic interactions used for force calculation were EAM potential for Aluminum single crystal and tersoff potentials for SiC and ZrB_2 single crystals. All models are simulated under periodic boundary conditions using LAMMPS MD code with a timestep of 1fs and temperature of 300 K. The Al, and SiC single crystal are arranged with cubic orientations with X = [100], Y = [010] and Z = [001]. As discussed earlier few atom layers in XY-plane were deleted to generate blunt crack defect into perfect crystals before relaxation. The interactions between specific groups of atoms were turned off to simulate the effect of sharp crack, as blunt crack may add extra energy due to the free surfaces created owing to removal of the atoms. Once, the models with cracks are achieved, they are equilibrated for 10 ps under micro-canonical ensemble (i.e., constant volume and energy ensemble/NVE ensemble) to get rid of any high surface energies due to crack creation. Once equilibrated under NVE ensemble, models were equilibrated for 50 ps under isobaric-isothermal (NPT) ensemble with target pressure being 0 bar to get initial stress-free state at prescribed temperature of 300 K. Subsequently, the models are subjected to pure tensile loading by moving two outer most layers (e.g., Red colored layers in figure 3-7) along Z direction with prescribed displacement (Δu_z) of 0.1 Å within 1 ps while relaxing the system constantly under NVT ensemble. During the simulation, data is recorded after every 1 ps and next increment is applied.

Table 3-4-1: Initial model dimensions for Al, SiC, and ZrB_2

Material	Lattice Constant (Å)	L_x (Å)	L_y (Å)	L_z (Å)	Crack Length '2a' (Å)
Al	a = 4.04	50a=202.0	5a=20.2	50a=202.0	5a=20.2
SiC	a = 4.3596	50a=217.98	5a=21.798	50a=217.98	5a=21.798
ZrB_2	a = 4.7535	50a = 237.675	8b = 21.955	68c = 240.187	5a = 23.7675
	b = 2.74435				
	c = 3.53217				

3.4.2 Computational Modeling of Core-Shell structure of ZrB_2/SiC ceramic composite

D. Sciti et al. [130] reported on the effect of different microstructure evolved due to pressure-less sintering of ZrB_2 and SiC with additives like Si_3N_4 and $MoSi_2$. From the two different microstructures undertaken, they found that processing induced SiC's anisotropic growth from particles to platelets type structure with ZrB_2 serving as a core structure and SiC platelets agglomerating with Si_3N_4 liquid phase to form shell structure, ultimately increasing the fracture toughness of the composite. Hence, the second aim of the current work is to develop an atomic model of core-shell type structure for ZrB_2-SiC ceramic and check for its mechanical behavior. Figure 3-11 below, shows microstructure observed by Sciti et al. during their experiment.

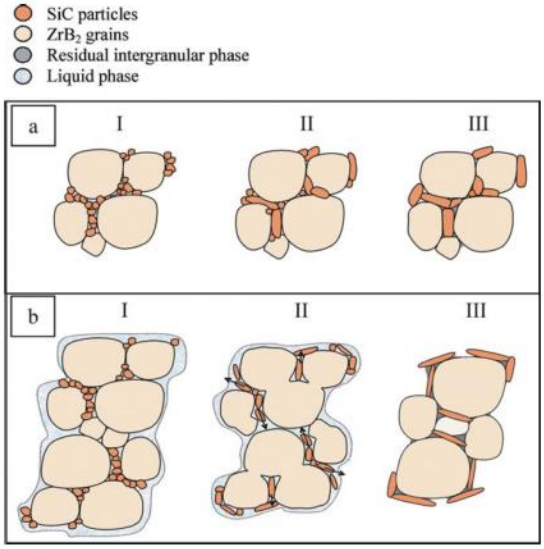

Figure 3-11: Microstructure mechanisms evolved between 1900 °C and 2100 °C [130]

One must keep in mind that the grains when experimentally produced, have very irregular shape. While creating such irregular shape computationally is not a viable option, one can study the morphological effect by creating simpler geometry which can still capture

the necessary effect of the microstructure generally. Hence, as a very initial study, only cubic cor-shell structure is considered to carry out MD simulation in this study.

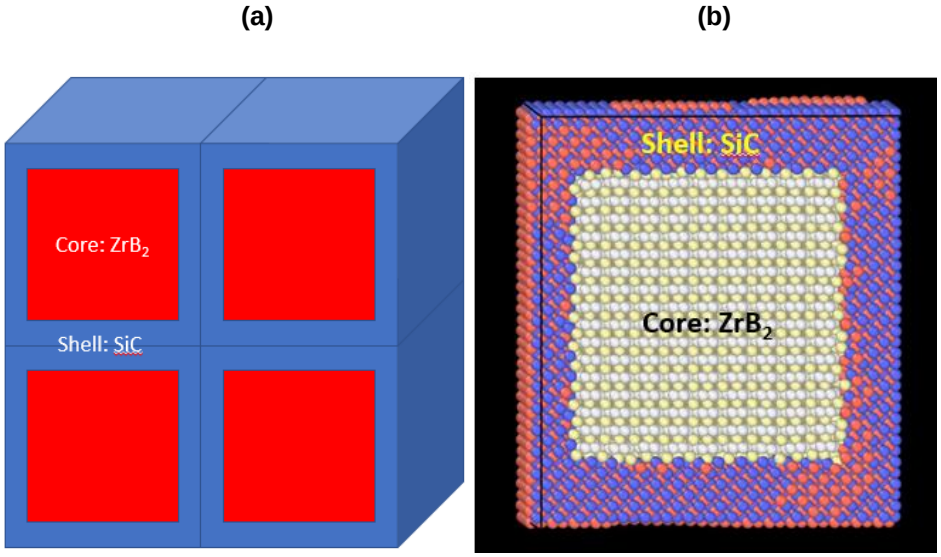

Figure 3-12: (a) Conceptual Core-shell structure for ZrB_2-SiC composite structure (b) Cross-section of atomistic model considered in present molecular dynamics study

As explained earlier, periodic boundary conditions are applied around the whole system. Molecular interactions are given by different potential functions, such as Zr-B, Si-C, Zr-Si and C-B by tersoff potential function; B-Si by modified tersoff function and interactions between Zr and C are defined by LJ parameters as obtained from bond energy calculations mentioned in the previous section of atomic interactions. Orientation of both ZrB_2 (core) and SiC (shell) is X=[100], Y=[010] and Z=[001]. Atoms from perfect SiC crystal are deleted to fit ZrB_2 into the cavity. Firstly, to get the initial stress-free state at a prescribed temperature of 300 K, the system is first relaxed under isobaric-isothermal (NPT) ensemble for 200 ps with target pressure to 0 bar, which is followed by canonical (NVT) ensemble for another 200 ps. On the second step, the whole system is subjected to pure tensile loading by moving two outer most layers along the Z direction with the incremental displacement

(Δu_z) of 0.02 Å over 1 ps under NVE ensemble. The time-step chosen for the simulation is again 1fs and since NVE ensemble does not control temperature, a separate thermostat has been applied which rescales velocity of atoms at every 5 time-steps to maintain the system temperature at 300 K if the temperature deviates more than ±5 K.

Chapter 4 Results and Discussions

As mentioned in previous chapter, three different material systems, respectively, single crystal Al, SiC, and ZrB_2 with the initial defect are studied for crack propagation under mixed mode loading condition. Below are the results generated from MD simulations and Maximum Stress criterion. Crack propagation angles, remote stress at failure and overall mechanical response of the systems are reported. In the last section overall mechanical response of the core-shell type ZrB_2/SiC ceramic composite system is shown.

4.1 : Mixed mode fracture analysis in Aluminum

4.1.1 Molecular dynamics simulation results

An atomistic system of single crystal Al with dimensions mentioned in Table 3.4.1 is considered. The atomic model with different orientation of crack is already displayed in Figure 3-8 and 3-9 for blunt crack and sharp crack in aluminum single-crystal respectively. The initial configuration, configuration after relaxation and configurations just before and after crack propagation are reported in the figure 4-1 (Case -1 to Case--7) and 4-2 (Case-1 to Case-7) for blunt crack and sharp crack respectively. The data is collected over 140 ps and 7.69% of strain for blunt crack models and over 160 ps and 8.79% of strain for sharp crack models.

In solids, the centro-symmetry parameter is a very useful measure of the local lattice disorder around an atom. It conveys the information about every atom that, whether an atom is part of the perfect lattice, a local defect or free surface. The figures displayed below is color-coded with centro-symmetry parameter [171] by using centro/atom feature of LAMMPS. The atoms in green color represent them as a part of perfect FCC lattice structure whereas red atoms around crack are dislocated atoms, and those around edges

are not in contact with their periodic simulation cell and are no longer part of perfect FCC structure.

Presented below, are MD results of crack propagation under mixed mode loading in single crystal Aluminum with blunt crack,

Case – 1, β=30°

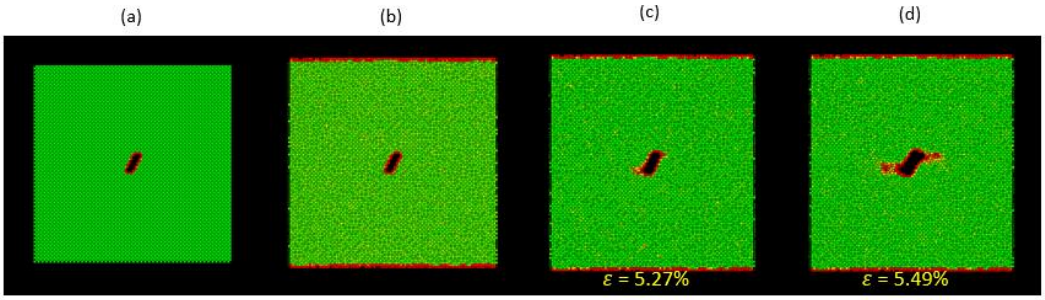

Case – 2, β=40°

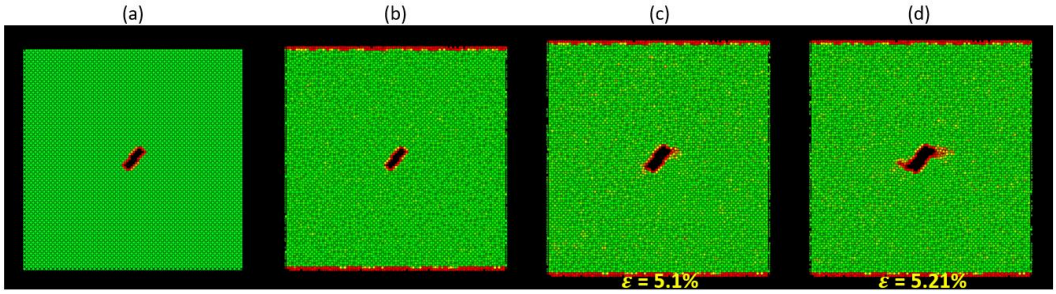

Case – 3, β=50°

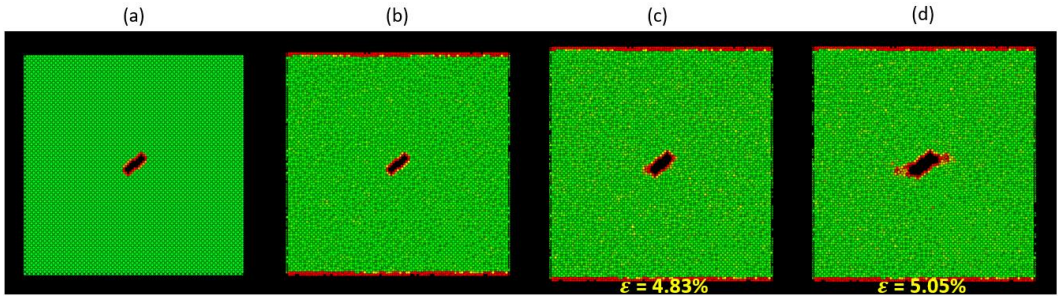

Case – 4, β=60°

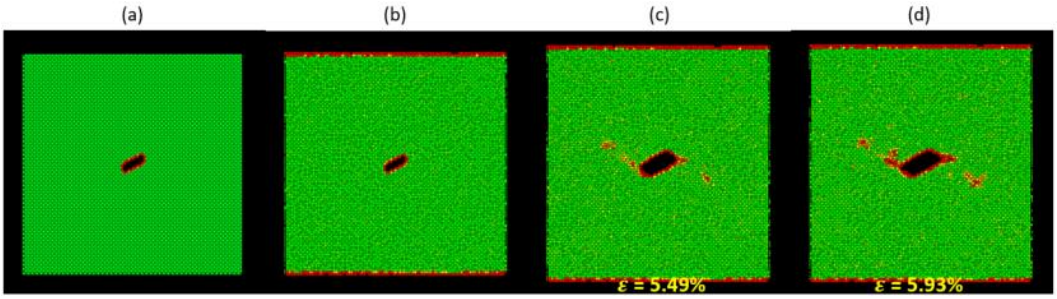

Case – 5, β=70°

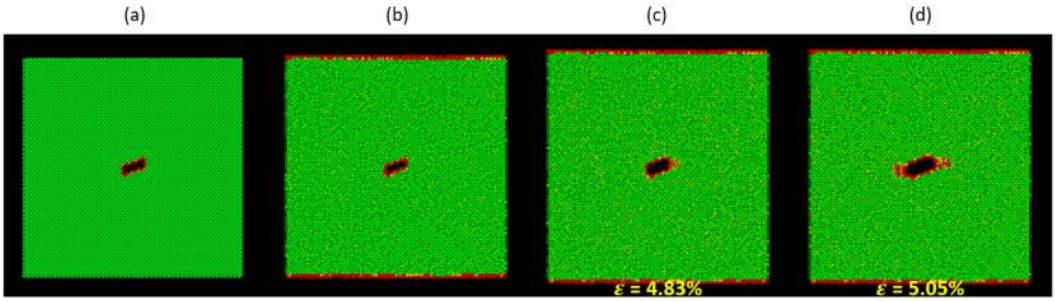

Case – 6, β=80°

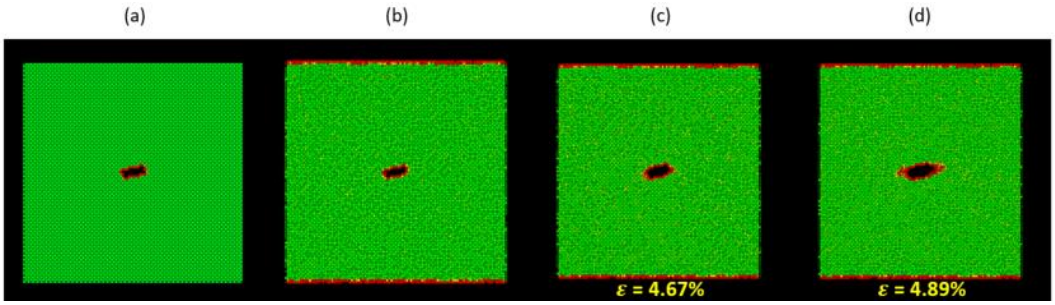

Case – 7, β=90°

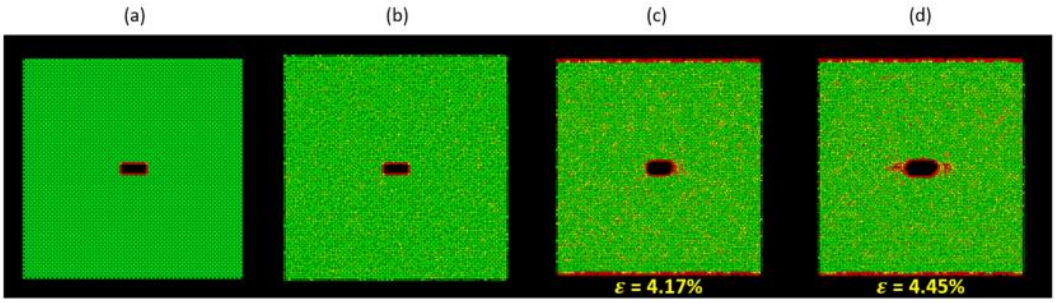

Figure 4-1: MD simulation results for inclined blunt crack in Al, oriented at β=30°(case-1) to β=90°(case-7), (a) Initial Configuration (b) System after relaxation (c) Strained system just before crack propagation (d) System when crack propagates; (case-1 to case-7)

Presented below, are results for sharp crack in Aluminum crystal,

Case – 1, β=30°

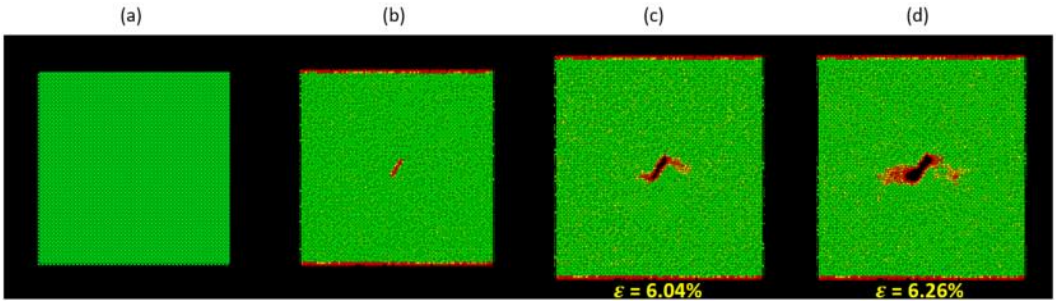

Case – 2, β=40°

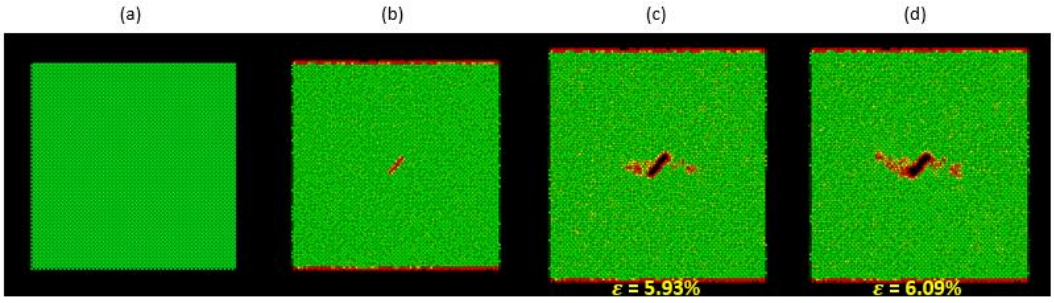

Case – 3, β=50°

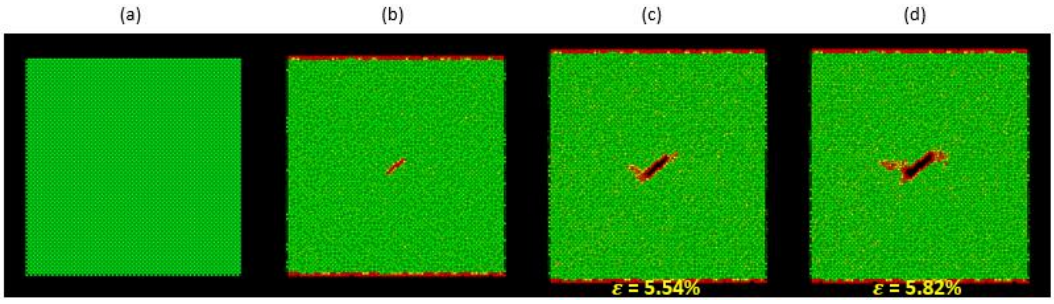

Case – 4, β=60°

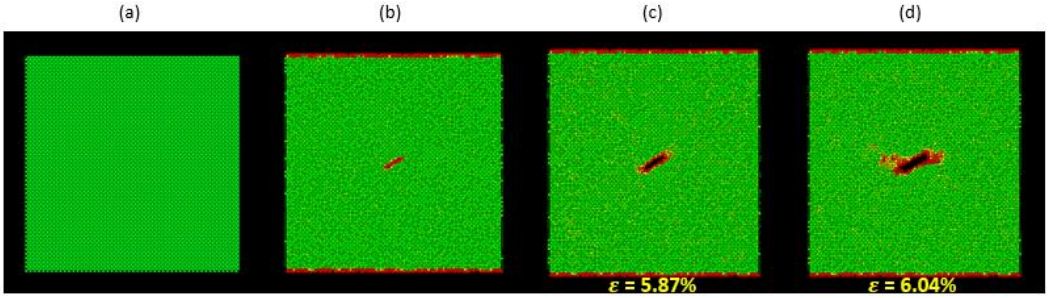

Case – 5, β=70°

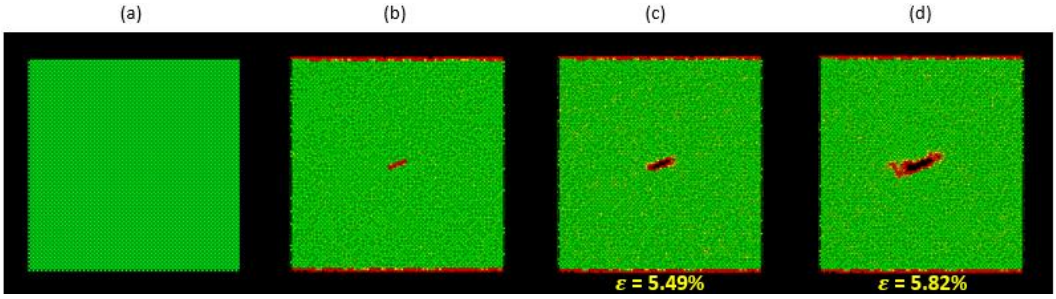

Case – 6, β=80°

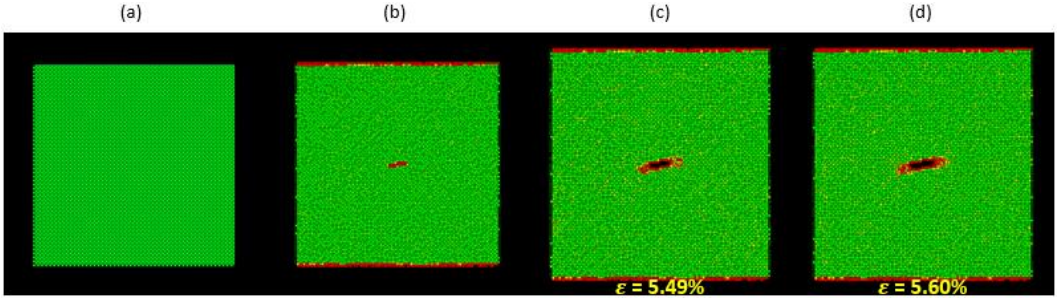

Case – 7, β=90°

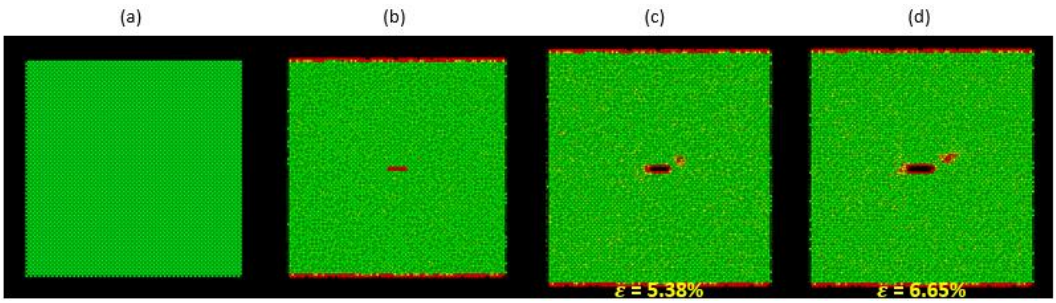

Figure 4-2: MD simulation results for inclined sharp crack in Al, oriented at β=30°(case-1) to β=90°(case-7), (a) Initial Configuration (b) System after relaxation (c) Strained system just before crack propagation (d) System when crack propagates; (case-1 to case-7)

Given below are the mechanical responses of the systems with the different crack orientation of blunt and sharp crack respectively. With the figures given in figure 4-1 (Case-1 to Case-7) and figure 4-2 (Case-1 to Case-7), one can compare the images (a), (b), (c) and (d) with stress-strain curve given in Figure 4-3 and 4-4 respectively. Image (a) and (b) displays system before and after relaxation and corresponds to the zero-stress point (i.e., initial point) on the stress-strain curve. Image (c) corresponds to near peak value in the stress-strain curves where the crack is about to propagate, and stresses are maximum, whereas, image (d) corresponds to the region after peak stress on stress-strain curves during which crack propagates ultimately rendering system to complete failure.

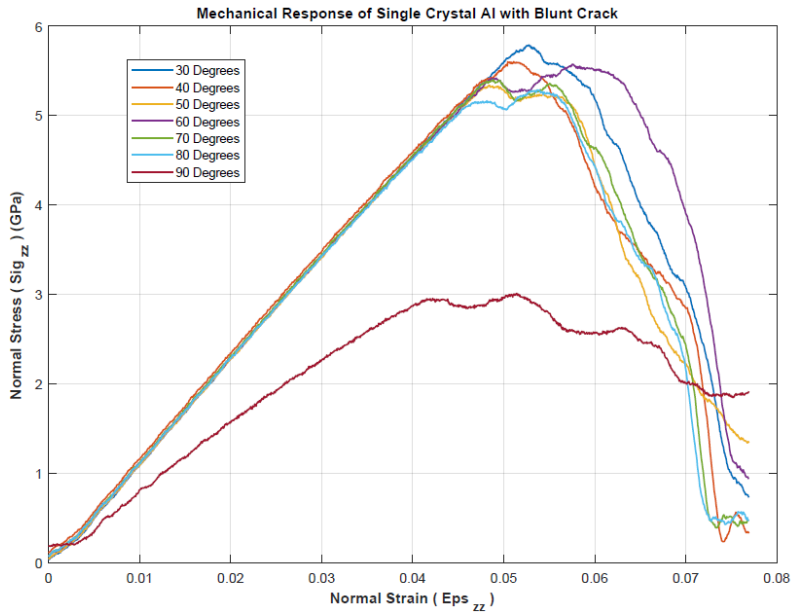

Figure 4-3: Mechanical response of single crystal Al with blunt crack at different orientation

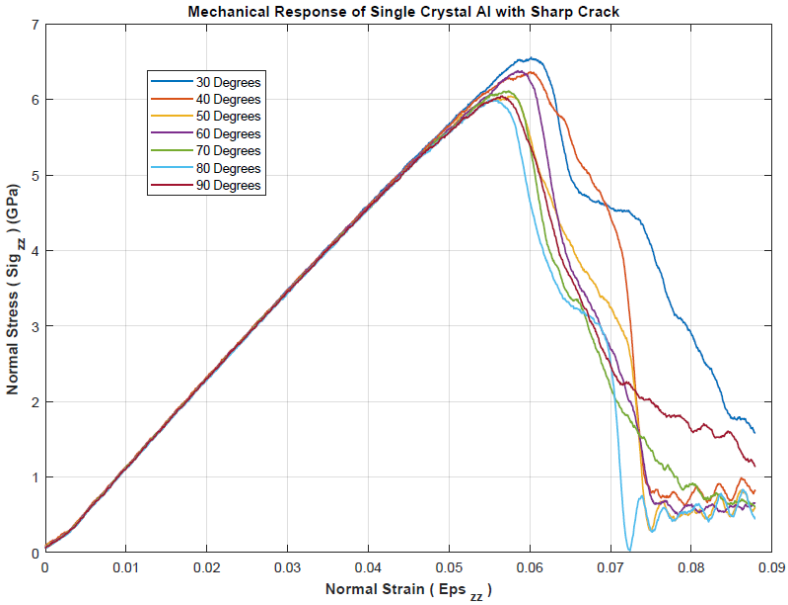

Figure 4-4: Mechanical response of single crystal Al with sharp crack at different orientation

As one can see from both stress-strain curves and MD visualized results that, a system with blunt crack has lower strength than that of the sharp crack but more plastic region than sharp crack. Also, blunt crack propagated more in void growth manner whereas sharp crack displayed cleavage fracture. From this observation, one can also conclude that, due to higher plasticity and void growth type propagation, the stiffness of the blunt crack system degrades way slower compared to sharp crack during crack propagation. As the stress obtained from MD simulations are for whole simulation box, the stresses are volume normalized by volume of the system under inspection before plotting.

4.1.2 Maximum Tensile Stress (MS) criterion results

As discussed earlier, Maximum Tensile Stress criterion is used to analytically obtain crack propagation angle in the considered system in the present study. The criterion

postulates (1) at the crack tip where the circumferential stress ($\sigma_{\theta\theta}$) becomes maximum with respect to θ the crack will extend in that direction, and (2) once $(\sigma_{\theta\theta})_{\max}$ is reached to the value of stress responsible for Mode-I fracture which is $(\sigma_{\theta\theta})_{max} = \frac{K_{Ic}}{\sqrt{2\pi r}}$., the fracture will happen

fracture criterion satisfied by K_I and K_{II} is given by,

$$K_I \cos^2\frac{\theta_0}{2} - \frac{3}{2}K_{II}\sin\theta_0 = \frac{K_{Ic}}{\cos\frac{\theta_0}{2}} \tag{4.1.1}$$

Where,

$$K_I = \sigma_0\sqrt{\pi a}\sin^2\beta$$

$$K_{II} = \sigma_0\sqrt{\pi a}\sin\beta\cos\beta$$

$$K_{Ic} = \sigma_{max}\sqrt{2\pi a} \tag{4.1.2}$$

And 'σ_0' is remotely applied uniaxial normal far from crack surface, '$2a$' is total crack length and 'β' is crack inclination angle from direction of applied normal stress.

But before applying this criterion, one must check for the crystal anisotropy of the considered material system. Despite being isotropic in behavior from the macro scale, materials may behave differently from lattice perspective. For example, all crystals with cubic unit cell have some amount of anisotropy at lattice level. Now, as known, there are three independent elastic constants in cubic lattice system which are C11, C12 and C44 compared to most of the polycrystalline aggregates which have two independent constants as C44 is related to C11 and C12, and stiffness matrix of such isotropic system can be represented as,

$$\begin{bmatrix} C11 & C12 & C12 & 0 & 0 & 0 \\ C12 & C11 & C12 & 0 & 0 & 0 \\ C12 & C12 & C11 & 0 & 0 & 0 \\ 0 & 0 & 0 & \frac{C11-C12}{2} & 0 & 0 \\ 0 & 0 & 0 & 0 & \frac{C11-C12}{2} & 0 \\ 0 & 0 & 0 & 0 & 0 & \frac{C11-C12}{2} \end{bmatrix}$$

But, such stiffness matrix, does not apply to cubic crystal materials, and anisotropy ratio needs to be introduced, which is often regarded as Zener number as given below.

$$A = \frac{2\,C44}{C11 - C12} \tag{4.1.3}$$

The near the ratio to value '1', the more isotropic system will be at crystal level. Hence, to obtain the ratio for Al, in this case, a perfect crystal of Al (i.e., without any defect) with similar dimensions as considered for crack propagation simulations were loaded in (1) Tension to obtain C11 and C12 and (2) Shear to obtain C44. The obtained Stress-strain curves are represented in figure 4-5 and 4-6 below. Strain in Z direction due to applied loading in the Z direction is plotted whose slope gives C11, whereas slope of mechanical strain in Z direction due to applied loading in X direction gives C12 from the tensile loading. From the slopes, C11 is achieved to be 116.5 GPa, C12 is achieved to be 65.6 GPa, and C44 is found 24 GPa rendering Zener number A,

$$A = \frac{2 \times 24}{116.5 - 65.6} = 0.9430$$

Hence, one can say that cubic crystal of Aluminum is close to an isotropic system and above presented equation 4.1.1 and 4.1.2 for Maximum Tensile Stress criterion can be applied safely to the crack propagation analysis in single crystal Al.

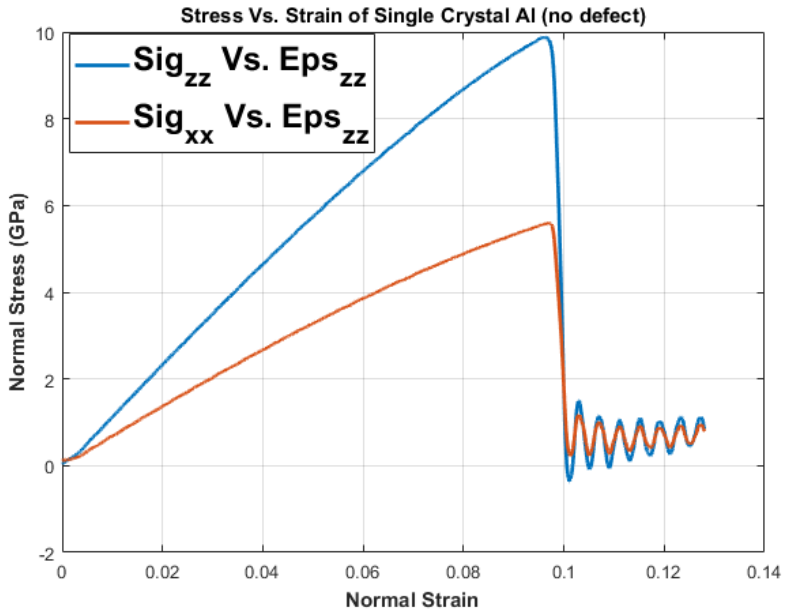

Figure 4-5: Single crystal Al tensile test (volume normalized stresses)

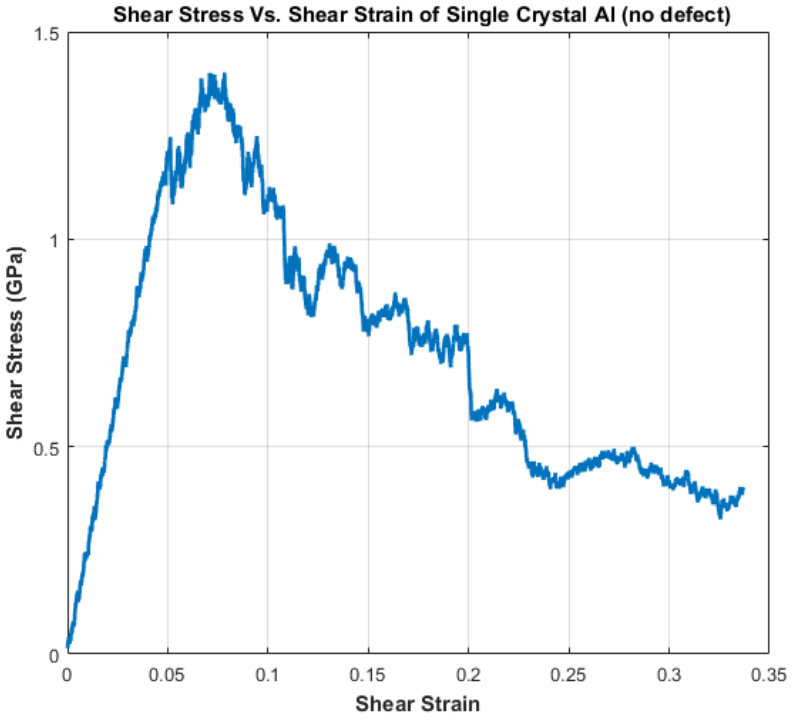

Figure 4-6: Single crystal Al shear test (volume normalized stresses)

Apart from this, the solution of maximum tensile stress criterion for crack propagation is derived for stress applied infinitely far from the defect (i.e., crack) in the materials system. As one cannot simulate the infinitely large system, the dimensions in this study are chosen in a manner that length dimensions of the system are much larger than crack length, but the system is loaded by a constant increment in the Z dimension. This does not provide any idea about remote stresses into the system. Hence, based on the failure strains for all the systems as reported in previous results from MD simulations, corresponding remote critical stress. 'σ_{Cr}' in the case of 90° crack and stress 'σ_0' in the case of cracks at other orientations are obtained by averaging the local virial stress within the layer of 5 unit cells underneath the fixed layers (i.e. layers where displacement is applied). This was achieved by stress/atom function in LAMMPS code. The obtained values were in ($pressure \times volume$) units, which was further converted into pressure units (GPa) by multiplying with atomic volume and subsequently averaging values from all the atom present in the layer of 5-unit cells underneath the fixed layers. This, assumption is common for all other system under study (i.e. SiC and ZrB_2).

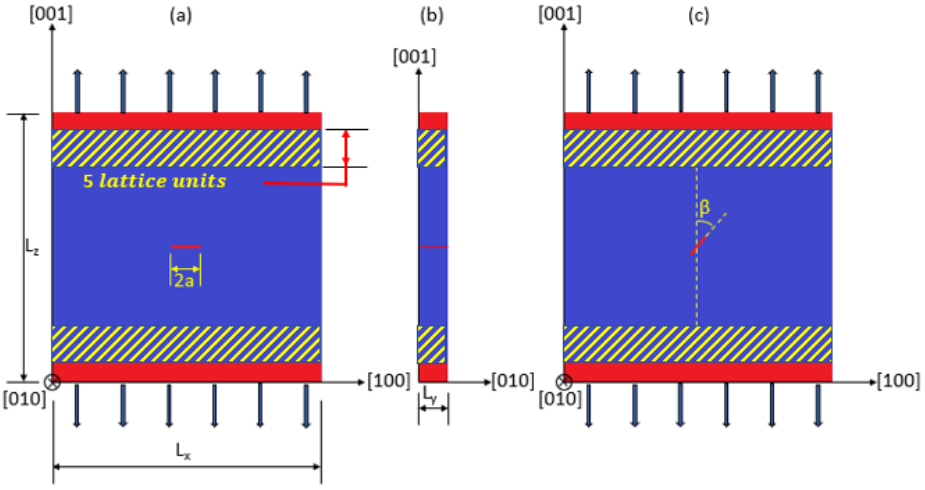

Figure 4-7: Stripped region indicates region considered to evaluate remote stress by averaging atomic stresses, in all the models (Al, SiC, and ZrB_2)

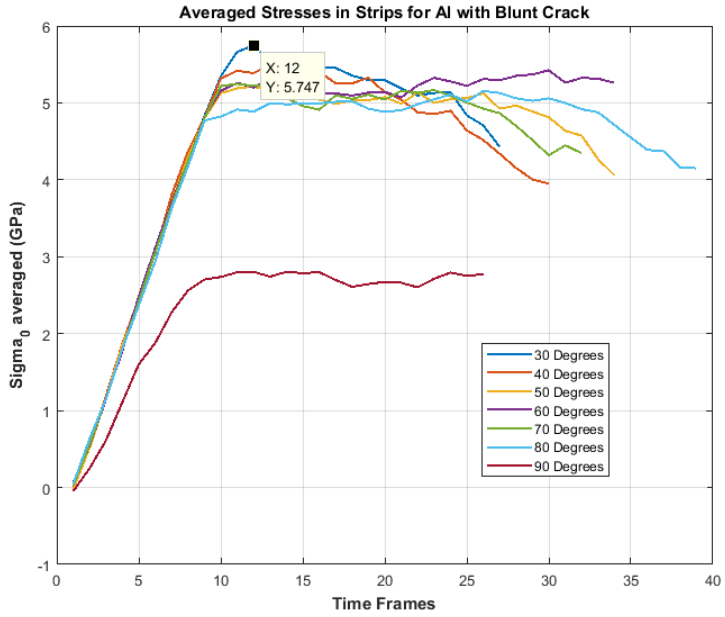

Figure 4-8: Remote stress by averaged atomic stresses in Al with blunt crack (The peak value, in above graph, represents stress (σ_0) at failure strain for corresponding model.)

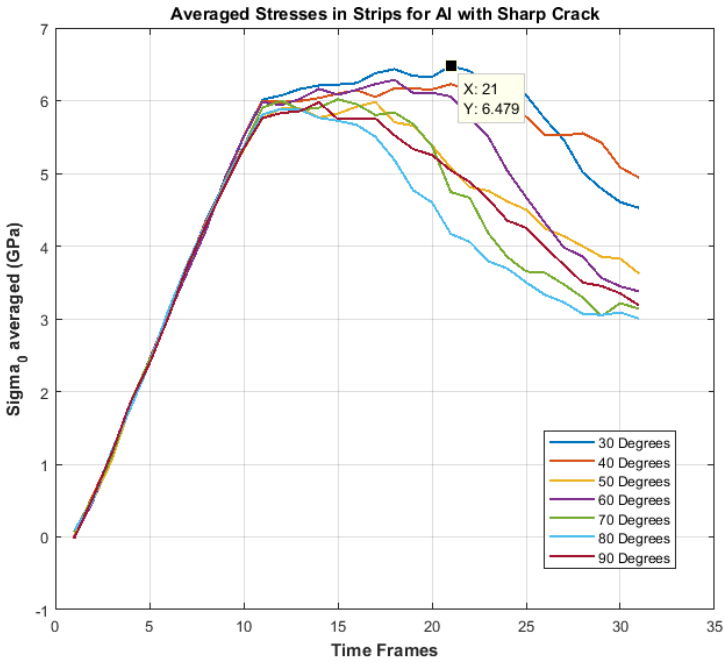

Figure 4-9: Remote stress by averaged atomic stresses in Al with blunt crack (The peak value, in above graph, represents stress 'σ_0' at failure strain for corresponding model.)

The peak value in above graphs corresponds to 'σ_0' at failure strain for corresponding model and by plotting these stresses one can conclude that as soon as model reaches to failure strain far field stress drops quickly, symbolizing release of large amount of strain energy. This is represented in below figures.

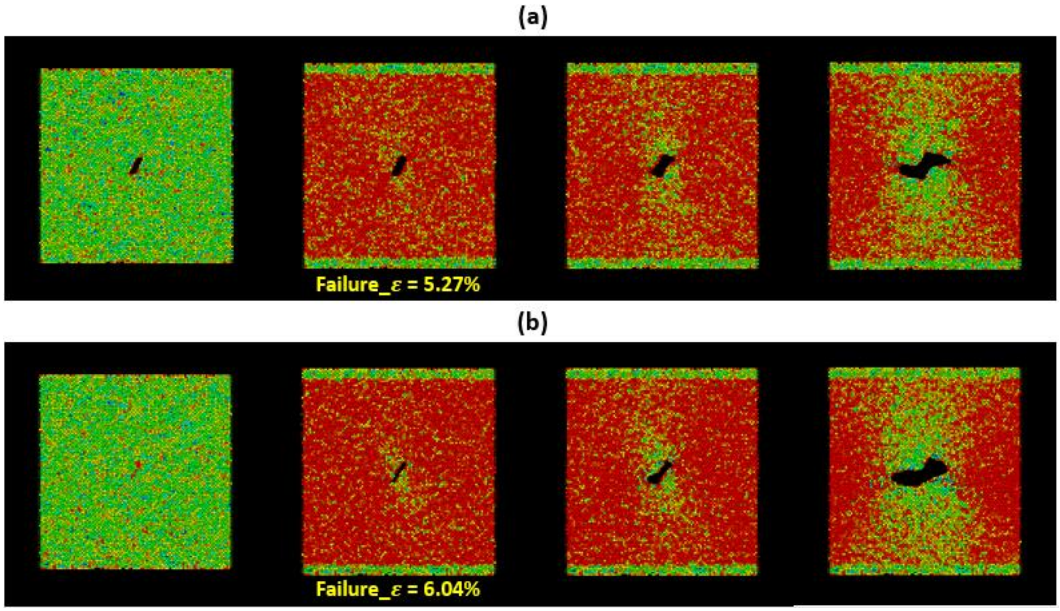

Figure 4-10: Per atom stress in Z direction (a) Blunt crack (b) Sharp crack (After failure strain stress into system is released)

Once, the values of critical far-field stresses 'σ_0' are obtained they are used to evaluate values of mode-I, mode-II and critical stress intensity factors by equations 4.1.2. And as mentioned above crack propagation angles can be now obtained by minimizing Equation 4.1.1. The crack propagation angles obtained through MD simulations were measure with the help of imageJ code [176]. The table below shows summary of the results obtained for crack propagation under mixed mode loading in Al single crystal.

Table 4-1-1: Summary of propagation of Sharp Crack under mixed mode loading in Al single crystal

	β (Sharp Crack, Orientation from Loading)	MD Simulation (Al Sharp Crack)					MS-criterion
		θ_L(in Degrees)	θ_R(in Degrees)	K_{Ic} (Pa $m^{1/2}$)	K_I (Pa $m^{1/2}$)	K_{II} (Pa $m^{1/2}$)	θ (in Degrees)
Al Sharp Crack	30°	-59.128	-58.736	474012.974	90832.2273	157326.0327	-60.27
	40°	-52.601	-53.827		144279.9006	171946.0898	-55.668
	50°	-47.865	-50.468		196789.1239	165125.6813	-50.511
	60°	-36.674	-34.281		264379.4015	152639.5186	-43.2
	70°	-16.772	-17.130		298049.1937	108481.0349	-33.323
	80°	-8.807	-8.25		319795.4049	56465.27731	-18.999
	90°	0	45.591		K_{Ic}	-	0

Table 4-1-2: Summary of propagation of Blunt Crack under mixed mode loading in Al single crystal

	β (Blunt Crack, Orientation from Loading)	MD Simulation (Al Blunt Crack)					MS-criterion
		θ_L(in Degrees)	θ_R(in Degrees)	K_{Ic} (Pa $m^{1/2}$)	K_I (Pa $m^{1/2}$)	K_{II} (Pa $m^{1/2}$)	θ (in Degrees)
Al Blunt Crack	30°	-59.601	-62.365	223610.933	80931.35824	140177.2244	-60.160
	40°	-58.316	-49.611		127983.6042	152524.9201	-55.63
	50°	-42.086	-48.616		172318.2523	144592.182	-50.306
	60°	-33.23	-32.652		229190.509	132323.2021	-43.201
	70°	-17.6	-18.052		261036.4067	95009.48209	-33.288
	80°	-12.467	-13.348		281567.7792	49647.99636	-18.907
	90°	0	0		K_{Ic}	-	0

4.2 : Mixed mode fracture analysis in Silicon Carbide

4.2.1 Molecular dynamics simulation results

An atomistic system of single crystal SiC with dimensions mentioned in Table 3.4.1 is considered. The material system with blunt crack and sharp crack are represented in the figure 4-11 below, which shows initial configurations of SiC material system.

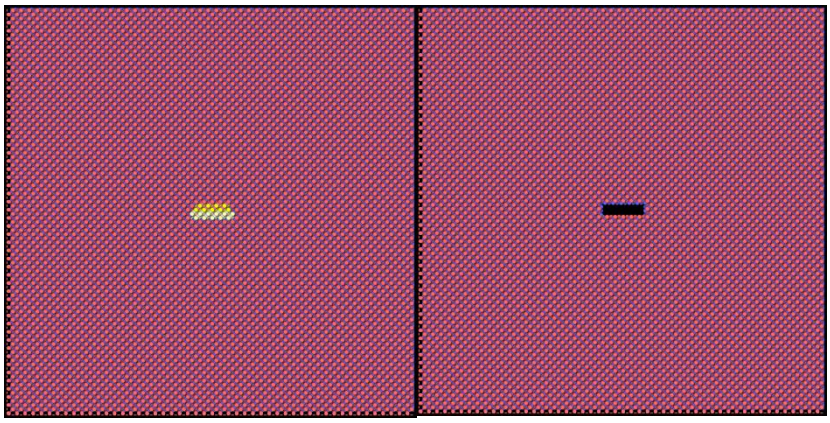

Figure 4-11: Single crystal SiC system with sharp and blunt crack respectively

The initial configuration, configuration after relaxation and configurations before and after crack propagation are reported in the figure 4-12 (Case-1 to Case-7) and 4-13 (Case-1 to Case-7) for blunt crack and sharp crack respectively. As in the case of aluminum, atoms in SiC lattice does not have any centro-symmetry parameter. Hence, one cannot use centro/atom option of lammps to assess the crack propagation. Instead, dislocation analysis [172] has been performed which color codes the atoms as a part of perfect crystal or a dislocated atom. This feature is used with the help of 'The Open Visualization Tool' (OVITO) [175]. All the results showing atomic configurations are plotted with OVITO in this study. As represented in images, the atom colored blue still possesses the perfect cubic diamond structure of SiC whereas, those colored red are dislocated atoms from the perfect cubic diamond structure. As one can see, such atoms are around blunt crack and near boundaries where while loading the structure the atoms are no longer in

contact with its periodic image cell. In figure 4-12, all the images after initial relaxation (i.e., all images marked as '(b)') does not show dislocated atoms near the presence of crack as to create the sharp crack effect, the interaction between some layer of atoms are turned off which means atoms are still in the cubic diamond crystal structure but they do not interact with each other. Unlike aluminum, SiC crystal does not undergo significant change while relaxation, rendering crack atoms unable to show up in dislocation analysis in the case of a sharp crack. Once crack opens, dislocated atoms are again marked red with dislocation analysis parameter automatically.

Presented below, are MD results of crack propagation under mixed mode loading in single crystal SiC with blunt crack,

Case – 1, β=30°

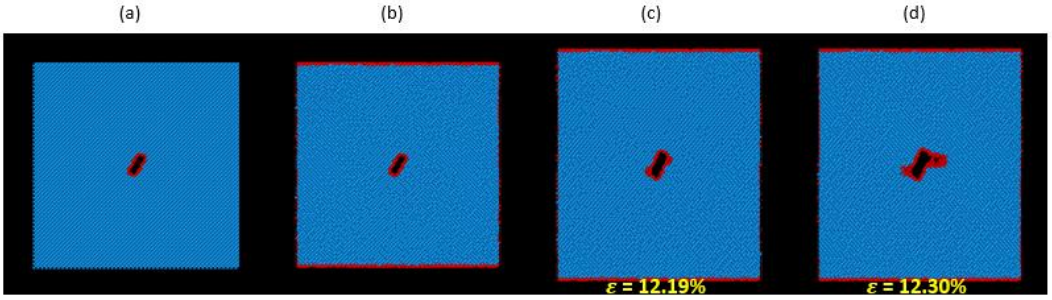

Case – 2, β=40°

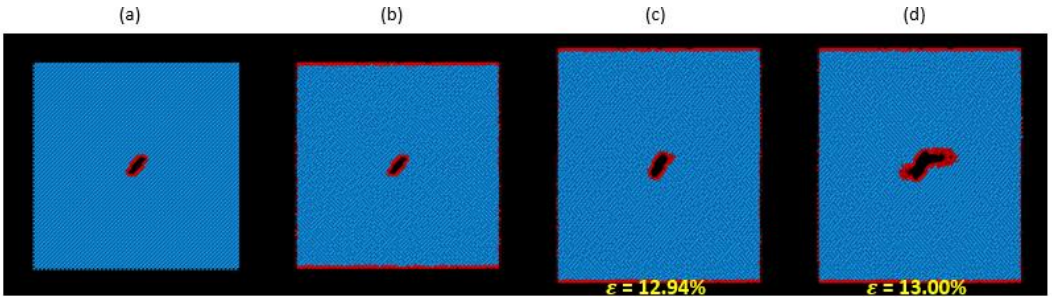

Case – 3, β=50°

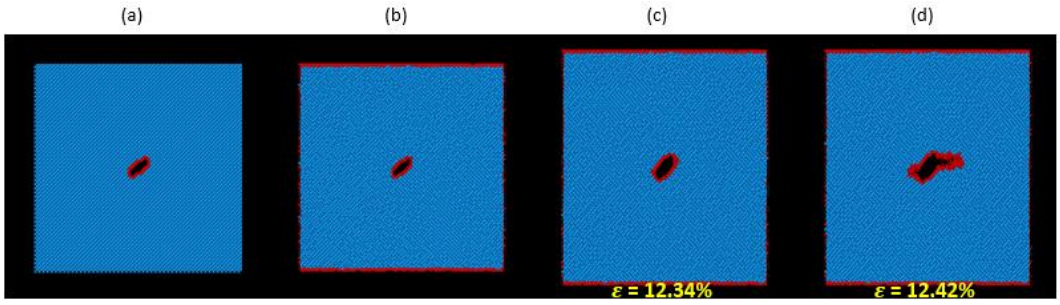

Case – 4, β=60°

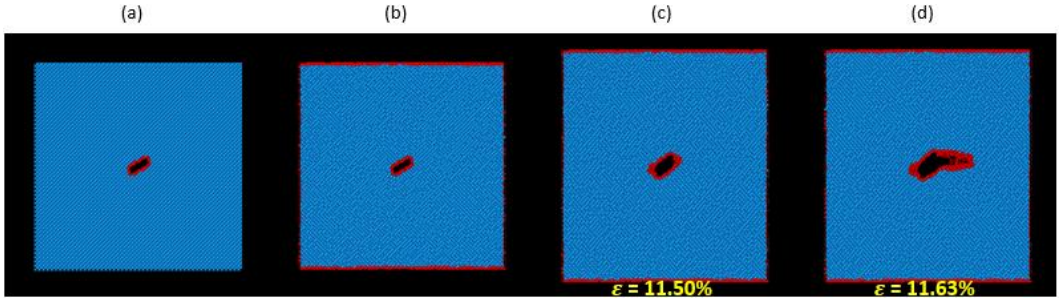

Case – 5, β=70°

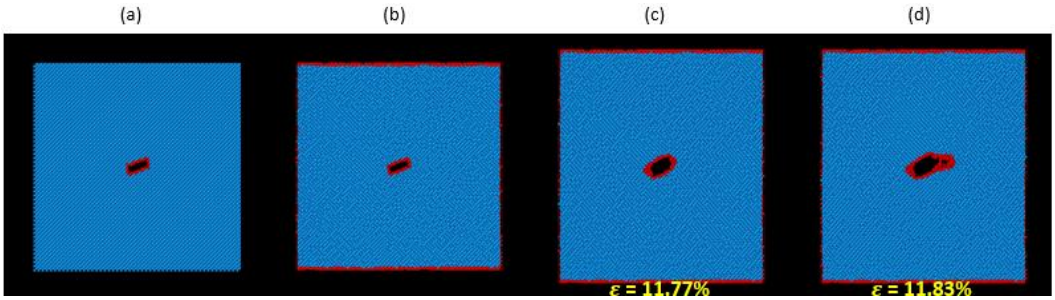

Case – 6, β=80°

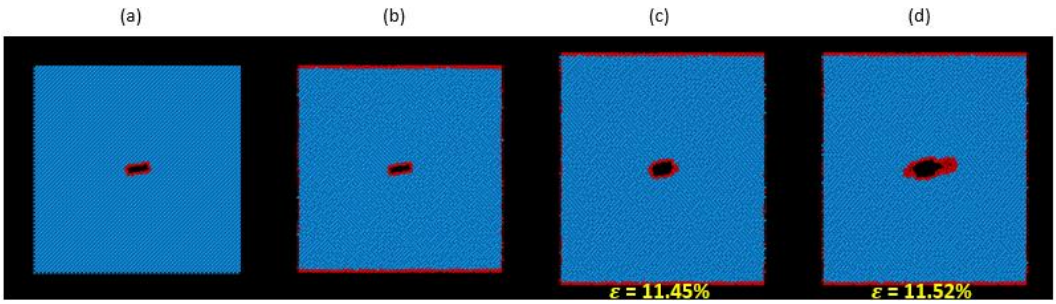

Case – 7, β=90°

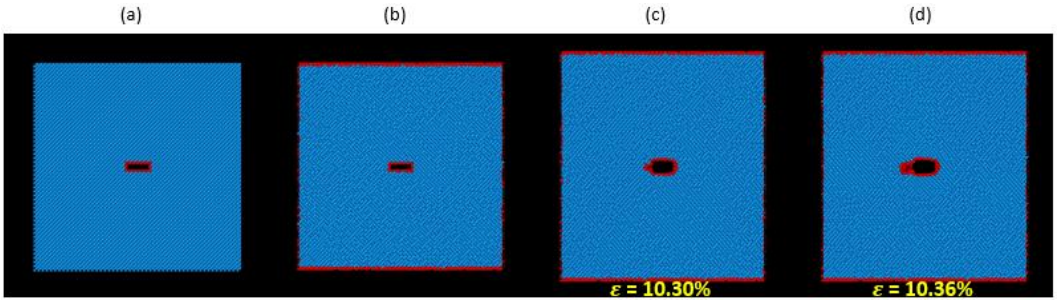

Figure 4-12: MD simulation results for inclined blunt crack in SiC, oriented at β=30°(case-1) to β=90°(case-7), (a) Initial Configuration (b) System after relaxation (c) Strained system just before crack propagation (d) System when crack propagates; (case-1 to case-7)

Following are the results for sharp crack with different orientations in SiC.

Case – 1, β=30°

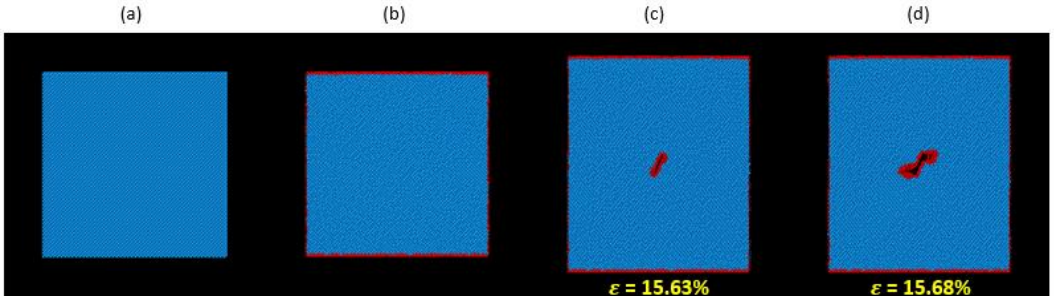

Case – 2, β=40°

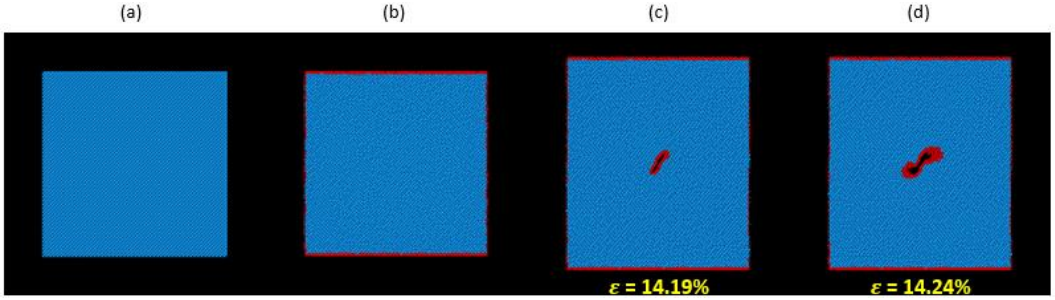

Case – 3, β=50°

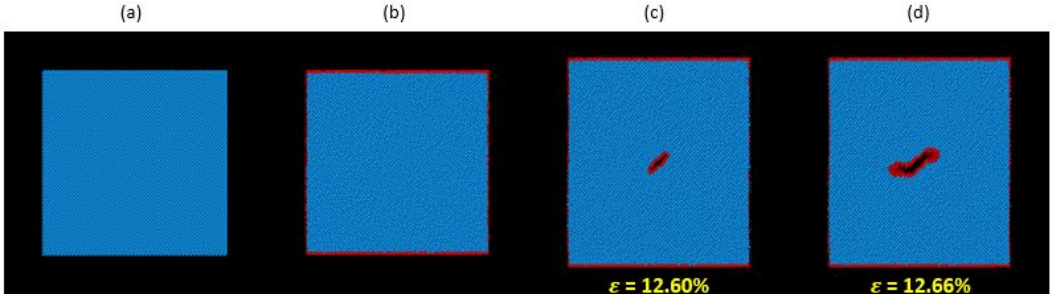

Case – 4, β=60°

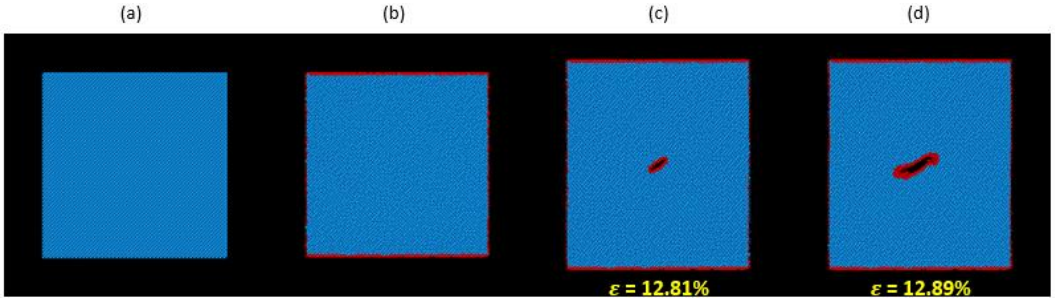

Case – 5, β=70°

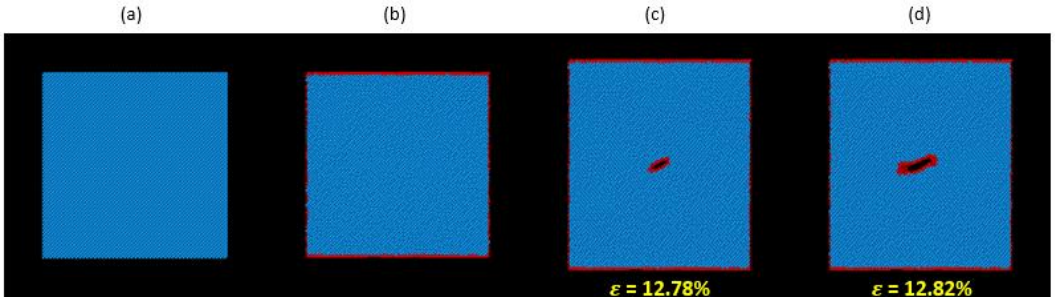

Case – 6, β=80°

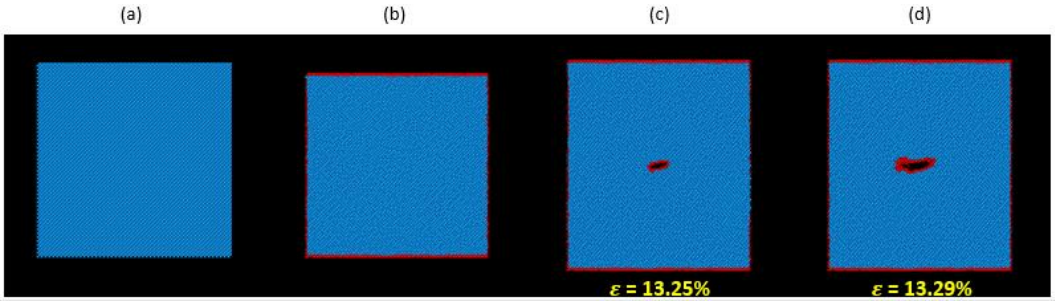

Case – 7, β=90°

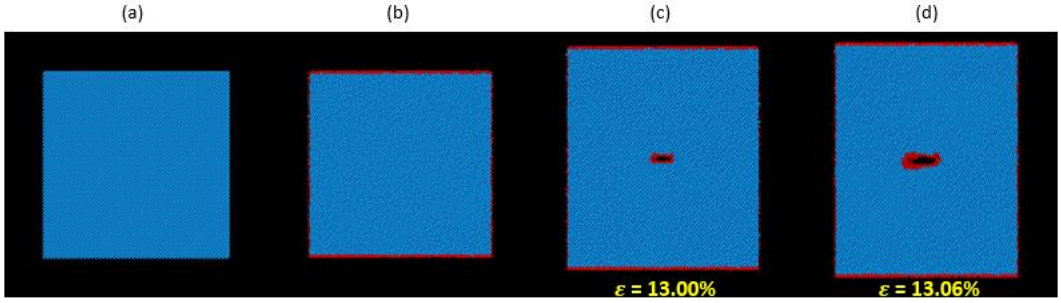

Figure 4-13: MD simulation results for inclined sharp crack in SiC, oriented at β=30°(case-1) to β=90°(case-7), (a) Initial Configuration (b) System after relaxation (c) Strained system just before crack propagation (d) System when crack propagates; (case-1 to case-7)

Given below are the mechanical responses of the systems with the different crack orientation of blunt and sharp crack respectively. With the figures given in figure 4-12 (Case-1 to Case-7) and figure 4-13 (Case-1 to Case-7), Image (c) corresponds to near peak value in the stress-strain curves where crack is about to propagate, and stresses are maximum, whereas, image (d) corresponds to the region after peak stress on stress-strain curves during which crack propagates ultimately rendering system to complete failure (Figure 4-14).

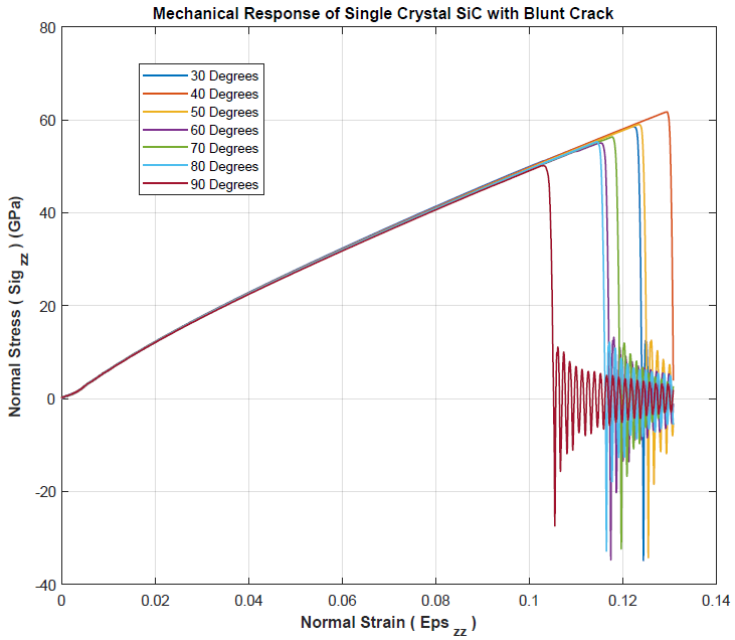

Figure 4-14: Mechanical response of single crystal SiC with blunt crack at different orientation

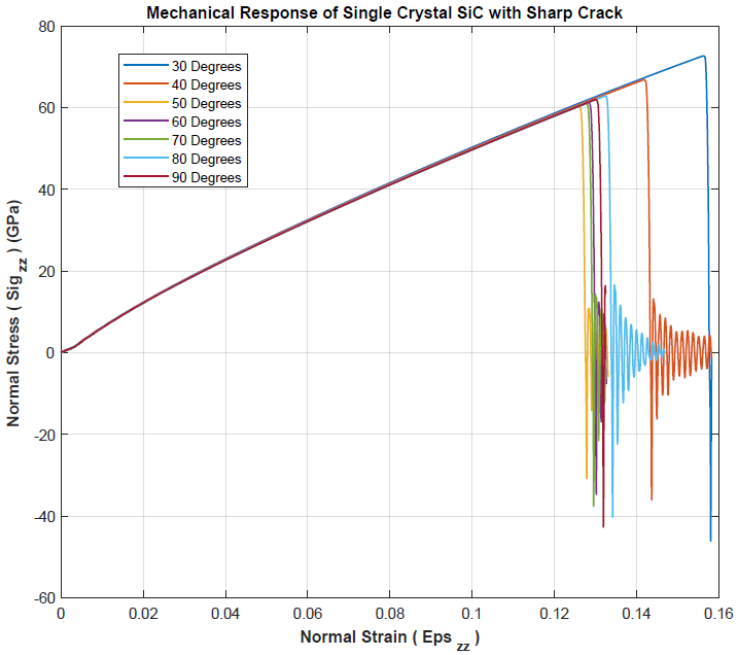

Figure 4-15: Mechanical response of single crystal SiC with blunt crack at different orientation

As one can see from both stress-strain curves and MD visualized results that, a system with blunt crack has lower strength than that of the sharp. As visualized by MD results in significant crack blunting occurs in both the models but a system with initial blunt crack forms more of a void like geometry before the crack propagates. Again, the stress obtained from MD simulations are for whole simulation box. Hence, the stresses are volume normalized by volume of the system under inspection before plotting.

4.2.2 Maximum Stress (MS) criterion results

Similar methodology as explained in 4.1.2 section has been carried out to obtain the analytical solutions by Maximum Stress criterion. The results are then compared with the crack propagation angles obtained by MD simulations as shown in the previous section. Again, a perfect crystal of SiC with the similar dimension as used for crack propagation analysis is used to obtain C11, C12 and C44 elastic constants to check the anisotropy of the cubic diamond lattice structure of pure SiC. Similarly, as earlier, Strain in Z direction due to applied loading in the Z direction is plotted whose slope gives C11, whereas slope of mechanical strain in Z direction due to applied loading in X direction gives C12 from the tensile loading. From the slopes, C11 is achieved to be 506.1 GPa, C12 is achieved to be 130.018 GPa, and C44 is found 250.759 GPa rendering Zener number A,

$$A = \frac{2 \times 250.75}{506.1 - 130.018} = 1.33$$

Which, suggests SiC is anisotropic at the crystal level. But, as far as present work is concerned it will be assumed that SiC crystal has isotropic behavior and crack propagation study will be performed. Effect of anisotropy on crack propagation is planned to be addressed in future work. Figure 4-16 and 4-17 represents the mechanical response of perfect SiC crystal under Tensile and Shear testing.

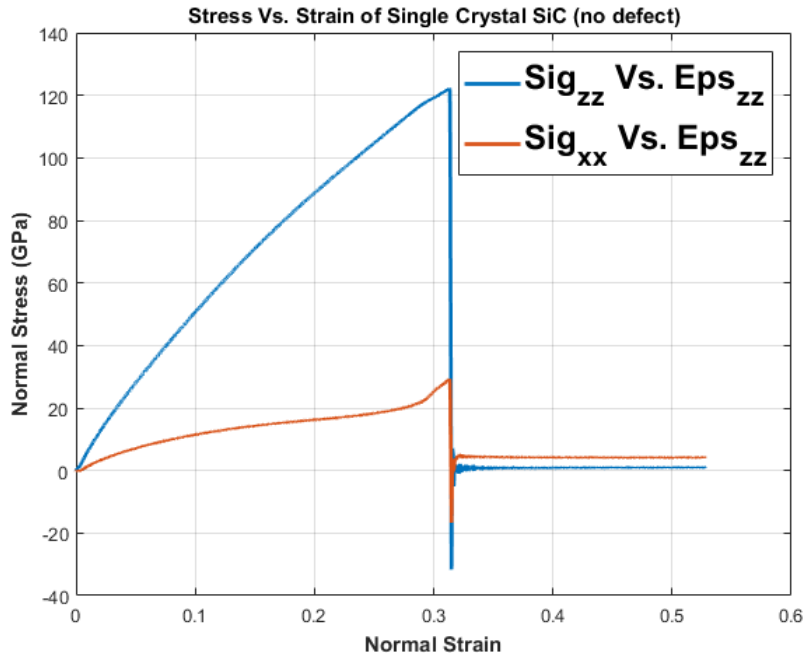

Figure 4-16: Single crystal SiC tensile test (volume normalized stresses)

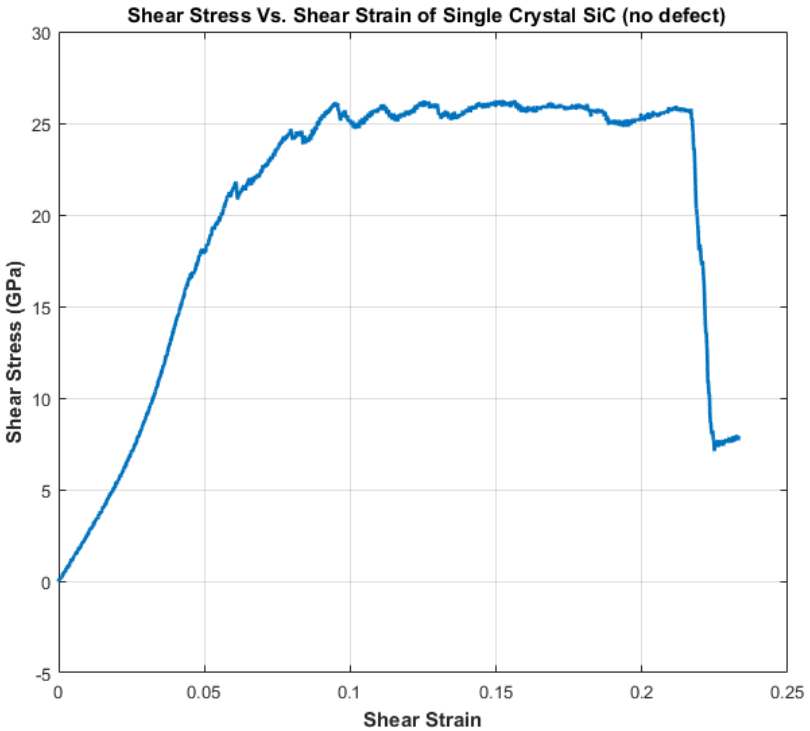

Figure 4-17: Single crystal SiC tensile test (volume normalized stresses)

As mentioned during analysis of Al single crystal, once again average per atom stresses from 5-unit cell worth region underneath the fixed grip is considered as far-field stress in the system for analysis of crack propagation angle. Critical stresses for all the system with differently oriented sharp and blunt cracks are obtained and are plotted in following graphs in Figure 4-18, and 4-19 and peak value corresponds to failure strain of the corresponding system beyond which material fails, and a huge amount of strain energy is released which is also noticeable from figure 4-20.

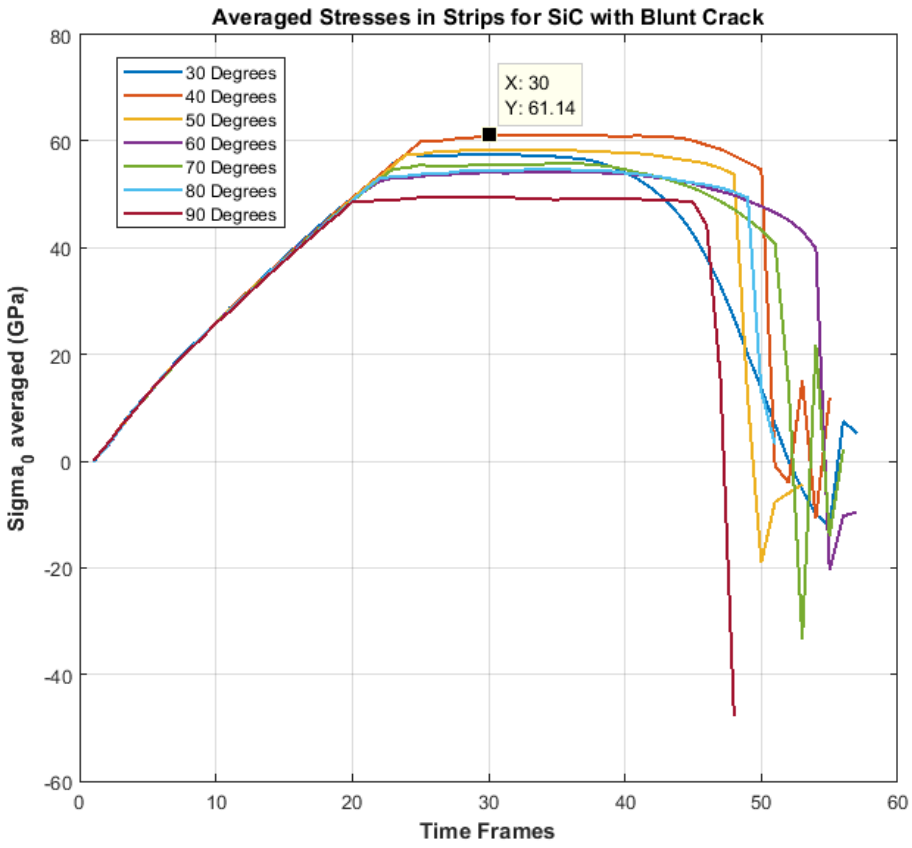

Figure 4-18: Remote stress by averaged atomic stresses in SiC with blunt crack (The peak value, in above graph represents stress 'σ_0' at failure strain for corresponding model)

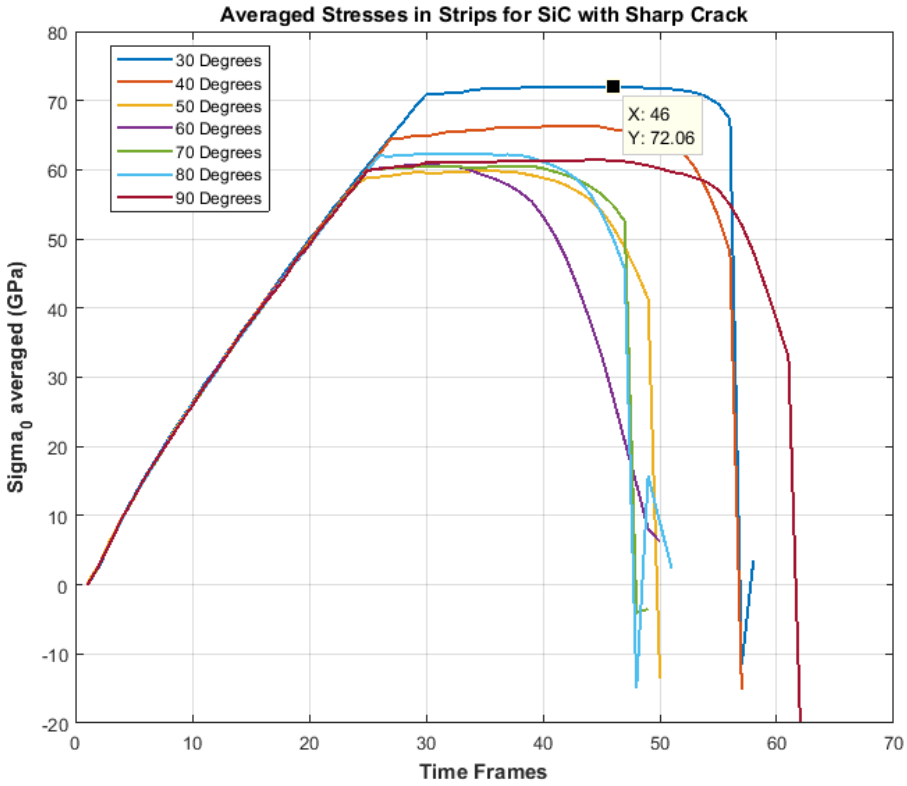

Figure 4-19: Remote stress by averaged atomic stresses in SiC with blunt crack (The peak value, in above graph, represents stress 'σ_0' at failure strain for corresponding model.)

far-field stresses 'σ_0' are obtained from graphs plotted above and mode-I, mode-II and critical stress intensity factors are evaluated by equations 4.1.2. Crack propagation angles is obtained by minimizing Equation 4.1.1. The crack propagation angles obtained through MD simulations were measure with the help of imageJ code [176]. The table 4-1-2 shows summary of the results obtained for crack propagation under mixed mode loading in Al single crystal.

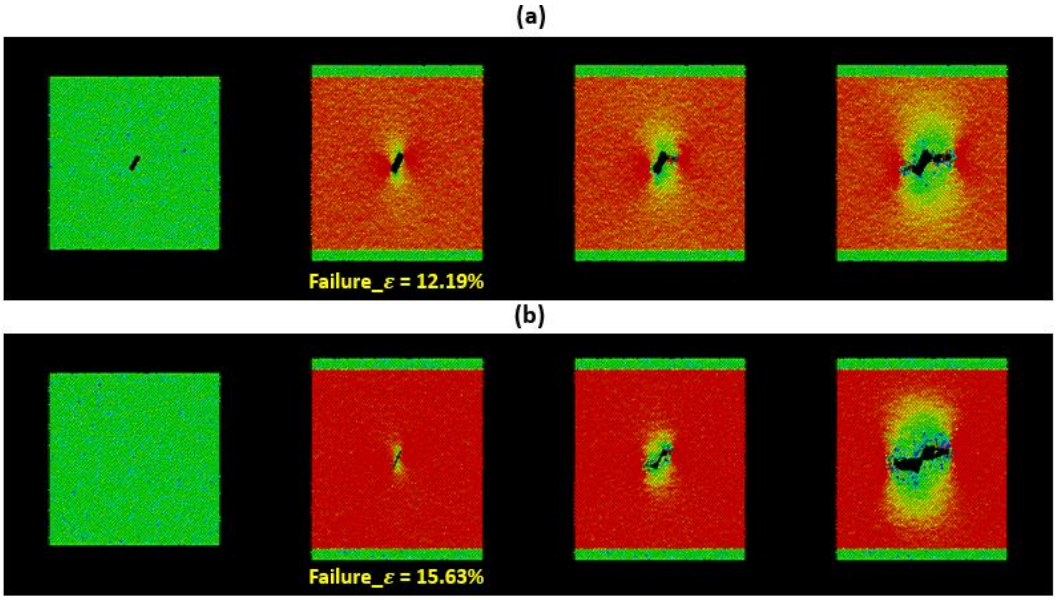

Figure 4-20: Per atom stress in Z direction (a) Blunt crack (b) Sharp crack (After failure strain, stress into system is released)

Table 4-2-1: Summary of propagation of Sharp Crack under mixed mode loading in SiC single crystal

	β (Sharp Crack, Orientation from Loading)	MD Simulation (SiC Sharp Crack)					MS-criterion
		θ_L(in Degrees)	θ_R(in Degrees)	K_{Ic} (Pa m$^{1/2}$)	K_I (Pa m$^{1/2}$)	K_{II} (Pa m$^{1/2}$)	θ (in Degrees)
SiC Sharp Crack	30°	-59.128	-58.736	5082683.566	1054150.282	1825841.846	-60.27
	40°	-54.318	-53.604		1605839.467	1913764.954	-55.668
	50°	-43.567	-48.467		2053761.452	1723310.477	-50.511
	60°	-29.104	-30.855		2663024.108	1537497.686	-43.063
	70°	-19.764	-17.553		3129662.234	1139103.896	-33.32
	80°	-10.421	-10.339		3535568.267	623416.0775	-18.999
	90°	0	0		K_{Ic}	-	0

Table 4-2-2: Summary of propagation of Blunt Crack under mixed mode loading in SiC single crystal

	β (Blunt Crack, Orientation from Loading)	MD Simulation (SiC Blunt Crack)					MS-criterion
		θ_L(in Degrees)	θ_R(in Degrees)	K_{Ic} (Pa $m^{1/2}$)	K_I (Pa $m^{1/2}$)	K_{II} (Pa $m^{1/2}$)	θ (in Degrees)
SiC Blunt Crack	30°	-59.5	-59.204	4104544.202	841008.8772	1456670.105	-60.21
	40°	-49.26	-46.061		1478184.658	1761631.877	-55.62
	50°	-51.871	-37.76		2006374.881	1683548.423	-49.893
	60°	-29.501	-28.836		2383029.154	1375842.524	-43.590
	70°	-17.152	-19.243		2881128.713	1048645.093	-33.27
	80°	-13.699	-7.464		3101424.454	546864.9861	-18.95
	90°	0	-4.3		K_{Ic}	-	0

4.3 : Mixed mode fracture analysis in ZrB_2

4.3.1 Molecular dynamics simulation results

Same as above cases, an atomistic system of single crystal ZrB_2 with dimensions mentioned in Table 3.4.1 is considered. The material system with sharp crack is represented in the figure 4-21 below, which shows initial configurations of the ZrB_2 material system. Atoms in Red color shows fixed atoms, where loading is applied. Atoms in green color show strips used to obtain far-field stresses as required for MS criterion by averaging stresses on these atoms.

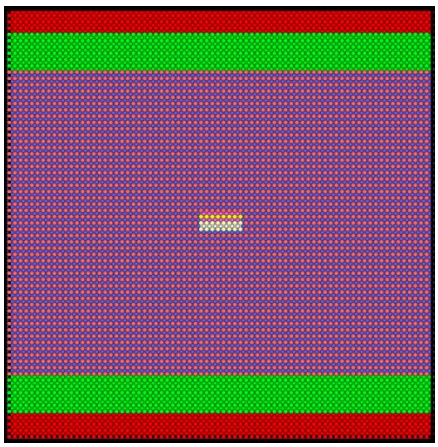

Figure 4-21: Initial configuration of single crystal ZrB_2 system with 90° crack, red-colored atoms represents loading region, and green atoms represents region chosen to obtain far-field stresses

Same as previous sections, the initial configuration, configuration after relaxation and configurations before and after crack propagation are reported in the figure 4-22 (Case-1 to Case-7) for a sharp crack in ZrB_2. As one knows, ZrB_2 has centrosymmetric structure, but being unknown to the actual centro-symmetry number of the system, centro-symmetry number 18 was selected which gave a noticeable visualization of crack

propagation in the system configurations plotted below. Again, OVITO [175] code was used to visualize these configurations presented here.

Presented below, are MD results of crack propagation under mixed mode loading in single crystal ZrB_2 with sharp crack,

Case – 1, β=30°

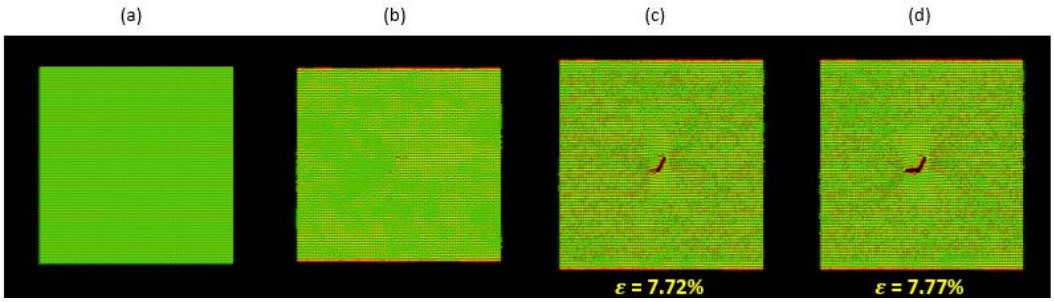

Case – 2, β=40°

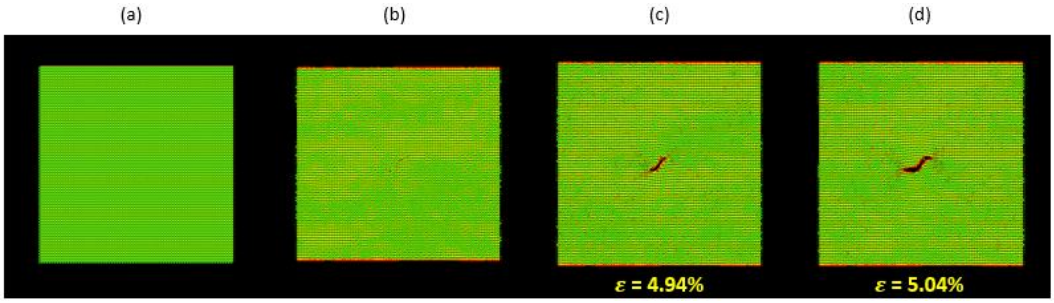

Case – 3, β=50°

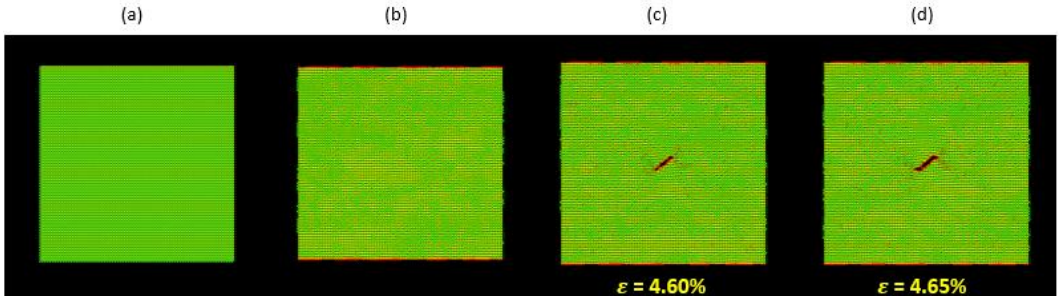

Case – 4, β=60°

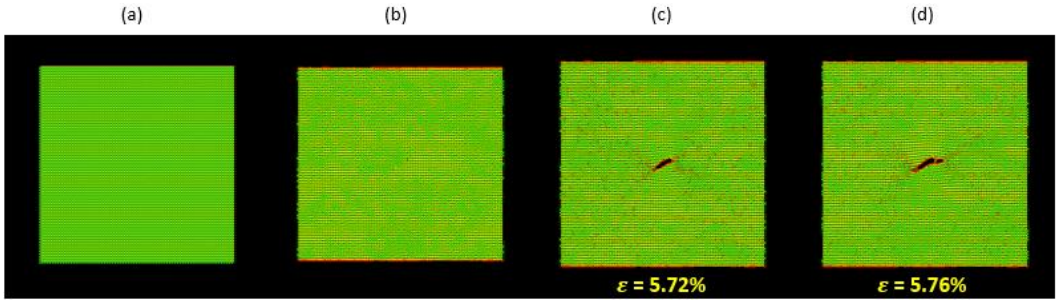

Case – 5, β=70°

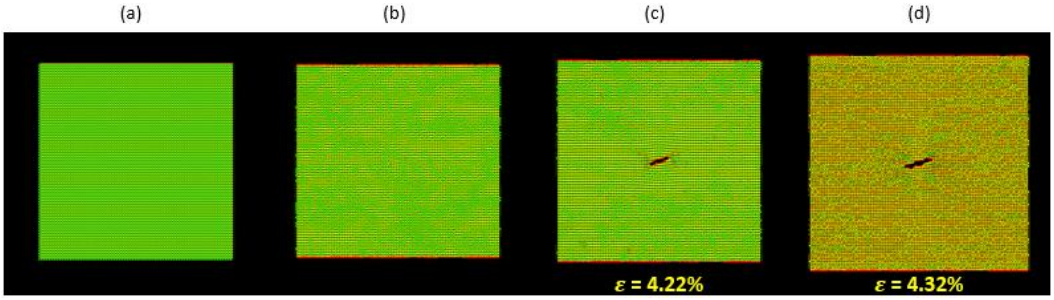

Case – 6, β=80°

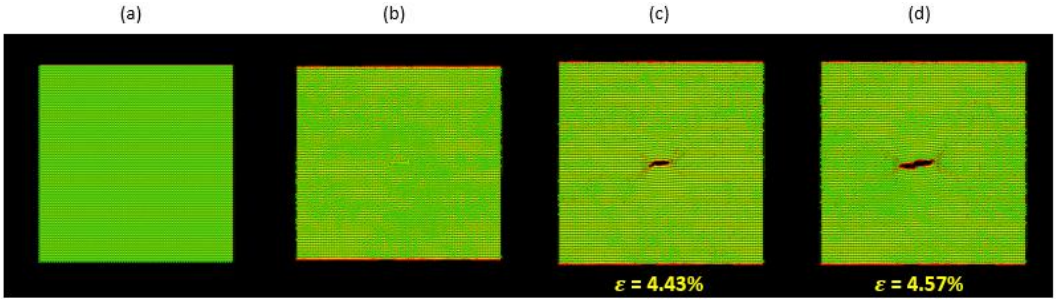

Case – 7, β=90°

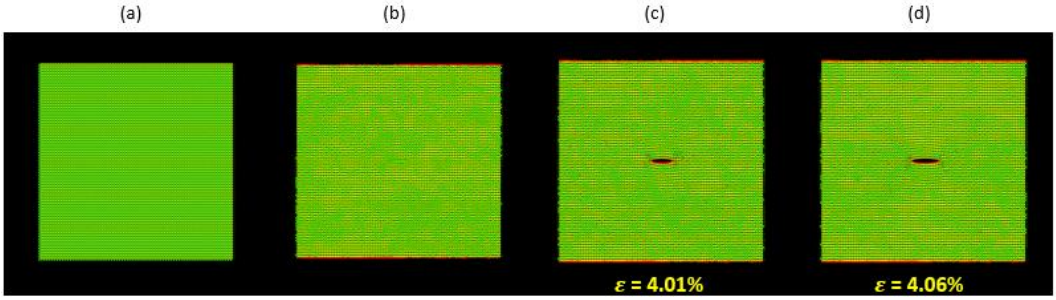

Figure 4-22: MD simulation results for inclined sharp crack in ZrB_2, oriented at β=30°(case-1) to β=90°(case-7), (a) Initial Configuration (b) System after relaxation (c) Strained system just before crack propagation (d) System when crack propagates; (case-1 to case-7)

Given below are the mechanical responses of the systems with the different crack orientation of sharp crack in single crystal ZrB_2. With the figures given in figure 4-22 (Case-1 to Case-7), Image (c) corresponds to near peak value in the stress-strain curves where crack is about to propagate, and stresses are maximum, whereas, image (d) corresponds to the region after peak stress on stress-strain curves during which crack propagates ultimately rendering system to complete failure.

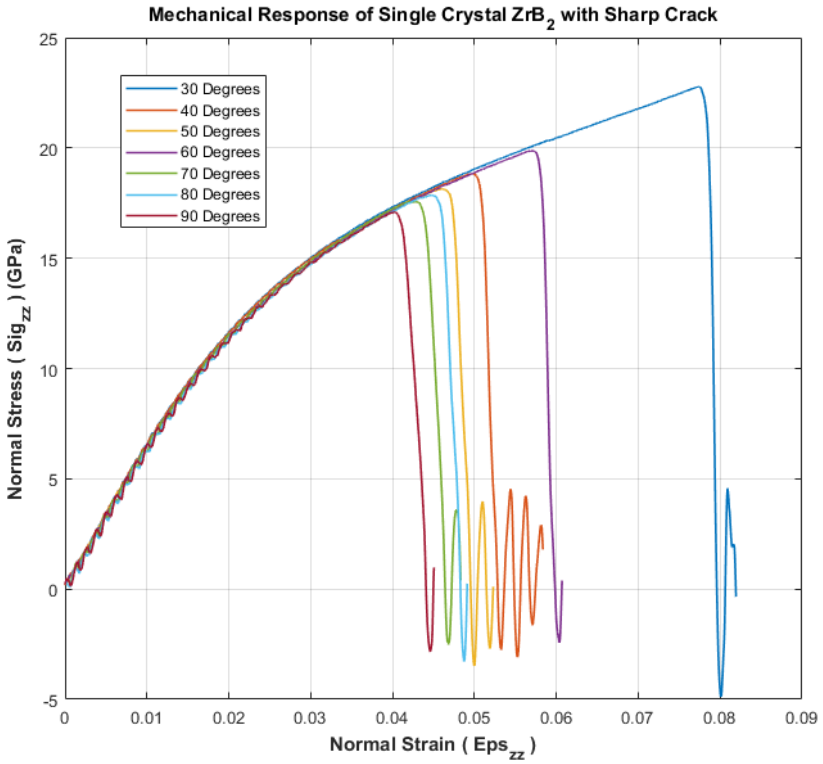

Figure 4-23: Mechanical response of single crystal ZrB_2 with sharp crack at different orientation

4.3.2 Maximum Stress (MS) criterion results

Firstly, the mechanical response of single crystal ZrB_2[0001], loaded in the Z direction is displayed in figure 4-24. Figure4-24(a) corresponds to tensile test whereas 4-24(b) displays shear response of the system.

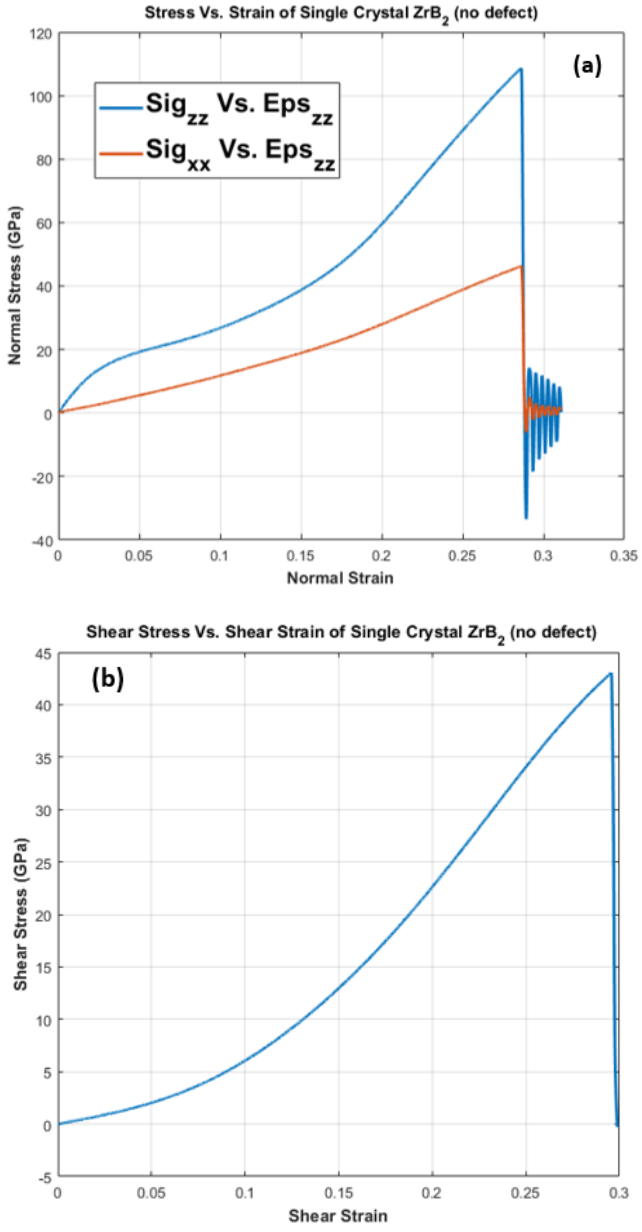

Figure 4-24: Mechanical response of single crystal ZrB_2 (a) Tensile test (b) Shear test

Unlike earlier cases, 6-unit cell worth region underneath the fixed grip is considered to obtain average per atom stresses, which are considered as required far-field stress in the system for analysis of crack propagation angle. 6-unit cells instead of 5-unit cells in the case of Al and SiC are taken owing to the difference in lattice constant of the materials. Critical stresses for all the system with differently oriented sharp and blunt cracks are obtained and are plotted in following graphs in Figure 4-25, and peak value corresponds to failure strain of the corresponding system beyond which material fails, and huge amount of strain energy is released which is also noticeable from figure 4-26.

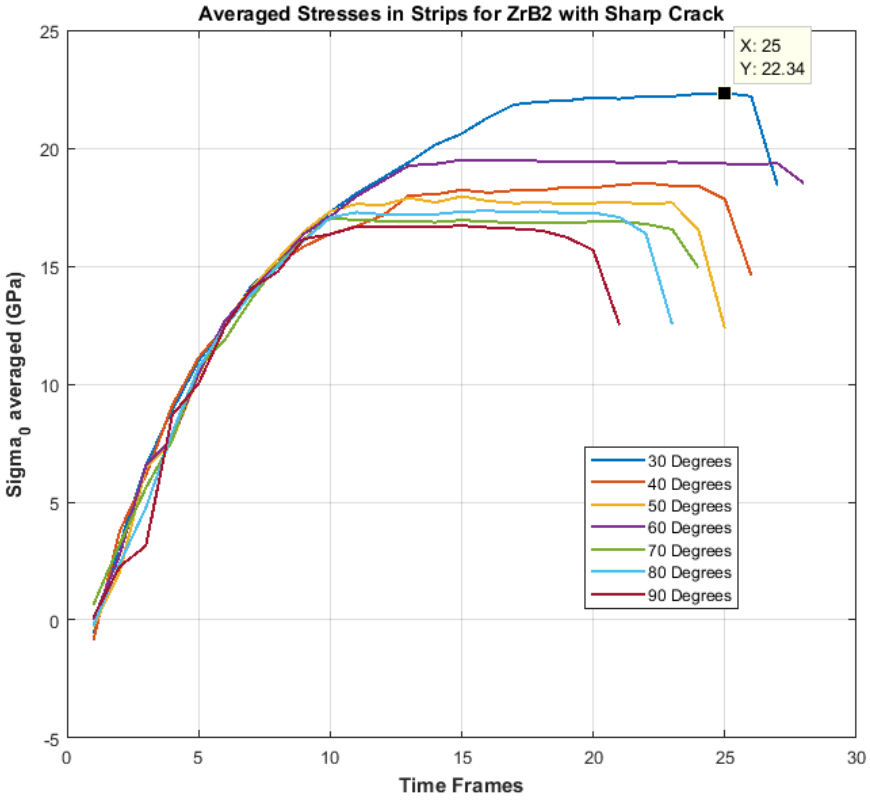

Figure 4-25: Remote stress by averaged atomic stresses in ZrB_2 with sharp crack (The peak value, in above graph, represents stress 'σ_0' at failure strain for corresponding model.)

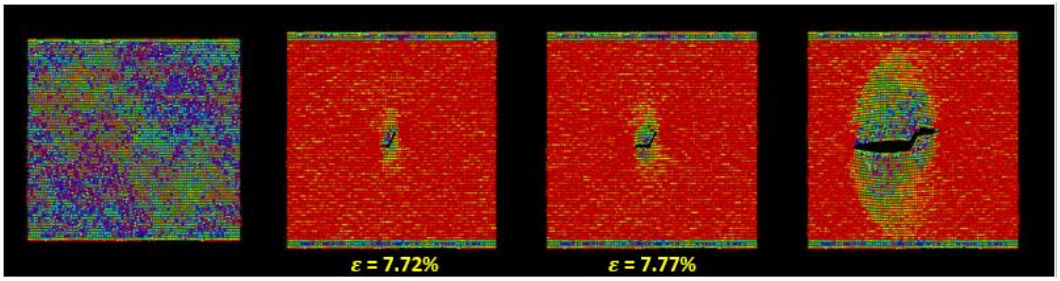

Figure 4-26: Per atom stress in loading direction in ZrB_2 with Sharp crack (once system reaches failure strain, stress into system is released as visible from last two images)

The values of mode-I and mode-II stress intensity factors are obtained using equations in 4.1.2, and corresponding crack propagation angle is found by minimizing equation 4.1.1. The obtained values are reported in Table 4-3-1 below along with propagation angles obtained by MD simulations.

Table 4-3-1: Summary of propagation of Sharp Crack under mixed mode loading in ZrB_2 single crystal

	β (Sharp Crack, Orientation from Loading)	MD Simulation (ZrB_2 Sharp Crack)					MS-criterion
		θ_L(in Degrees)	θ_R(in Degrees)	K_{Ic} (Pa $m^{1/2}$)	K_I (Pa $m^{1/2}$)	K_{II} (Pa $m^{1/2}$)	θ (in Degrees)
ZrB_2 Sharp Crack	30°	-59.421	-59.216	1443920.019	341251.7343	591065.342	-60.160
	40°	-53.976	-53.967		467802.0306	557504.7506	-55.63
	50°	-46.537	-49.268		643611.9155	540054.5209	-50.30
	60°	-31.430	-35.642		894067.3237	516190.01	-43.20
	70°	-16.004	-21.092		919375.4722	334625.306	-33.288
	80°	-4.260	-10.761		1028144.335	181289.5863	-18.90
	90°	0	0		K_{Ic}	-	0

4.4 : Mechanical behavior of ZrB_2/SiC core-shell structure

As shown in Figure 3-12, core-shell type of morphology is designed computationally using molecular dynamics. As discussed in section 3.2.2 and 3.2.3, different interatomic potential functions are adopted to model interaction at the interface of ZrB_2 and SiC. The figure 4-27 below shows the mechanical response of the designed system.

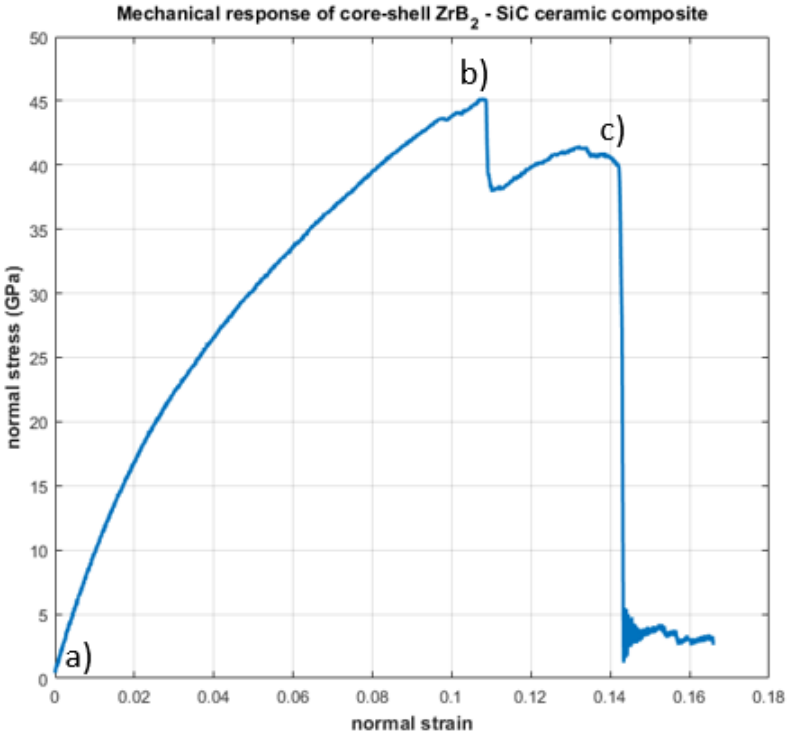

Figure 4-27: Mechanical response of ZrB_2-SiC core-shell structure

In the figure above, point a) belongs to a relaxed system where no loading is applied. As mentioned in section 3.4.2, system is loaded with displacement (Δu_z) of 0.02 Å over 1 ps under NVE ensemble in Z direction with timestep of 1fs. Point b) corresponds to peak stress into the system where system fails at interface between ZrB_2 and SiC. This

failure at interface can be seen as a crack growing inside the system which is arrested by outer layer (i.e. shell structure made of SiC), which can be noticed in Figure 2-28(c). Compared to pure ZrB_2 or SiC single crystal system, the strength of the composite is found to be much lower which can be attributed to higher surface area of interface between constituent materials, which is certainly weaker than individual material. But, owing to more number of interfaces it might lead to increased fracture toughness of the whole system compared to their constituent materials, which needs to be analyzed and is referenced to future work. Figure 2-28 below shows failure in considered core-shell model.

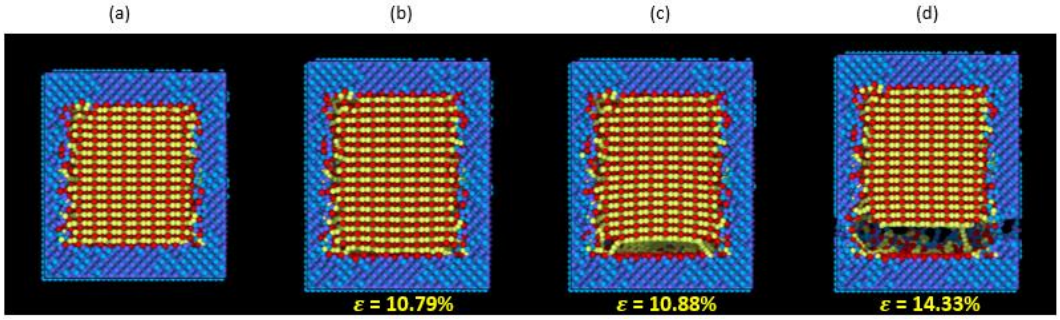

Figure 4-28: Failure in ZrB_2-SiC core-shell structure (a) relaxed system, (b) Maximum strain before failure, (c) Interface separation and (d) complete failure

Chapter 5 Summary and Conclusions

The major objectives of current study are, (1) to study crack propagation in mixed mode loading in different material system, (2) to assess the effect of crack geometry on crack growth, (3) use molecular dynamics simulations as dynamic approach to identify as well as quantify the crack propagation mechanisms in single crystal Al, SiC and ZrB_2, and to validate it against experiments and theoretical solutions and (4) use obtained crack growth behavior as general approach to computational design of morphology in ceramic composites (i.e., ZrB_2/SiC).

A number of requirements needed by future super strong and ultra-high temperature ceramic materials were discussed along with possible additives, processing techniques, and grain morphologies. As the mechanical performance of such materials is of prime interest, the importance of fracture mechanics and fracture mechanics at atomic level was discussed along with different failure criterions for mixed mode crack propagation.

The general approach and motivation for using molecular dynamics as a bridging tool between theory and experiments were discussed. The basic numerical algorithm which facilitates molecular dynamics simulation along with interatomic potential function and time integrator scheme was discussed.

The crack propagation under mixed mode loading was analyzed in three different material systems respectively Al, SiC, and ZrB_2 single crystals. Two crack geometry, blunt crack and sharp crack was considered for analysis to assess its effect on crack propagation behavior. The blunt crack was created by removing some layers of atoms and hence, high surface energy was present near the crack in the system. Results showed that failure stress of systems with sharp crack was much higher than compared to blunt crack. Propagation of blunt crack happened more in a void growth manner whereas systems with

sharp crack displayed cleavage fracture. As a result, blunt crack showed more plastic behavior during crack propagation compared to the sharp crack. As system underwent mixed mode loading stress intensity factors K_I, K_{II} (for cracks oriented at 30°-80°) and K_{Ic} (90° crack) were evaluated. We observed that, Stress intensity factors K_I, K_{II} and K_{Ic} for sharp crack was much higher than those obtained for blunt cracks. Also, individually for all three material systems as crack transited from 30° to 90° mode-I stress intensity factor (K_I) kept on increasing. On the contrary, mode-II stress intensity factor (K_{II}) was highest for crack oriented at 40° and kept on decreasing for cracks oriented from 40° to 80°.

The angles measured from crack propagation as simulated by molecular dynamics were compared with theoretical solutions from Maximum Stress failure criterion for mixed mode fracture as given by Erdogan and Sih. Having known, K_I, K_{II} and K_{Ic} from MS criterion crack growth angles (θ) were obtained by minimizing the equation representing the criterion. It was found that results were in agreement for cracks initially oriented at up to 60°, beyond which angles obtained from crack propagation in MD simulation did not match with that of the theoretical solutions by MS criterion. Also, crack propagation angles obtained for blunt crack models from MD simulations were in particularly in less agreement with theoretical solution compared to sharp crack model. This behavior is attributed to stress concentration effect due to sharp corners created by removing layers of atoms. Hence, one can conclude that given proper details MD simulation can recreate experimental results and can serve as an effective chain between theory and experiments.

Apart from crack propagation under mixed mode loading in SiC and ZrB_2, core-shell morphology for the ZrB_2/SiC composite system was designed computationally by using molecular dynamics. Appropriate interatomic potentials were undertaken to represent the interactions at the interface as close to real system as possible. Optimum Lennard-Jones parameter for interactions between Zr and C were obtained from surface

energy information available, and the ZrB_2/SiC system was loaded mechanically using MD simulation.

Chapter 6 Future Work

The considered systems for the current study was single crystal Al, SiC, and ZrB_2, from which, Al behaves closely as isotropic at the crystal level as predicted by using Zener number. But as evaluated earlier SiC is anisotropic at crystal level, and this anisotropy has to be incorporated into failure criterions being used for assessment of crack propagation behavior under mixed mode loading, which will be addressed in future work.

Apart from initial orientation of crack, lattice orientation also effects crack propagation angles, and one lattice orientation can be stronger than other. It is a necessity to perform crack propagation under mixed mode loading under such settings to gather more idea on reproducibility of MD results.

Maximum stress criterion is used in present study which uses critical value of mode-I stress-intensity factor (K_{Ic}) only as a failure criterion and no other material property shows up in the system equation. It also assumes isotropic behavior for material undertaken. But, it is researched that fracture toughness alone cannot be treated as a material constant when crack is no longer than several nanometers and in practice, stress field ahead of the crack is often mixed type and highly non-linear. Some authors have reported on this non-linearity. Future works spans on to encompass this behavior in the failure criterions being selected for crack propagation in mixed mode loading.

The material systems considered in the present study were also single crystalline. But most of the materials in practical applications are polycrystalline as shown in Figure 6-1. Different orientations of grains and different structure at grain boundaries in such materials are found to affect crack propagation vastly and crack propagation in polycrystalline structure is an open problem and lots of research is being done in the field. Contributing in such adverse research field will be of great interest.

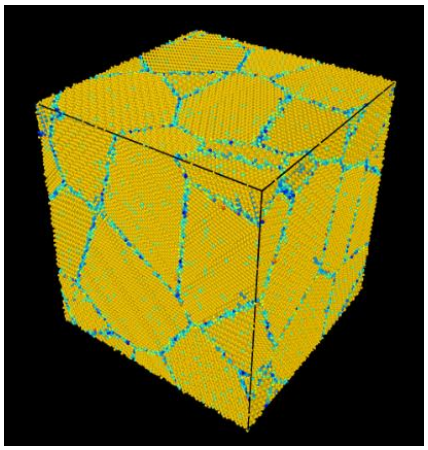

Figure 6-1: Polycrystalline Silicon carbide system

Actual core-shell structure may differ mechanically compared to system undertaken in the present study. To make the system as real as possible complex designing of a material system is needed. As displayed in Figure 6-2, atoms from SiC grains are removed to obtained only grain boundary which will act as shell structure. ZrB_2 atoms will be added into voids to complete the core-shell system in future and will be analyzed using MD simulations.

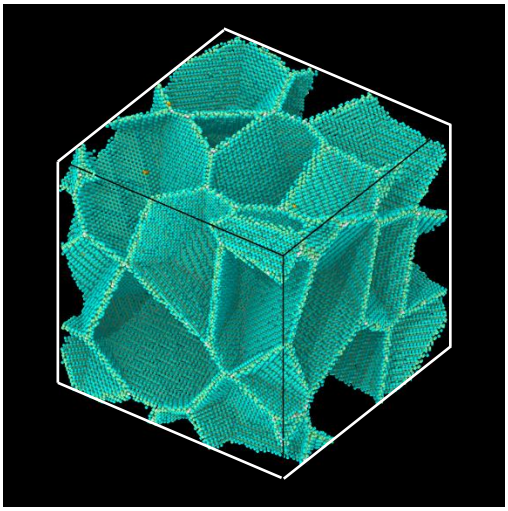

Figure 6-2: Shell structure created by removing atoms from grains of Silicon Carbide ploy-crystalline system

References

1. Gibbs, Yvonne, ed. (28 February 2014). "NASA Armstrong Fact Sheet: X-15 Hypersonic Research Program". NASA. Retrieved 4 October 2015.
2. Purwar, A., & Basu, B. (2017). Thermo-structural design of ZrB2-SiC-based thermal protection system for hypersonic space vehicles. Journal of the American Ceramic Society, 100(4), 1618–1633.
3. Wei, J., Dharani, L. R., Chandrashekhara, K., Hilmas, G. E., & Fahrenholtz, W. G. (2014). Modeling of Thermal and Mechanical Behavior of ZrB 2 -SiC Ceramics after High Temperature Oxidation, 2014(l).
4. Silvestroni, L., Kleebe, H.-J., Fahrenholtz, W. G., & Watts, J. (2017). Super-strong materials for temperatures exceeding 2000 °C. Scientific Reports, 7(November 2016), 40730.
5. Marschall, J., Pejakovic, D. A., Fahrenholtz, W. G., Hilmas, G. E., Zhu, S. M., Ridge, J., … Thomel, J. (2009). Oxidation of ZrB(2)-SiC Ultrahigh-Temperature Ceramic Composites in Dissociated Air. Journal Of Thermophysics and Heat Transfer, 23(2), 267–278.
6. Hu, P., Guolin, W., & Wang, Z. (2009). Oxidation mechanism and resistance of ZrB2-SiC composites. Corrosion Science, 51(11), 2724–2732.
7. Soboyejo, W. O., Obayemi, J. D., Annan, E., Ampaw, E. K., Daniels, L., & Rahbar, N. (2015). Review of High Temperature Ceramics for Aerospace Applications. Advanced Materials Research, 1132, 385–407.
8. Tang, S., Deng, J., Wang, S., Liu, W., & Yang, K. (2007). Ablation behaviors of ultra-high temperature ceramic composites. Materials Science and Engineering A, 465(1–2), 1–7.
9. Eakins, E., Jayaseelan, D. D., & Lee, W. E. (2011). Toward oxidation-resistant ZrB2-SiC ultra high temperature ceramics. Metallurgical and Materials Transactions A: Physical Metallurgy and Materials Science, 42(4), 878–887.
10. Zhang, L., & Padture, N. P. (2017). Inhomogeneous oxidation of ZrB2-SiC ultra-high-temperature ceramic particulate composites and its mitigation. Acta Materialia, 129, 138–148.
11. Monteverde, F., Savino, R., Fumo, M. D. S., & Di Maso, A. (2010). Plasma wind tunnel testing of ultra-high temperature ZrB2-SiC composites under hypersonic re-entry conditions. Journal of the European Ceramic Society, 30(11), 2313–2321.
12. T. H. Squire and J. Marschall, "Material property requirements for analysis and design of UHTC components in hypersonic applications," Journal of the European Ceramic Society, vol. 30, pp. 2239-2251, 2010.
13. R. Loehman, Corral, E., Dumm, H.P., Kotula, P., Tandon, R., "Ultra-high temperature ceramics for hypersonic vehicle applications," Sandia National Laboratories.
14. C. A. Steeves, He, M., Valdevit, L., Evans, A.G., , "Metallic structural heat pipes as sharp leading edges from MACH 7 vehicles," in Proceedings of IMECE 2007, ASME International Mechanical Engineering Congress and Exposition, Seattle, USA, 2007.
15. D. D. J. Van Wie DM, King DE and Hudson CM, "The hypersonic environment: Required operating conditions and design challenges," J. Mater. Sci., vol. 39, pp. 5915- 5924, 2004.
16. E. D. a. F. A. Jackson TA, "High speed propulsion: Performance advantage of advanced materials," J. Mater. Sci., vol. 39, pp. 5905-5913, 2004.

17. M. M. Opeka, I. G. Talmy, and J. A. Zaykoski, "Oxidation-based materials selection for 2000°C + hypersonic aerosurfaces: Theoretical considerations and historical experience," Journal of Materials Science, vol. 39, pp. 5887-5904, 2004.
18. Monteverde, F., Guicciardi, S., & Bellosi, A. (2003). Advances in microstructure and mechanical properties of zirconium diboride based ceramics. Materials Science and Engineering A, 346(1–2), 310–319.
19. Guo, S. Q. (2009). Densification of ZrB2-based composites and their mechanical and physical properties: A review. Journal of the European Ceramic Society, 29(6), 995–1011.
20. Li, H., Zhang, L., Zeng, Q., Wang, J., Cheng, L., Ren, H., & Guan, K. (2010). Crystal structure and elastic properties of ZrB compared with ZrB 2: A first-principles study. Computational Materials Science, 49(4), 814–819.
21. Loehman, R., Corral, E., Dumm, H., Kotula, P., & Tandon, R. (2006). Ultra high temperature ceramics for hypersonic vehicle applications. Sandia Report: Sand2006-2925, (June), 46.
22. Clougherty, E.V., Kaufman, L. “Investigation of Boride Compounds for Very High Temperature Applications,” ManLabs, Inc., Cambridge, MA, Air Force Technical Documentary Report No. RTD-TDR-63-4096, 1963.
23. Kuriakose, a. K., & Margrave, J. L. (1964). The Oxidation Kinetics of Zirconium Diboride and Zirconium Carbide at High Temperatures. Journal of The Electrochemical Society, 111(7), 827.
24. D. E. Wiley, W. R. Manning, and J. O. Hunter, "Elastic properties of polycrystalline TiB2, ZrB2 and HfB2 from room temperature to 1300 °K," Journal of The Less-Common Metals, vol. 18, pp. 149-157.
25. Fahrenholtz, W. G., Hilmas, G. E., Talmy, I. G., & Zaykoski, J. A. (2007). “Refractory diborides of zirconium and hafnium”. Journal of the American Ceramic Society, 90(5), 1347–1364.
26. Vajeeston, P., Ravindran, P., Ravi, C., & Asokamani1, R. (2001). “Electronic structure, bonding, and ground-state properties of AlB_{2}-type transition-metal diborides”. Physical Review B, 63(4), 45115.
27. Okamoto, N. L., Kusakari, M., Tanaka, K., Inui, H., Yamaguchi, M., & Otani, S. (2003). “Temperature dependence of thermal expansion and elastic constants of single crystals of ZrB2 and the suitability of ZrB2 as a substrate for GaN film”. Journal of Applied Physics, 93(1), 88–93.
28. Milman, V., Winkler, B., & Probert, M. I. J. (2005). Stiffness and thermal expansion of ZrB 2 : an ab initio study. Journal of Physics: Condensed Matter, 17(13), 2233–2241.
29. Zhang, X., Luo, X., Han, J., Li, J., & Han, W. (2008). Electronic structure, elasticity and hardness of diborides of zirconium and hafnium: First principles calculations. Computational Materials Science, 44(2), 411–421.
30. Zhou, Y., Wang, J., Li, Z., Zhan X., Jingyang, Wang (2014). First-Principles investigation on the chemical bonding nd intrinsic elastic properties of transition metal diborides TMB 2 (TM=Zr, Hf, Nb, Ta, and Y). UHTC : Materials for Extreme Environment Applications, First Edition, Wiley.
31. Fahrenholtz, W. G., Hilmas, G. E., Chamberlain, A. L., & Zimmermann, J. W. (2004). Processing and characterization of ZrB 2 -based ultra-high temperature monolithic and brous monolithic ceramics. Journal of Materials Science, 39, 5951–5957.

32. Zhang, X., Xu, L., Du, S., Liu, C., Han, J., & Han, W. (2008). Spark plasma sintering and hot pressing of ZrB2-SiCW ultra-high temperature ceramics. Journal of Alloys and Compounds, 466(1–2), 241–245.
33. Y. Y. Wang et al., "Electrical and Mechanical Properties of ZrB2-Based Composite Ceramic", Key Engineering Materials, Vols. 512-515, pp. 744-747, 2012
34. Opeka, M. M., Talmy, I. G., Wuchina, E. J., Zaykoski, J. A., & Causey, S. J. (1999). Mechanical, Thermal, and Oxidation Properties of Refractory Hafnium and zirconium Compounds. Journal of the European Ceramic Society, 19(13–14), 2405–2414.
35. Meléndez-Martínez, J. J., Domínguez-Rodríguez, A., Monteverde, F., Melandri, C., & De Portu, G. (2002). Characterisation and high temperature mechanical properties of zirconium boride-based materials. Journal of the European Ceramic Society, 22(14–15), 2543–2549.
36. Monteverde, F. (2006). Beneficial effects of an ultra-fine α-SiC incorporation on the sinterability and mechanical properties of ZrB2. Applied Physics A: Materials Science and Processing, 82(2), 329–337.
37. Monteverde, F. (2009). The addition of SiC particles into a MoSi2-doped ZrB2 matrix: Effects on densification, microstructure and thermo-physical properties. Materials Chemistry and Physics, 113(2–3), 626–633.
38. Grigoriev, O. N., Galanov, B. A., Kotenko, V. A., Ivanov, S. M., Koroteev, A. V., & Brodnikovsky, N. P. (2010). Mechanical properties of ZrB2-SiC(ZrSi2) ceramics. Journal of the European Ceramic Society, 30(11), 2173–2181.
39. Guo, S. Q., Yang, J. M., Tanaka, H., & Kagawa, Y. (2008). Effect of thermal exposure on strength of ZrB2-based composites with nano-sized SiC particles. Composites Science and Technology, 68(14), 3033–3040.
40. Guo, S. Q., Kagawa, Y., & Nishimura, T. (2009). Mechanical behavior of two-step hot-pressed ZrB2-based composites with ZrSi2. Journal of the European Ceramic Society, 29(4), 787–794.
41. Zapata-Solvas, E., Jayaseelan, D. D., Lin, H. T., Brown, P., & Lee, W. E. (2013). Mechanical properties of ZrB2- and HfB2-based ultra-high temperature ceramics fabricated by spark plasma sintering. Journal of the European Ceramic Society, 33(7), 1373–1386.
42. Zhu, S. (2008). Densification , microstructure , and mechanical properties of zirconium diboride based ultra-high temperature ceramics. Doctoral Dissertations.
43. Guo, S., Nishimura, T., & Kagawa, Y. (2011). Preparation of zirconium diboride ceramics by reactive spark plasma sintering of zirconium hydride-boron powders. Scripta Materialia, 65(11), 1018–1021.
44. Fahrenholtz, W. G., Hilmas, G. E., Zhang, S. C., & Zhu, S. (2008). Pressureless sintering of zirconium diboride: Particle size and additive effects. Journal of the American Ceramic Society, 91(5), 1398–1404.
45. Chamberlain, A. L., Fahrenholtz, W. G., & Hilmas, G. E. (2006). Pressureless sintering of zirconium diboride. Journal of the American Ceramic Society, 89(2), 450–456.
46. Talmy, I. G., Zaykoski, J. A., Opeka, M. M., & Smith, A. H. (2006). Properties of ceramics in the system ZrB2-Ta5Si3. J. Mater. Res.
47. Clougherty, E. V, Wilkes, K. E., & Tye, R. P. (1969). Research and Development of Refractory Oxidation-Resistant Diborides.

48. Chamberlain, A. L., Fahrenholtz, W. G., Hilmas, G. E., & Ellerby, D. T. (2004). High-Strength Zirconium Diboride-Based Ceramics. Journal of the American Ceramic Society, 87(6), 1170–1172.
49. Chamberlain, Adam L., Fahrenholtz, William G., Hilmas, Gregory E., Ellerby, Donald T. (2003). Characterization of Zirconium Diboride-Molybdenum Disilicide Ceramics.
50. Chamberlain, A. L., Fahrenholtz, W. G., Hilmas, G. E., & Ellerby, D. T. (2004). Characterization of Zirconium Diboride for Thermal Protection System.
51. Fahrenholtz, W. G., Wuchina E. J., Lee W. E., Zhou Y. (2014). 'Ultra-High Temperature Ceramics: Materials for extreme environment applications', the American Ceramic Society, Wiley.
52. Muranaka, T., Kikuchi, Y., Yoshizawa, T., Shirakawa, N., & Akimitsu, J. (2008). Superconductivity in carrier-doped silicon carbide. Science and Technology of Advanced Materials, 9(4), 44204.
53. Park, Yoon-Soo (1998). SiC materials and devices. Academic Press. pp. 20–60. ISBN 0-12-752160-7.
54. Hayun, S., Paris, V., Mitrani, R., Kalabukhov, S., Dariel, M. P., Zaretsky, E., & Frage, N. (2012). Microstructure and mechanical properties of silicon carbide processed by Spark Plasma Sintering (SPS). Ceramics International, 38(8), 6335–6340.
55. Nakashima, S., & Harima, H. (1997). Raman Investigation of SiC Polytypes. Physica Status Solidi A, 162, 39–64.
56. P. Greulich-Weber. (2010). Silicon Carbide: Basics.
57. Starke, U., Bernhardt, J., Schardt, J., & Heinz, K. (1999). SiC surface reconstruction: relevancy of atomic structure for growth technology. Surface Review and Letters.
58. C. H. Park, B.-H. Cheong, K.-H. Lee, and K. J. Chang, "Structural and electronic properties of cubic, 2H, 4H, and 6H SiC," Physical Review B, vol. 49, pp. 4485-4493, 1994.
59. Chang, K. J., & Cohen, M. L. (1987). Ab initio pseudopotential study of structural and high-pressure properties of SiC. Physical Review B, 35(15), 8196–8201.
60. P. E. Van Camp, V. E. Van Doren, and J. T. Devreese, "First-principles calculation of the pressure coefficient of the indirect band gap and of the charge density of C and Si," Physical Review B, vol. 34, pp. 1314-1316, 07/15/ 1986.
61. B. H. Cheong, K. J. Chang, and M. L. Cohen, "Pressure dependences of band gaps and optical-phonon frequency in cubic SiC," Physical Review B, vol. 44, pp. 1053-1056, 07/15/ 1991.
62. N. Churcher, K. Kunc, and V. Heine, "Calculated ground-state properties of silicon carbide," Journal of Physics C: Solid State Physics, vol. 19, p. 4413, 1986.
63. N. Churcher, K. Kunc, and V. Heine, "Ground state properties of the group IV ionic compound silicon carbide," Solid State Communications, vol. 56, pp. 177-180, 10// 1985.
64. P. J. H. Denteneer and W. van Haeringen, "Ground-state properties of polytypes of silicon carbide," Physical Review B, vol. 33, pp. 2831-2834, 02/15/ 1986.
65. P. J. H. Denteneer and W. van Haeringen, "Ground-state properties of wurtzite silicon carbide," Solid State Communications, vol. 65, pp. 115-119, 1// 1988.
66. Turkevich, V. Z., Stratiichuk, D. A., Tonkoshkura, M. A., & Bezhenar, N. P. (2014). Thermodynamic calculation of the Al-B system at pressures to 8 GPa. Journal of Superhard Materials, 36(6), 437–439.

67. Harris, Gary Lynn (1995). Properties of silicon carbide. IET. p. 19; 170–180. ISBN 0-85296-870-1
68. Yamamoto, T. a., Kondou, T., Kodera, Y., Ishii, T., Ohyanagi, M., & Munir, Z. a. (2005). Mechanical Properties of β-SiC Fabricated by Spark Plasma Sintering. Journal of Materials Engineering and Performance, 14(4), 460–466.
69. Wuchina, E., Opila, E., Opeka, M., Fahrenholtz, W., & Talmy, I. (2007). UHTCs: Ultra-High Temperature Ceramic Materials for Extreme Environment Applications. The Electrochemical Society Interface, 30–36.
70. Varshney, D., Varshney, S. S. M., & Khenata, N. S. R. (2015). Elastic and thermodynamical properties of cubic (3 C) silicon carbide under high pressure and high temperature. Journal of Theoretical and Applied Physics, 9(3), 221–249.
71. Miao, M., & Lambrecht, W. (2003). Unified path for high-pressure transitions of SiC polytypes to the rocksalt structure. Physical Review B, 68(9), 1–4.
72. Shimojo, F., Ebbsjö, I., Kalia, R. K., Nakano, A., Rino, J. P., & Vashishta, P. (2000). Molecular Dynamics Simulation of Structural Transformation in Silicon Carbide under Pressure. Physical Review Letters, 84(15), 3338–3341.
73. Vashishta, P., Kalia, R.K., Nakano, A.: Interaction potential for silicon carbide: A molecular dynamics study of elastic constants and vibrational density of states for crystalline and amorphous silicon.
74. Tersoff, J. (1988). New empirical approach for the structure and energy of covalent systems. Physical Review B, 37(12), 6991–7000.
75. Stillinger, F. H., & Weber, T. A. (1985). Computer simulation of local order in condensed phases of silicon. Physical Review B, 31(8), 5262–5271.
76. Aleksandrov, I. V., Goncharov, A. F., Stishov, S. M., & Yakovenko, E. V. (1989). Equation of State and Raman scattering in cubic BN and SiC at high pressure. American Institute of Physics.
77. Feldman, D. W., Parker, J. H., Choyke, W. J., & Patrick, L. (1968). Phonon Dispersion Curves by Raman Scattering in SiC, Polytypes. Physical Review, 173(3), 787–793.
78. Institute for Basic Standards (U.S.). Selected Values of Chemical Thermodynamic Properties: Tables for the First Thirty-four Elements In the Standard Order of Arrangement. Washington, D.C.: Dept. of Commerce, National Bureau of Standards, 19681975.
79. Lee, D. H., & Joannopoulos, J. D. (1982). Simple scheme for deriving atomic force constants: Application to SiC. Physical Review Letters, 48(26), 1846–1849.
80. YEAN, DH, and JR RITER. "estimates of Isothermal Bulk Moduli for Group (Iva) Crystals with Zincblende Structure." Journal of Physics and Chemistry of Solids, vol. 32, no. 3, 1971, pp. 653-653.
81. CARNAHAN, R. D. "Elastic Properties of Silicon Carbide." Journal of the American Ceramic Society, vol. 51, no. 4, 1968, pp. 223-224.
82. Matsumoto, T., Nose, T., Nagata, Y., Kawashima, K., Yamada, T., Nakano, H., & Nagai, S. (2004). Measurement of High-Temperature Elastic Properties of Ceramics Using a Laser Ultrasonic Method. Journal of the American Ceramic Society, 84(7), 1521–1525.
83. Desmaison-Brut, M., Tetard, D., Tixier, C., Faure, C., & Chabas, E. (2007). Mechanical Properties and Oxidation Behaviour of Electroconductive Ceramic Composites, 1315–1320.

84. Weber, W. J., Yu, N., Wang, L. M., & Hess, N. J. (1997). Temperature and dose dependence of ion-beam-induced amorphization in α-SiC. Journal of Nuclear Materials, 244(3), 258–265.
85. A. H. Rashed. (2002). Properties and Characteristics of Silicon Carbide. POCO Graphite, Inc, 5(7), 18–20.
86. Lonné, Q., Glandut, N., & Lefort, P. (2012). Surface densification of porous ZrB 2-39mol.% SiC ceramic composites by a laser process. Journal of the European Ceramic Society, 32(4), 955–963.
87. Jaffe HA. Development and testing of superior nozzle materials. National Aeronautics and Space Administration Final report for Project NASw-67. Washington, DC: National Aeronautics and Space Administration; April 1961
88. Arthur D, L. (1964). Thermodynamic and Kinetic Studies for a Refractory Materials Program, 33(616).
89. Fahrenholtz, William G., et al., eds. Ultra-high temperature ceramics: materials for extreme environment applications. John Wiley & Sons, 2014.
90. Berkowitz-mattuck, J. B. (1967). High-Temperature Oxidation, 908–914.
91. Air, I. V., Base, F., Lyon, T. F., & Desantis, V. J. (1964). Refractory Materials Research, 4776(4776).
92. Mizuguchi, T., Guo, S., & Kagawa, Y. (2010). Transmission electron microscopy characterization of spark plasma sintered ZrB2 ceramic. Ceramics International, 36(3), 943–946.
93. Kaufman, L., & Clougherty, E. V. (1963). Investigation of Boride Compounds for Very High Temperature Applications, Part I.
94. Kaufman, L., & Clougherty, E. V. (1965). Investigation of Boride Compounds for Very High Temperature Applications, Part II.
95. Clougherty, E. V, Wilkes, K. E., Tye, R. P., Peters, E. T., & Kalish, D. (1969). Research and Development of Refractory Oxidation-Resistant Diborides, Part II, volume II.
96. Clougherty, E. V., Pober, R. L., & Kaufman, L. (1968). Synthesis of oxidation resistant metal diboride composites. ManLabs., Inc., Cambridge, Mas
97. Clougherty, E. V, Wilkes, K. E., Tye, R. P., Peters, E. T., & Kalish, D. (1969). Research and Development of Refractory Oxidation-Resistant Diborides, Part II, volume IV.
98. Grierson, Anita E.; VanIngen-Dunn, C. (1995). Stability Characterization of Refractory Materials Under High Velocity Atmospheric Flight Conditions. Part 3, Volume 2: Experimental Results of High Velocity Hot GAS/COLD WALL TESTS.
99. Number, A. D. (2002). Stability Characterization of Refractory Materials Under High Velocity Atmospheric Flight Conditions. Part 3, Volume 3: Experimental Results of High Velocity Hot GAS/COLD WALL TESTS.Akin, I., Hotta, M., Sahin, F. C., Yucel, O., Goller, G., & Goto, T. (2009).
100. Microstructure and densification of ZrB2-SiC composites prepared by spark plasma sintering. Journal of the European Ceramic Society, 29(11), 2379–2385.
101. Sun, C. N., Gupta, M. C., & Taminger, K. M. B. (2010). Electron beam sintering of zirconium diboride. Journal of the American Ceramic Society, 93(9), 2484–2486.
102. Ran, S., Van der Biest, O., & Vleugels, J. (2010). ZrB2-SiC composites prepared by reactive pulsed electric current sintering. Journal of the European Ceramic Society, 30(12), 2633–2642.

103. Yuan, Z., Jin, Z., Kang, R., & Wen, Q. (2012). Tribochemical polishing CVD diamond film with FeNiCr alloy polishing plate prepared by MA-HPS technique. Diamond and Related Materials, 21, 50–57.
104. Dong, X., Lü, F., Yang, L., Zhang, Y., & Wang, X. (2008). Influence of spark plasma sintering temperature on electrochemical performance of La0.80Mg0.20Ni3.75 alloy. Materials Chemistry and Physics, 112(2), 596–602.
105. Effect of holding time and pressure on properties of ZrB2–SiC composite fabricated by the spark plasma sintering reactive synthesis method. (2009). International Journal of Refractory Metals and Hard Materials, 27(1), 177–180.
106. Guo, W. M., Vleugels, J., Zhang, G. J., Wang, P. L., & Van der Biest, O. (2010). Effect of heating rate on densification, microstructure and strength of spark plasma sintered ZrB2-based ceramics. Scripta Materialia, 62(10), 802–805.
107. Watts, J., Hilmas, G., & Fahrenholtz, W. G. (2011). Mechanical characterization of ZrB2-SiC composites with varying SiC particle sizes. Journal of the American Ceramic Society, 94(12), 4410–4418.
108. Clegg, W. J., Kendall, K., Alford, N. M., Button, T. W., & Birchall, J. D. (1990). A simple way to make tough ceramics. Nature, 347(6292), 455–457.
109. Kovar, D., Thouless, M. D., & Halloran, J. W. (1998). Crack deflection and propagation in layered silicon nitride/boron nitride ceramics. Journal of American Ceramics Society, 81(4), 1004–1012.
110. Tomaszewski, H., Węglarz, H., Wajler, A., Boniecki, M., & Kalinski, D. (2007). Multilayer ceramic composites with high failure resistance. Journal of the European Ceramic Society, 27(2–3), 1373–1377.
111. Bermejo, R., & Danzer, R. (2010). High failure resistance layered ceramics using crack bifurcation and interface delamination as reinforcement mechanisms. Engineering Fracture Mechanics, 77(11), 2126–2135.
112. Grigoriev, O. N., Karoteev, A. V., Maiboroda, E. N., Berezhinsky, I. L., Serdega, B. K., Ostrovoi, D. Y., & Piskunov, V. G. (2006). Structure, nonlinear stress-strain state and strength of ceramic multilayered composites. Composites Part B: Engineering, 37(6), 530–541.
113. Krstic, Z., & Krstic, V. D. (2009). Fracture toughness of concentric Si3N4-based laminated structures. Journal of the European Ceramic Society, 29(9), 1825–1829.
114. Wang, H., Fan, B., Feng, L., Chen, D., Lu, H., Xu, H., … Zhang, R. (2012). The fabrication and mechanical properties of SiC/ZrB2 laminated ceramic composite prepared by spark plasma sintering. Ceramics International, 38(6), 5015–5022.
115. Lü, Z., Jiang, D., Zhang, J., Lin, Q., & Huang, Z. (2012). ZrB2–SiC laminated ceramic composites. Journal of the European Ceramic Society, 32(7), 1435–1439.
116. Zhou, P., Hu, P., Zhang, X., & Han, W. (2011). Laminated ZrB2-SiC ceramic with improved strength and toughness. Scripta Materialia, 64(3), 276–279.
117. Zhang, X., Zhou, P., Hu, P., & Han, W. (2011). Toughening of laminated ZrB2-SiC ceramics with residual surface compression. Journal of the European Ceramic Society, 31(13), 2415–2423.
118. Wei, C., Zhang, X., Hu, P., Han, W., & Tian, G. (2011). The fabrication and mechanical properties of bionic laminated ZrB 2-SiC/BN ceramic prepared by tape casting and hot pressing. Scripta Materialia, 65(9), 791–794.

119. Yuan, H., Li, J., Shen, Q., & Zhang, L. (2013). Preparation and Microstructure of Laminated ZrB 2 -SiC Ceramics with Porous ZrB 2 Interlayers. Journal of Physics: Conference Series, 419, 12001.
120. Samvedi, V., & Tomar, V. (2013). An ab initio study of ZrB2-SiC interface strength as a function of temperature: Correlating phononic and electronic thermal contributions. Journal of the European Ceramic Society, 33(3), 615–625.
121. An, Y. M., Zhang, X. H., Han, W. B., Hu, P., Chen, G. Q., & Zhao, G. D. (2015). Interface of Graphene/ZrB2 Ceramics Structure by Molecular Dynamics Simulation. Key Engineering Materials, 655, 82–86.
122. Liu, P.-L., Chizmeshya, A. V. G., & Kouvetakis, J. (2008). Structural, electronic, and energetic properties of SiC[111]/ZrB2[0001] heterojunctions: A first-principles density functional theory study. Physical Review B, 77(3), 35326.
123. Huang, Y., Zhao, S. K., Li, C. W., Wang, C. A., & Zan, Q. F. (2003). Flexure creep behaviors of Si3N4/BN laminated ceramic composites produced by rolling. In Key Engineering Materials (Vol. 249, pp. 15-24). Trans Tech Publications.
124. Wang, C. A., Huang, Y., Zan, Q., Zou, L., & Cai, S. (2002). Control of composition and structure in laminated silicon nitride/boron nitride composites. Journal of the American Ceramic Society, 85(10), 2457–2461.
125. Yang, F., Zhang, X., Han, J., & Du, S. (2008). Mechanical properties of short carbon fiber reinforced ZrB2-SiC ceramic matrix composites. Materials Letters, 62(17–18), 2925–2927.
126. Zhang, P., Hu, P., Zhang, X., Han, J., & Meng, S. (2009). Processing and characterization of ZrB2-SiCW ultra-high temperature ceramics. Journal of Alloys and Compounds, 472(1–2), 358–362.
127. Zhang, X., Xu, L., Han, W., Weng, L., Han, J., & Du, S. (2009). Microstructure and properties of silicon carbide whisker reinforced zirconium diboride ultra-high temperature ceramics. Solid State Sciences, 11(1), 156–161.
128. Li, W., Zhang, X., Hong, C., Han, W., & Han, J. (2009). Preparation, microstructure and mechanical properties of ZrB2-ZrO2 ceramics. Journal of the European Ceramic Society, 29(4), 779–786.
129. Zhang, S. C., Hilmas, G. E., & Fahrenholtz, W. G. (2006). Pressureless densification of zirconium diboride with boron carbide additions. Journal of the American Ceramic Society, 89(5), 1544–1550.
130. Sciti, D., Guicciardi, S., Bellosi, A., & Pezzotti, G. (2006). Properties of a pressureless-sintered ZrB2-MoSi2 ceramic composite. Journal of the American Ceramic Society, 89(7), 2320–2322.
131. Zhang, X., Li, W., Hong, C., Han, W., & Han, J. (2008). Microstructure and mechanical properties of hot pressed ZrB2-SiCp-ZrO2 composites. Materials Letters, 62(16), 2404–2406.
132. W. H. Mason, "Some Hypersonic Aerodynamics," Configuration Aerodynamics Class- Presentation.
133. Kaufman, L., & Clougherty, E. V. (1965). Investigation of Boride Compounds for Very High Temperature Applications, Part II.
134. Pook, L. P. (1970). The effect of crack angle on fracture toughness. National Engineering Laboratory, East Kilbridge, Report NEL 449.
135. Hoskin, B. C., Gratt D. G., & Foden P. J., (1965). Fracture of tension panels with oblique cracks. Aeronautical Research Laboratory, Melbourne, Report SM 305.

136. Erdogan, F., G. C. Sih (1963), On the Crack Extension in Plates under Plane Loading and Transverse Shear
137. Sih, G. C. (1974). Strain-energy-density factor applied to mixed mode crack problems. International Journal of Fracture, 10(3), 305–321.
138. Hussain M. A., Pu S. L., & Underwood J., (1974). Strain energy release rate for a crack under combined Mode I and II. Fracture Analysis, ASTM STP 560, American Society for Testing and Materials, pp. 2-28.
139. Cotterell B., Rice J. R. (1980) Slightly curved or kinked cracks. International journal of fracture, Vol. 16, pp. 155-169.
140. Lo K. K., (1978). Analysis of branched racks. Journal of Applied Mechanics, Vol. 45, pp. 797-802.
141. Wells, A. (1961, September). Unstable crack propagation in metals: cleavage and fast fracture. In Proceedings of the crack propagation symposium (Vol. 1, No. 84).
142. Rice, J. R. (1968). A Path Independent Integral and the Approximate Analysis of Strain Concentration by Notches and Cracks. Journal of Applied Mechanics, 35(2), 379.
143. Hutchinson, J. W. (1968). Singular behaviour at the end of a tensile crack in a hardening material. Journal of the Mechanics and Physics of Solids, 16(1), 13-31.
144. Rice, J. R., & Rosengren, G. F. (1968). Plane strain deformation near a crack tip in a power-law hardening material. Journal of the Mechanics and Physics of Solids, 16(1), 1–12.
145. Anderson, T. L. (2005). Fracture mechanics: Fundamentals and applications (3rd ed.). Boca Raton, FL: Taylor & Francis.
146. Riaz M. (2017) Grain boundary driven mechanical properties of ZrB2 and ZrC-ZrB2 nanocomposite: a molecular simulation study
147. Liu, W. K., Karpov, E. G. and Park, H. S. (2006) Introduction, in Nano Mechanics and Materials: Theory, Multiscale Methods and Applications, John Wiley & Sons, Ltd, Chichester, UK.
148. Park, H. S., & Zimmerman, J. A. (2005). Modeling inelasticity and failure in gold nanowires. Physical Review B - Condensed Matter and Materials Physics, 72(5), 1–9.
149. Raty, J.-Y., Gygi, F., & Galli, G. (2005). Growth of Carbon Nanotubes on Metal Nanoparticles: A Microscopic Mechanism from Ab Initio Molecular Dynamics Simulations. Physical Review Letters, 95(9), 96103.
150. Sakib, A. R. N., De, N. N., & Adnan, A. (2013). Shear fracture of confined NaCl nanofilms. Computational Materials Science, 68, 271–279.
151. Ferdous, S. F., & Adnan, A. (2015). Tailoring Fracture Toughness of Silicon Carbide Ceramics Film via Nanoscale Multi-layering with, (September 2014).
152. Ferdous, S. F., & Adnan, A. (2015). Computational Design of Carbon Enriched Ceramics for Improved Strength and Toughness, (October).
153. Ferdous, S. F., & Adnan, A. (2017). Mode-I Fracture Toughness Prediction of Diamond at the Nanoscale, 7(1), 1–10.
154. Haile, J. M., Johnston, I., Mallinckrodt, A. J., & McKay, S. (1993). Molecular dynamics simulation: elementary methods. Computers in Physics, 7(6), 625-625.
155. Cai, W., Li, J., & Yip, S. (2010). Molecular Dynamics. Comprehensive Nuclear Materials, 1–36.

156. Daw, M. S., & Baskes, M. I. (1984). Embedded-Atom Method: Derivation and application to impurities, surfaces and other defects in metals. Physical Review B.
157. Mishin, Y., Farkas, D., Mehl, M. J., & Papaconstantopoulos, D. A. (1999). Interatomic potentials for monoatomic metals from experimental data and ab initio calculations. Physical Review B, 59(5), 3393–3407.
158. Tersoff, J. (1988). New empirical approach for the structure and energy of covalent systems. Physical Review B, 37(12), 6991–7000.
159. Tersoff, J. (1994). Chemical order in amorphous silicon carbide. Physical Review B, 49(23), 16349–16352.
160. Daw, M. S., Lawson, J. W., & Bauschlicher, C. W. (2011). Interatomic potentials for Zirconium Diboride and Hafnium Diboride. Computational Materials Science, 50(10), 2828–2835.
161. Chen, H.-L., Ju, S.-P., Wu, T.-Y., Hsieh, J.-Y., & Liu, S.-H. (2015). Investigation of Zr and Si diffusion behaviors during reactive diffusion – a molecular dynamics study. RSC Adv., 5(33), 26316–26320.
162. KInacI, A., Haskins, J. B., Sevik, C., & Çağln, T. (2012). Thermal conductivity of BN-C nanostructures. Physical Review B - Condensed Matter and Materials Physics, 86(11), 1–8.
163. Kumagai, T., Izumi, S., Hara, S., & Sakai, S. (2007). Development of bond-order potentials that can reproduce the elastic constants and melting point of silicon for classical molecular dynamics simulation. Computational Materials Science, 39(2), 457–464.
164. Sakai, T. K. and S. H. and S. I. and S. (2006). Development of a bond-order type interatomic potential for Si–B systems. Modelling and Simulation in Materials Science and Engineering, 14(5), S29.
165. Lennard-Jones, J. (1924). On the Determination of Molecular Fields. Procedures Royal Society London A, 4(71).
166. Li, J., Liao, D., Yip, S., Najafabadi, R., & Ecker, L. (2003). Force-based many-body interatomic potential for ZrC. Journal of Applied Physics, 93(11), 9072–9085.
167. Arya, A., & Carter, E. A. (2004). Structure, bonding, and adhesion at the ZrC(1 0 0)/Fe(1 1 0) interface from first principles. Surface Science, 560(1–3), 103–120.
168. An, Y. M., Zhang, X. H., Han, W. B., Hu, P., Chen, G. Q., & Zhao, G. D. (2015). Interface of Graphene/ZrB_2 Ceramics Structure by Molecular Dynamics Simulation. Key Engineering Materials, 655, 82–86.
169. Liu, P.-L., Chizmeshya, A. V. G., & Kouvetakis, J. (2008). Structural, electronic, and energetic properties of SiC[111]/ZrB_2[0001] heterojunctions: A first-principles density functional theory study. Physical Review B, 77(3), 35326.
170. Allen, M. (2004). Introduction to molecular dynamics simulation. Computational Soft Matter: From Synthetic Polymers to …, 23(2), 1–28.
171. Kelchner, C. L., Plimpton, S. J., & Hamilton, J. C. (1998). Dislocation nucleation and defect structure during surface indentation. Physical Review B, 58(17), 11085–11088.
172. Stukowski, A., Bulatov, V. V., & Arsenlis, A. (2012). Automated identification and indexing of dislocations in crystal interfaces. Modelling and Simulation in Materials Science and Engineering, 20(8).

173. Cheng, S.-H., & Sun, C. T. (2014). Size-Dependent Fracture Toughness of Nanoscale Structures: Crack-Tip Stress Approach in Molecular Dynamics. Journal of Nanomechanics and Micromechanics, 4(4), A4014001.
174. S. Plimpton, Fast Parallel Algorithms for Short-Range Molecular Dynamics, J Comp Phys, 117, 1-19 (1995). http://lammps.sandia.gov/index.html
175. A. Stukowski, Modelling Simul. Mater. Sci. Eng. 18, 015012 (2010).
176. Schneider, C. A., Rasband, W. S., & Eliceiri, K. W. (2012). NIH Image to ImageJ: 25 years of image analysis. Nature Methods, 9(7), 671–675.

Biographical Information

Krutarth S Patel, born on 11th December 1992, completed his Bachelor of Engineering in Mechanical Engineering from LDRP Institute of Technology and Research, affiliated to Gujarat Technological University, Gujarat, India on May 2014.

He pursued his Masters in Aerospace Engineering at the University of Texas at Arlington starting August 2015. His master's thesis research work was under supervision of Dr. Ashfaq Adnan at Multiscale Mechanics and Physics Lab. His research interest includes mixed-mode fracture in materials, computational material modeling, ceramic and polymer matrix composite structures, multi-physics finite elemental modeling and ion-transport driven morphology and property transition in heterogeneous ceramic composites. During his master's study he also worked as Research Intern at the Institute for Predictive Performance Methodologies at the University of Texas at Arlington Research Institute on computational modeling of nuclear waste containment in ceramic waste forms.

He graduated with his master's degree from UTA in December 2017. He plans to continue his research on fracture prediction in composite materials as well as ion-transport driven morphology and property transition in heterogeneous ceramic conductors.